Bose-Einstein Condensation of Rubidium: Towards Ultracold Binary Bosonic Mixtures

Dissertation

zur

Erlangung des Doktorgrades (Dr. rer. nat.)

der

Mathematisch-Naturwissenschaftlichen Fakultät

der

Rheinischen Friedrich-Wilhelms-Universität Bonn

vorgelegt von

Daniel Frese

aus

Köln

Bonn 2005

Angefertigt mit Genehmigung der Mathematisch-Naturwissenschaftlichen Fakultät

der Rheinischen Friedrich-Wilhelms-Universität Bonn

1. Referent: Prof. Dr. Dieter Meschede
2. Referent: Priv.-Doz. Dr. Wolfgang Hillert

Tag der Promotion: 23.5.2005

Diese Dissertation ist auf dem Hochschulschriftenserver der ULB Bonn `http://hss.ulb.uni-bonn.de/diss_online` elektronisch publiziert.

Summary / Zusammenfassung

In this thesis, first experiments are reported towards the realization of ultracold Cesium-Rubidium mixtures. In particular, Bose-Einstein condensates (*BECs*) of Rubidium atoms have been created and combined samples of Rubidium and Cesium have been stored in magneto-optical and magnetic traps.

The presented theoretical framework (chapter 2) covers basic properties of single and double species BECs. Special attention is devoted to few particle systems of one species interacting with a larger quantum degenerated sample of a different species.

The main part of the manuscript (chapters 3, 4) describes our procedure for the creation of the Rubidium BEC and properties of the condensate. The transition to quantum degeneracy is reached with 10^5 atoms at a temperature of 300 nK. Characteristic properties of the condensate as an inversion of the aspect ratio upon free expansion and a bimodal density distribution can be clearly observed.

The third part (chapter 5) reports on first experiments with simultaneously trapped cold Cesium and Rubidium atoms. Evidence for the interaction of the two species can be identified in the MOT as well as in a magnetic trap.

Diese Arbeit berichtet über erste Experimente mit dem Ziel der Erzeugung von ultrakalten Cäsium-Rubidium Gemischen. Im Rahmen dieser Arbeit wurde zunächst ein Bose-Einstein Kondensat (*BEC*) aus Rubidiumatomen hergestellt. Zudem sind kalte Rubidium- und Cäsiumatome gleichzeitig sowohl in magnooptischen Fallen als auch in magnetischen Potenzialen gefangen worden.

Die dargelegten theoretischen Grundlagen (Kapitel 2) beschreiben wesentliche Eigenschaften von einfachen BECs sowie von Kondensaten zweier atomarer Spezies. Besonderes Augenmerk gilt hier der Wechselwirkung von Wenig-Teilchen Systemen mit einem quantenentarteten Viel-Teilchen System.

Der Hauptteil der Arbeit (Kapitel 3, 4) beschreibt die Erzeugung des BEC und charakteristische Eigenschaften des Kondensats. Der Übergang zur Quantenentartung erfolgt mit 10^5 Atomen bei 300 nK. Typische Eigenschaften des Kondensats wie die Invertierung des Achsenverhältnisses während freier Expansion und eine bimodale Dichteverteilung können deutlich beobachtet werden.

Der dritte Teil der Arbeit (Kapitel 5) befasst sich mit ersten Experimenten mit gleichzeitig gespeicherten kalten Rubidium- und Cäsiumatomen. Sowohl in der magnetooptischen Falle als auch in einer Magnetfalle können Anzeichen für eine Wechselwirkung zwischen den beiden atomaren Spezies beobachtet werden.

Contents

1 Introduction **1**

2 Theoretical foundations and predictions **5**

2.1 Basic BEC theory . . . 5
  2.1.1 Semiclassical treatment of an ideal Bose gas . . . 5
  2.1.2 Quantum mechanical theory of an interacting, condensed Bose gas . 8
2.2 Properties of two species condensates . . . 11
  2.2.1 Gross-Pitaevski and Thomas-Fermi limit . . . 12
  2.2.2 Few particles interacting with a macroscopic quantum wave . . . 16
2.3 Conclusions . . . 22

3 The route towards BEC **25**

3.1 Experimental setup . . . 25
  3.1.1 Vacuum system . . . 25
  3.1.2 Laser system . . . 27
3.2 Characterization of cold atomic clouds . . . 28
  3.2.1 Near resonant interaction with light . . . 28
  3.2.2 Imaging system for absorption measurements . . . 29
  3.2.3 Temperature measurements . . . 32
  3.2.4 Atom number measurements . . . 34
  3.2.5 Limits for the detection of small particle numbers . . . 38
3.3 Magneto-optical traps as the precooling stage . . . 40
  3.3.1 Working principles and limits . . . 41
  3.3.2 The reservoir MOT as a cold atom source . . . 47
  3.3.3 Atomic transfer beam and high vacuum MOT . . . 49
3.4 Magnetic traps . . . 54
  3.4.1 Magnetic trapping . . . 54
  3.4.2 Measurements in the magnetic quadrupole trap . . . 56
  3.4.3 Measurements in the QUIC trap . . . 62
3.5 Evaporative Cooling as the final cooling stage . . . 68
  3.5.1 Theoretical considerations . . . 68
  3.5.2 Experimental results . . . 69

3.6 Conclusions 74

4 Characterization of the BEC 77

4.1 Experimental parameters and methods 77
4.1.1 BEC figures of interest 77
4.1.2 Experimental methods 79
4.2 Measured BEC properties 81
4.2.1 Reversal of the aspect ratio and mean field energy 82
4.2.2 Atom number and critical temperature 84
4.2.3 Multi component BECs 85
4.3 Conclusions 87

5 Combined trapping of two atomic species 89

5.1 Double species atomic traps 89
5.1.1 Important properties of ^{133}Cs 89
5.1.2 Rubidium-Cesium interaction and related work 90
5.1.3 Technical implementation of a double species atomic trap 92
5.2 Results for combined trapping in Magneto-Optical Traps 94
5.2.1 The Cesium MOT 94
5.2.2 The Cesium-Rubidium MOT 95
5.3 Results for combined trapping in Magnetic Traps 97
5.4 Conclusions 98

6 Conclusion and outlook 101

6.1 Sympathetic cooling of Cesium 101
6.2 Single Cesium atoms 102

A Technical Details 105

A.1 Optical setup of the UHV MOT 105
A.2 Complete timing sequence of the experiment 105

B Relevant molecular data for the RbCs molecule 111

C Numerical methods 113

C.1 Gross-Pitaevski equation 113
C.2 Schrödinger equation 113

List of Figures 114

List of Tables **116**

Bibliography **117**

Chapter 1

Introduction

Bose-Einstein Condensation (*BEC*) was predicted by S. Bose and A. Einstein [1, 2, 3] 80 years ago in 1925. At that time, the theory and its consequences were so distinctively different from previous theoretical predictions, that it was questioned for a long time — even by one of the original authors ! In a letter to Paul Ehrenfest, Einstein remarked “Die Theorie ist hübsch, aber ob auch etwas Wahres dran ist ?” — “The theory looks neat, but is there anything real to it ?” [4]

Efforts to realize BEC in a weakly interacting gas were initiated by a paper by Stwalley and Nosanow in 1976 [5]. In this paper the authors pointed out that Hydrogen remains in its gaseous state down to temperatures necessary for BEC, while all other substances — with the exception of Helium — transform into the solid state. The groups of Silvera and Walraven in the Netherlands and Greytak and Kleppner in the USA started experiments to reach BEC in Hydrogen in the early 80s [6, 7]. The American group eventually observed BEC in 1998 [8] — 3 years after the first condensates in Alkali vapors had been realized. It turned out that ultracold alkali atoms can be stored in a metastable state with a sufficient life time to reach BEC.

Soon after the invention of laser cooling, it was realized that this technique offered a second possible route to BEC apart from the Hydrogen approach. The pioneers of laser cooling were awarded the Nobel Prize in 1997 [9, 10, 11], two years after BEC (in Sodium, Rubidium and Lithium) was achieved nearly simultaneously by three groups in 1995 [12, 13, 14]. In 2001 Carl E. Wiemann, Eric Cornell and Wolfgang Ketterle received the Nobel Prize for their contributions to studies on BEC [15, 16].

Meanwhile, the topic is one of the cornerstones of current atomic physics. After many initial experiments were focussed on the fascinating new features, which these systems exhibit in unparalleled purity — such as matter interference [17], atom lasers [18], observation of solitons in a dilute gas [19] and more — most recent experiments are mainly concentrating on one of the two following areas.

In the first class of experiments, the BEC is transferred into a light induced periodic potential, a so-called optical lattice. In such an environment, it is now possible to conduct solid state physics experiments. An especially outstanding experiment of that type is the observation of the phase transition between the superfluid and the Mott insulator state [20]. It also exemplifies another related strength of these atomic systems, namely to tailor external potentials in a flexible way unrivaled by solid state physics. Other exciting experiments of this class include e.g. the observation of the Josephson effect [21] and superfluidity [22]. BEC has served as a bridge between two different communities, who have now a common field of interest: most applied techniques stem from atomic physics while many concepts are taken from condensed matter physics.

A second focus of current research in ultracold gases is on questions related to atomic and molecular physics. Traditional atomic and quantum optical experiments, such as atomic interferometers [23] and atomic optics, [24] are reexamined using BECs as well as ultracold fermionic ensembles. The interaction of these ultracold atoms is of particular interest. It is now possible to build homonuclear ultracold dimers [25, 26] or tune the inter-atomic interaction using Feshbach resonances. Feshbach resonances are dramatic enhancements of the scattering cross section between two atoms for certain values of an external magnetic field [27]. Utilizing these resonances, it has even become possible to control the effective interaction between atoms of different species [28, 29].

The experiment, which will be described in this manuscript, is designed to contribute to the latter area. Our aim is to examine the interactions in a two component mixture made of Rubidium and Cesium atoms. By preparing two different species for an ultracold sample, a selective control of the ingredients becomes possible. Also qualitatively new features of a heteronuclear dimer as e.g. a static polarizability [30] become accessible.

Another intriguing possibility stemming from the inequality of the two species is to study a small system coupled to a larger one. In the most extreme case it should be possible to study the behavior of one impurity atom inside a larger system made up of atoms of the second species. Recently, the interaction of two such immersed impurities by phonons within the larger cloud was studied theoretically in [31].

For this extreme case, one expects only a slight change of the properties of the larger cloud. The behavior of a single impurity atom, on the other hand, will be significantly changed due to the interaction with the large cloud. A particular interesting application resulting from this situation is to use a large number of one species as a cooling agent for a few particles system of the other species. It has been proposed, that cooling few particles by immersing them into a BEC will at the same time cool the dopant atoms and also preserve coherence properties of the sample [32]. Since cooling is usually associated with dissipation and loss of coherence, this fact is already interesting in itself. Furthermore, such a mechanism has direct applications for the handling of few atom systems. One of the main experimental constraints so far is the observed heating due to imperfections in the applied storage schemes.

Increasing the number of impurities, one will reach a region in which the influence of the smaller sub-system on the larger one is not negligible any more. For equally large clouds, both ensembles are expected to interact with each other in a collective way and one can expect that the single particle character of the impurities will vanish completely. These heteronuclear systems offer the unique chance to observe the transition from single to multi-particle physics in a controlled way.

This thesis reports on initial experiments directed to realize this program. First I discuss important properties of single and two species condensates. It turns out, that the interaction between atoms of the same species and also of different species can be subsumed with one number. This is the s-wave scattering length for homonuclear collisions and heteronuclear collisions respectively. It is one objective of this thesis to pave the way towards an experimental determination of the s-wave scattering length for Rubidium–Cesium collisions.

In order to build model-like systems, as required to study the above mentioned effects, it is necessary to combine several experimental technologies, each at a challenging level. These techniques are closely related to the methods used to create our BEC. In this thesis, I illustrate the main steps to reach our BEC in detail. Following this description is a systematic study of some important properties of our BEC. This also illustrates the possibilities and limitations for performing the aimed experiments on two species systems.

Further I give a first account of our experiments with two different atomic species. First results are shown on storing and manipulating Rubidium and Cesium simultaneously. The interaction of Cesium and Rubidium results in very different signatures, depending on whether the mixture is exposed to near resonant light — as in a magneto-optical trap — or whether they are stored in a dark magnetic trap in their electronic ground state.

Chapter 2

Theoretical foundations and predictions

In this chapter, the main features of a Bose condensed gas are given. One focus within the discussion are the approximations and simplifications of the theoretical models, since some of these assumptions — and correspondingly some results derived therefrom — are not correct in the context of few particle systems.

Properties of a quantum degenerate gas consisting of two different atomic species are examined in the second part. Depending on the particle number ratio of one species compared with the other one, different regimes can be distinguished. The two cases of two equally large samples and of one sample consisting of much more atoms than the second one, are studied.

2.1 Basic BEC theory

Many properties of Bose Einstein condensation can be derived within a semiclassical framework. Most of these predictions agree surprisingly well with experimental findings, although substantial simplifications are applied. The results are explicitly used in chapter 4 to analyze corresponding measurements.

To describe the detailed properties of the condensed phase however, one has to resort to more exact quantum mechanical models. This is pursued in the second section.

2.1.1 Semiclassical treatment of an ideal Bose gas

Numerous review papers [33, 34] as well as a dedicated textbook [27] are by now available on BEC detailing nearly every aspect of this topic. Here I introduce the necessary theoretical basis and the nomenclature relevant to the described experiments.

The distribution function for a system of non-interacting Bosons in thermal equilibrium is given by

$$f_{\mathrm{B}}(E_n) = \frac{1}{\exp\left((E_n - \mu)/kT\right) - 1}, \tag{2.1}$$

where E_n is the energy of the nth energy eigenstate, μ is the chemical potential, k is the Boltzmann Constant and T the temperature. This equation also shows that the chemical potential must always be less than the ground state energy, since otherwise a negative population of the ground state would result. In a semiclassical treatment one replaces the discrete energy spectrum of the system by a continuous one, assuming that the difference between two neighboring energy eigenvalues is much smaller than other energies of interest. In this case one can define for a given external potential the density of states $\rho(E)$ by the definition

$$\int_{E_0}^{E_1} dE\, \rho(E) = \text{number of states with energies between } E_0 \text{ and } E_1. \tag{2.2}$$

The key point for exploring BEC within this formalism is to treat the lowest energy state separately. Since the population of states is a smooth function of the energy E for temperatures higher than a certain critical temperature T_c (which usually is very small), the extra treatment of the ground state is not important for these temperatures. But for $T < T_c$, the population of the ground state becomes macroscopic, adding a δ-functional like term for the population at the ground state energy.

As long as the occupation of the lowest energy state is negligible, all N particles of the system will be in excited states, and this determines the chemical potential via

$$\int_{E_0}^{\infty} dE\, \rho(E)\, f_{\mathrm{B}}(E) = N_{\text{excited}} = N. \tag{2.3}$$

According to this equation and (2.1), by lowering the temperature the chemical potential is driven to E_0. The temperature, at which $\mu = E_0$, is the critical temperature T_c. For temperatures lower than T_c the integral in (2.3) is always less than N. For particle number conserving problems this implies that for $T < T_c$ the ground state must be populated macroscopically with $N - N_{\text{excited}}$ particles. The critical temperature is thus determined by the condition

$$\int_{0}^{\infty} dE\, \rho(E) \frac{1}{\exp\left(E/kT_c\right) - 1} = N. \tag{2.4}$$

In evaluating this expression for given density of states functions $\rho(E)$ one frequently encounters functions of the class $g_k(x) = \sum_{n=1}^{\infty} x^n/n^k$. In particular, for the density function of a harmonic trap with potential $V(\vec{x}) = \frac{1}{2}m(\omega_1^2 x^2 + \omega_2^2 y^2 + \omega_3^2 z^2)$ one obtains [27]

$$kT_c = \hbar\overline{\omega} \left(\frac{N}{g_3(1)}\right)^{1/3} \approx 0.94 \hbar\overline{\omega} N^{1/3} \tag{2.5}$$

and for a uniform gas of density $n = N/V$ [27]

$$kT_c = \frac{2\pi\hbar^2}{m} \left(\frac{n}{g_{3/2}(1)}\right)^{2/3} \approx 3.31 \frac{\hbar^2 (N/V)^{2/3}}{m}. \tag{2.6}$$

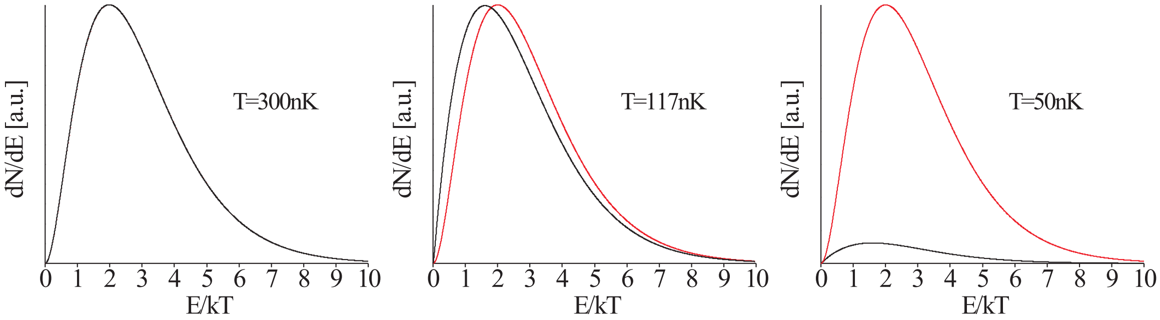

Figure 2.1: Energy distributions of 10^4 bosonic particles in a harmonic potential with parameters equal to the harmonic trap used in our experiments (black curve). The critical temperature is at 117 nK. Above this temperature the curve is in very good agreement with a Boltzmann energy distribution (red curve); close to the critical temperature T_c the distributions differ strongly and below T_c the ground state is populated macroscopically, leading to a depletion of the excited states.

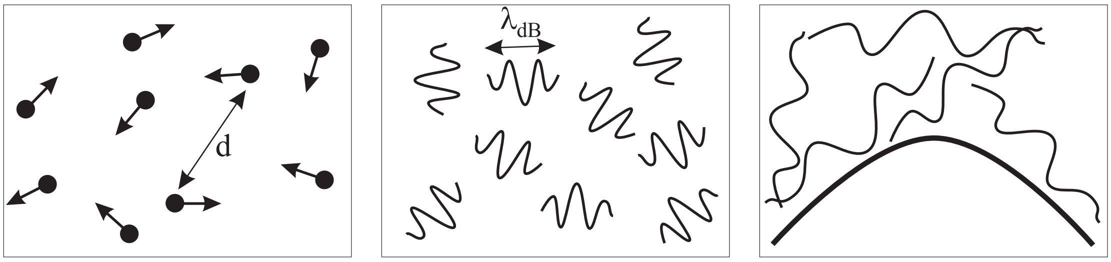

Figure 2.2: A pictorial interpretation of the BEC phase transition. At high temperatures (left) Bosons can be described as pointlike particles. The colder the gas becomes, the more prominent is the atoms' wave-like behavior (middle). Below T_c, the de Broglie waves overlap, i. e. the size of the atomic wave packets becomes comparable to their distance d, and the phase transition occurs (right). Figure adapted from [34].

Here $\overline{\omega}$ is the geometric mean of the trap frequencies $\overline{\omega} = (\omega_1\omega_2\omega_3)^{1/3}$. In figure (2.1) the energy distribution dN/dE is plotted for parameters as used in our experiments. The atoms are confined in a magnetic trap, which is described in detail in 3.4. For all considerations in this chapter it suffices to treat the trapping potential as an anisotropic harmonic potential with $\omega_1 = \omega_2 = \omega_\rho = 2\pi \cdot 271.6\ \mathrm{s}^{-1}$ and $\omega_3 = \omega_z = 2\pi \cdot 23.2\ \mathrm{s}^{-1}$. In figure (2.1) one can clearly observe the departure from the classical behavior as predicted by the Boltzmann distribution. Equation (2.6) can be cast in the well known form

$$n\lambda_{\mathrm{dB}}^3 = g_{3/2}(1) \approx 2.61, \tag{2.7}$$

$n = N/V$ being the particle density and λ_{dB} the de Broglie wavelength. The left hand side in this equation is just the phase space density of a uniform Bose gas. For a gas trapped in a harmonic trap, the condition for condensation can be formulated analogously in terms of the phase space density with equation (2.7) if one replaces n with the peak density $n(0)$ in the trap [35].

The connection with the phase space density and de Broglie wavelengths leads naturally to a pictorial interpretation of the phase transition as shown in figure (2.2). At high temperatures the atoms behave as classical, pointlike particles. With decreasing temperature the de Broglie wavelength λ_{dB} increases. In accordance with (2.7), the phase transition occurs as soon as λ_{dB} becomes comparable to the interatomic distance.

From equation (2.4) one can further calculate for $T < T_c$ the number of atoms in the condensed phase. For a gas trapped in a harmonic potential one obtains

$$\frac{N_0}{N} = 1 - \left(\frac{T}{T_c}\right)^3 . \tag{2.8}$$

Here N_0 is the number of atoms in the condensed phase.

These results from the semiclassical approach are in remarkable consistency with experimental findings. The main deviation in T_c from the given expressions is mainly due to two effects. First, if one uses exact sums instead of integrals, one encounters a deviation due to the finite number of atoms that scales in the limit of large particle numbers N as $N^{-1/3}$ [36, 37]. This is detailed later in the discussion of few particles double condensates (cf. section 2.2.2).

Second the behavior of the gas is modified due to interparticle interactions, i. e. the system is not an ideal gas. Interactions of ultracold neutral atoms arise due to collisions between them. The shift of the transition temperature T_c is again in the range of a few percent and can thus be regarded as small [38, 39].

Experimental verification of these effects is difficult because the shift of T_c is on the same order as the experimental precision. In [40] a detailed investigation has been undertaken and was later repeated with greater precision in [41], confirming the theoretical predictions.

The properties of the condensed phase itself depend very strongly on the interactions and can only be treated properly in a full quantum mechanical approach.

2.1.2 Quantum mechanical theory of an interacting, condensed Bose gas

The description of an ultracold gas of interacting bosonic atoms can be accomplished by using the formalism of many body theory in second quantization. The Hamiltonian of an interacting many particle system is given by

$$\hat{H} = \int d^3r\, \hat{\Psi}^\dagger(\vec{r}) \left(-\frac{\hbar^2}{2m}\nabla^2 + V_{\mathrm{ext}}(\vec{r})\right) \hat{\Psi}(\vec{r}) + \frac{1}{2}\int d^3r\, d^3r'\, \hat{\Psi}^\dagger(\vec{r})\hat{\Psi}^\dagger(\vec{r}')V_{\mathrm{coll}}(\vec{r}-\vec{r}')\hat{\Psi}(\vec{r}')\hat{\Psi}(\vec{r}). \tag{2.9}$$

$\hat{\Psi}(\vec{r})$ and $\hat{\Psi}^\dagger(\vec{r})$ are the annihilation and creation field operators of the boson field, acting on states in the space spanned by the Fock states $|N_0, N_1, \cdots >$. Details on the formalism can be found in [42].

For our purposes it is important to note, that $\hat{\Psi}(\vec{r})$ and $\hat{\Psi}^\dagger(\vec{r})$ satisfy the standard bosonic commutation rules and can be expanded as

$$\hat{\Psi}(\vec{r}) = \sum_{n=0}^{\infty} u_n(\vec{r})\hat{a}_n \tag{2.10}$$

$$\hat{\Psi}^\dagger(\vec{r}) = \sum_{n=0}^{\infty} u_n^*(\vec{r})\hat{a}_n^\dagger. \tag{2.11}$$

Here $u_n(\vec{r})$ are the orthogonal and normalized solutions of the single particle Schrödinger equation and $\hat{a}_n$ $(\hat{a}_n^\dagger)$ are the annihilation (creation) operators for a particle in a state with index n. This explicit expansion in turn with elementary properties of the operators $\hat{a}_n$ and $\hat{a}_n^\dagger$ shows directly, that the density operator is given by $\hat{n}(\vec{r}) = \hat{\Psi}^\dagger(\vec{r})\hat{\Psi}(\vec{r})$.

In equation (2.9) the term $V_{\text{ext}}(\vec{r})$ represents in experimentally realized systems the external harmonic trapping potential, while the term $V_{\text{coll}}(\vec{r} - \vec{r}')$ takes into account the collisional interactions. This term can be simplified greatly using two approximations, which are both very well fulfilled in BEC experiments.

First one can use the fact that all atoms are very cold. This allows to parameterize the quantum mechanical scattering process with essentially one real number, the scattering length a. The physical reason behind this becomes clear in a partial wave analysis of the scattering process. All partial waves with angular momentum larger than $l = 0$ exhibit a centrifugal barrier of the form $\hbar^2 l(l+1)/2mr^2$, which is larger than the kinetic energy of ultracold atoms. Thus particles with a non-zero angular momentum do not acquire a phase shift as compared to particles without the influence of the scattering potential, while the phase shift for the s-wave for low energies equals ka, k being the wave number of the atomic wavepacket [43].

The second approximation consists in assuming a contact potential whose spatial dependance is proportional to a δ-functional as $\delta(\vec{r} - \vec{r}')$. This is justified since the range of the interatomic van der Waals potentials, which are responsible for the interaction, is always much smaller than the distance between atoms in the gas.

These two approximations lead to an explicit form of $V_{\text{coll}}(\vec{r} - \vec{r}')$ given by

$$V_{\text{coll}}(\vec{r} - \vec{r}') = \frac{4\pi\hbar^2 a}{m}\delta(\vec{r} - \vec{r}'). \tag{2.12}$$

The appearing δ-functional simplifies (2.9) already by reducing the double integration in the V_{coll} term to a single integration. A differential equation for the field operator $\hat{\Psi}(\vec{r})$ is obtained using the Heisenberg equation of motion $i\hbar\frac{d}{dt}\hat{\Psi}(\vec{r},t) = [\hat{\Psi}(\vec{r},t), \hat{H}]$. In evaluating the commutator, in each term further δ-functionals arise due to the Boson commutator rules obeyed by the field operators and all integrals disappear. One arrives at the time dependant operator equation

$$i\hbar\frac{d}{dt}\hat{\Psi}(\vec{r},t) = \left(-\frac{\hbar^2\nabla^2}{2m} + V_{\text{ext}}(\vec{r}) + \frac{4\pi\hbar^2 a}{m}\hat{\Psi}^\dagger(\vec{r},t)\hat{\Psi}(\vec{r},t)\right)\hat{\Psi}(\vec{r},t). \tag{2.13}$$

In order to deduce a c-number differential equation from this operator equation, we need two further approximations.

For the following discussion, we are only interested in the condensed phase. Therefore all atoms are assumed to be in the ground state. From a thermodynamical point of view this corresponds to a temperature of $T = 0$ and is formally described with the Fock state $|N_0, 0 \cdots >$. Thus only the first term of the expansion in (2.11) is necessary.

This still keeps the operator property of (2.13), which can be removed in the spirit of a Bogoliubov transformation [44]. For large particle numbers N the states $|N_0 + 1, 0, \cdots >$ and $|N_0, 0, \cdots >$ correspond approximately to the same physical situation. Thus $\hat{a}$ and $\hat{a}^\dagger$ can both be approximated by $\sqrt{N_0}\hat{\mathbf{1}}$, where $\hat{\mathbf{1}}$ is the identity operator. This is equivalent to replacing the field operators by their expectation value.

These simplifications lead to a differential equation for the so-called condensate wave function[1] $\psi(\vec{r}, t)$. Choosing the ansatz $\psi(\vec{r}, t) = \psi(\vec{r})e^{-i\mu t/\hbar}$ yields the time independent Gross-Pitaevski equation

$$\mu\psi(\vec{r}) = \left(-\frac{\hbar^2\nabla^2}{2m} + V_{\text{ext}}(\vec{r}) + \frac{4\pi\hbar^2 a}{m}|\psi(\vec{r})|^2\right)\psi(\vec{r}). \tag{2.14}$$

This equation serves as the starting point for most theoretical examinations on BEC. Its structure is that of a Schrödinger equation with an additional nonlinear term. Since $|\psi(\vec{r})|^2 = n(\vec{r})$, the additional term can be understood as an energy term due to the collisions between the atoms, the rate of which is proportional to the local density of the gas. In this approach the local interactions between single particles are taken into account in some averaged way. For this reason this term is commonly called the *mean field energy*. Depending on the sign of the scattering length a it is either energetically favorable for the gas to stretch over a larger volume ($a > 0$, repulsive interactions) or smaller volume ($a < 0$, attractive interaction). Sign and magnitude of a thus determine shape and even stability of the condensate [45, 46].

Most experiments are performed in a regime, where the mean field energy is much larger than the kinetic energy. In this case one can neglect in (2.14) the kinetic energy and deduce for the more common case of positive scattering lengths a simple expression for the condensate density $n(\vec{r})$:

$$n(\vec{r}) = \frac{\mu}{U_0}\left(1 - \sum_{i=1}^{3}\frac{r_i^2}{R_i^2}\right). \tag{2.15}$$

Here $U_0 = \frac{4\pi\hbar^2 a}{m}$ and $R_i^2 = \frac{2\mu}{m\omega_i^2}$ are the so called *Thomas-Fermi radii* along the spatial coordinate r_i. This expression is defined for $r_i \leq R_i$; the density equals zero elsewhere. The Thomas Fermi approximation describes in most experiments the density distribution well, but fails close to $r_i = R_i$, since then the differential operator in (2.14) can no longer be neglected.

Within the Thomas Fermi approximation the atoms move freely inside the condensate, since the mean field energy term and the external potential cancel exactly, yielding an

---

[1] In some texts ψ is also referred to as the *order parameter*. The name *wave function* refers to the fact, that ψ can be used in many respects like a single particle wave function in calculations.

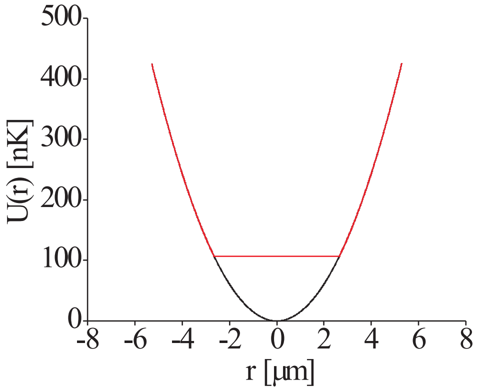

Figure 2.3: The effective potential (red curve) in Thomas-Fermi approximation consists of the external potential (black curve) plus the mean field energy. Over the occupied volume of the gas, the sum is flat due to cancellation of the two terms, and an offset equal to the chemical potential remains. The shown potentials are plotted with parameters from the trap used in our experiments in the most confining direction and for $N = 10^5$ ^{87}Rb atoms

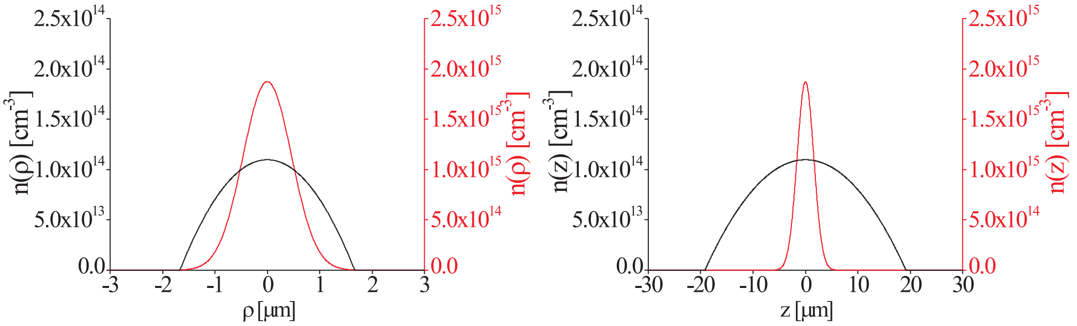

Figure 2.4: Cuts through Thomas-Fermi density profiles (black) for 10^4 ^{87}Rb atoms in a trap with parameters as used in the experiments. The used trap provides stronger confinement in radial direction (left picture) than in axial direction (right picture). For comparison, the ground state of a noninteracting gas is also shown (red). For a better comparison, the Gaussian ground state profiles have been scaled down by a factor of 10.

effective potential as shown in figure 2.3. In figure 2.4 the density distribution is given for the same trap parameters as above, showing clearly how the trapped cloud becomes larger due to the repulsive interactions.

2.2 Properties of two species condensates

A Bose condensed system with two different atomic species exhibits new degrees of freedom, since there are two distinguishable classes of particles. Deviations from the one component system will depend largely on the interaction between the species. In two limiting situations, namely the case of many atoms of both classes and the case of few atoms of the second species, it is possible to derive simple models describing the emerging system.

2.2.1 Gross-Pitaevski and Thomas-Fermi limit

General theoretical considerations

Closest to the discussion in the last section is the situation when there are many atoms of both species.

The value of the critical temperature for the single species interacting Boson gas was changed only slightly as compared with the ideal gas case. Similarly one expects this to be also valid for the two component BEC since the presence of the other species is mediated by the same type of interactions. Indeed, in experiments on sympathetic cooling of one atomic species with another one down to the critical temperature, the phase transition occurred in the expected range for the critical temperature of single species transition [47].

As in the single species case, more dramatic effects take place for the properties of the condensed phase itself. I concentrate in the following part on the density distribution of the mixture.

The system can be described again as a many body system in second quantized notation. The first species as well as the second one can be described by field operators acting on states in the space spanned by a basis of Fock states $|N_0, N_1, \cdots >_1$ and $|N_0, N_1, \cdots >_2$; the entire state of the system can be described in the basis of tensor products of Fock states

$$|N_0^1, N_0^2, N_1^1, N_1^1, \cdots > := |N_0, N_1, \cdots >_1 \otimes |N_0, N_1, \cdots >_2 . \tag{2.16}$$

A general operator acting on this state is also a tensor product of operators acting on the composite Fock state. Operators acting only on one species, like the field operators $\hat{\Psi}_1$, $\hat{\Psi}_1^\dagger$, $\hat{\Psi}_2$ and $\hat{\Psi}_2^\dagger$, are in this notation tensor products with the identity operator acting on the respective other part of the Fock state. To keep the notation simple, we define the short forms $O_1 \otimes \hat{\mathbf{1}}_2 =: O_1$ and $f(\vec{r}, \vec{r}')(\hat{\mathbf{1}}_1 \otimes \hat{\mathbf{1}}_2) =: f(\vec{r}, \vec{r}')$. In this notation, the basic Hamiltonian of the problem is in analogy to (2.9) given by

$$\begin{aligned}
\hat{H} = &\int d^3r\, \hat{\Psi}_1^\dagger(\vec{r}) \left(-\frac{\hbar^2}{2m_1} \nabla^2 + V_{\text{ext},1}(\vec{r}) \right) \hat{\Psi}_1(\vec{r}) \\
&+ \int d^3r\, \hat{\Psi}_2^\dagger(\vec{r}) \left(-\frac{\hbar^2}{2m_2} \nabla^2 + V_{\text{ext},2}(\vec{r}) \right) \hat{\Psi}_2(\vec{r}) \\
&+ \frac{1}{2} \int d^3r\, d^3r'\, \hat{\Psi}_1^\dagger(\vec{r}) \hat{\Psi}_1^\dagger(\vec{r}') V_{\text{coll},11}(\vec{r} - \vec{r}') \hat{\Psi}_1(\vec{r}') \hat{\Psi}_1(\vec{r}) \\
&+ \frac{1}{2} \int d^3r\, d^3r'\, \hat{\Psi}_2^\dagger(\vec{r}) \hat{\Psi}_2^\dagger(\vec{r}') V_{\text{coll},22}(\vec{r} - \vec{r}') \hat{\Psi}_2(\vec{r}') \hat{\Psi}_2(\vec{r}) \\
&+ \frac{1}{2} \int d^3r\, d^3r'\, \hat{\Psi}_1^\dagger(\vec{r}') \hat{\Psi}_2^\dagger(\vec{r}) V_{\text{coll},12}(\vec{r} - \vec{r}') \hat{\Psi}_1(\vec{r}') \hat{\Psi}_2(\vec{r}).
\end{aligned} \tag{2.17}$$

Some of the simplifications of the preceding sections can be applied immediately. The expressions for the interaction potentials can be cast in the same form as (2.12), with the corresponding scattering lengths a_{11} and a_{22} instead of a. Similarly the expression for $V_{\mathrm{coll},12}$ can be derived by substituting the interspecies scattering length a_{12} for a, the reduced mass m_{12} instead of m and 2π instead of 4π since the scattered particles are no longer indistinguishable. Moreover we restrict ourselves to the case $V_{\mathrm{ext},1}(\vec{r}) = V_{\mathrm{ext},2}(\vec{r})$. This is fulfilled in the particular problem for the elements of interest to us, namely ^{133}Cs and ^{87}Rb in their double polarized states $|4,4\rangle$ and $|2,2\rangle$ respectively. In this state the magnetic moments of both atoms equal one Bohr magneton, and since the trapping potentials depend only on $\vec{\mu}\cdot\vec{B}_{\mathrm{ext}}$ (cf. section 3.4), they are equal in both cases. In this treatment, the different gravitational potentials due to the different masses are neglected.

These approximations are valid regardless of the number of atoms involved. In the case of many atoms of both species one can also apply all the simplifications of the single species case leading to the Gross-Pitaevski equation (2.14). From an operator equation acting on two tensored Hilbert spaces we arrive here at two coupled differential equations, which have the form of modified Gross-Pitaevski equations:

$$\begin{aligned}
\mu_1\psi_1(\vec{r}) &= \left(-\frac{\hbar^2\nabla^2}{2m_1} + V_{\mathrm{ext}}(\vec{r}) + \frac{4\pi\hbar^2 a_{11}}{m_1}\left|\psi_1(\vec{r})\right|^2 + \frac{2\pi\hbar^2 a_{12}}{m_{12}}\left|\psi_2(\vec{r})\right|^2\right)\psi_1(\vec{r}) \\
\mu_2\psi_2(\vec{r}) &= \left(-\frac{\hbar^2\nabla^2}{2m_2} + V_{\mathrm{ext}}(\vec{r}) + \frac{4\pi\hbar^2 a_{22}}{m_2}\left|\psi_2(\vec{r})\right|^2 + \frac{2\pi\hbar^2 a_{12}}{m_{12}}\left|\psi_1(\vec{r})\right|^2\right)\psi_2(\vec{r})
\end{aligned} \tag{2.18}$$

In analogy to the basic Gross-Pitaevski equation (2.14) these equations can be understood as Schrödinger equations for the condensate wave functions, modified by the local collisional interactions. Again as in the case of a single species condensate, one can further proceed to a Thomas-Fermi like approximation by neglecting all kinetic energy operators. The resulting equations for the density distributions n_1 and n_2 are given by

$$\begin{aligned}
\mu_1 &= V_{\mathrm{ext}}(\vec{r}) + g_{11}n_1(\vec{r}) + g_{12}n_2(\vec{r}) \\
\mu_2 &= V_{\mathrm{ext}}(\vec{r}) + g_{22}n_2(\vec{r}) + g_{12}n_1(\vec{r}).
\end{aligned} \tag{2.19}$$

Here the coupling constants g_{11}, g_{22} and g_{12} can be deduced from (2.18) as

$$\begin{aligned}
g_{11} &= \frac{4\pi\hbar^2 a_{11}}{m_1} \\
g_{22} &= \frac{4\pi\hbar^2 a_{22}}{m_2} \\
g_{12} &= \frac{2\pi\hbar^2 a_{12}}{m_{12}}.
\end{aligned} \tag{2.20}$$

An algorithm for solving these equations in a self-consistent way is proposed in [48]. The trap volume is divided in four parts G_1, G_2, G_{12} and G_0 populated by species 1 alone, species 2 alone, both species simultaneously and no atoms at all. For these three parts the density distributions can be derived from (2.19) as

$$\begin{array}{llcl@{\qquad}lcl}
G_0: & n_1 & = & 0 & n_2 & = & 0 \\
G_1: & n_1 & = & \frac{\mu_1 - V_{\text{ext}}(\vec{r})}{g_{11}} & n_2 & = & 0 \\
G_{12}: & n_1 & = & \frac{g_{22}(\mu_1 - V_{\text{ext}}(\vec{r})) - g_{12}(\mu_2 - V_{\text{ext}}(\vec{r}))}{g_{11}g_{22} - g_{12}^2} & n_2 & = & \frac{g_{11}(\mu_2 - V_{\text{ext}}(\vec{r})) - g_{12}(\mu_1 - V_{\text{ext}}(\vec{r}))}{g_{11}g_{22} - g_{12}^2} \\
G_2: & n_2 & = & 0 & n_2 & = & \frac{\mu_2 - V(\vec{r})_{\text{ext}}}{g_{22}}
\end{array} \tag{2.21}$$

For fixed chemical potentials, the boundaries between these different phases are given by the condition of each distribution being continuous. The value for the chemical potentials is determined as usual by $\int d^3r\, n_i(\vec{r}) = N_i$.

This ansatz is valid for $g_{11}g_{22} > g_{12}^2$. Outside this range the system is dominated by the interspecies interaction and becomes unstable [27, 49]. This can be understood by noting that the system will distribute itself over the volume as to minimize its total energy. For $g_{12}^2 > g_{11}g_{22}$ and $g_{12} > 0$ (i. e. repulsive interaction) this is achieved by a total separation between the phases with no overlap between the distributions. Since some overlap is required for having the interaction resulting in any effect, this clearly does not correspond to a physical situation. For $g_{12}^2 > g_{11}g_{22}$ and $g_{12} < 0$ (attractive interaction) the energy is minimized by collapsing into an infinitesimal small volume, a clearly unphysical behavior again.

Numerical results for a Rubidium/Cesium mixture

In order to illustrate the results of the preceding section, I apply the formulae to the problem of interest, namely a mixture of ^{133}Cs and ^{87}Rb in a magnetic trap as realized in the our experiment (cf. section 3.4). As discussed later in greater detail, the trap provides a harmonic potential with cylindrical symmetry. The trap parameters are such, that the confinement in ρ-direction is much stronger than in z-direction. This means that the atomic clouds are cigar shaped. All cuts through the density distribution, which are shown below, are perpendicular to the z-direction. Details for the calculation of density profiles for a slightly simplified system (spherical trap instead of a cylindrical symmetry) can be found in [50].

The relevant known values for the used atoms are

$$\begin{array}{lcll}
m_{\text{Rb}} & = & 1.443161 \cdot 10^{-25}\ \text{kg} & [51] \\
m_{\text{Cs}} & = & 2.206947 \cdot 10^{-25}\ \text{kg} & [52] \\
a_{\text{Rb}} & = & 104 a_0 & [53] \\
a_{\text{Cs}} & = & 2400 a_0 \text{ at } 0\ \text{G} & [54]
\end{array}$$

Here a_0 is the Bohr radius. The scattering length $a_{\text{Rb,Cs}}$ is not known in sufficient accuracy to date. Current estimates for $a_{\text{Rb,Cs}}$ are discussed in appendix B. The most probable value is assumed to be in the range between 300 a_0 and 500 a_0 [55]. From the known values for Cesium and Rubidium and the stability condition above, one can expect stable mixtures for $-493a_0 < a_{\text{Rb,Cs}} < 493a_0$.

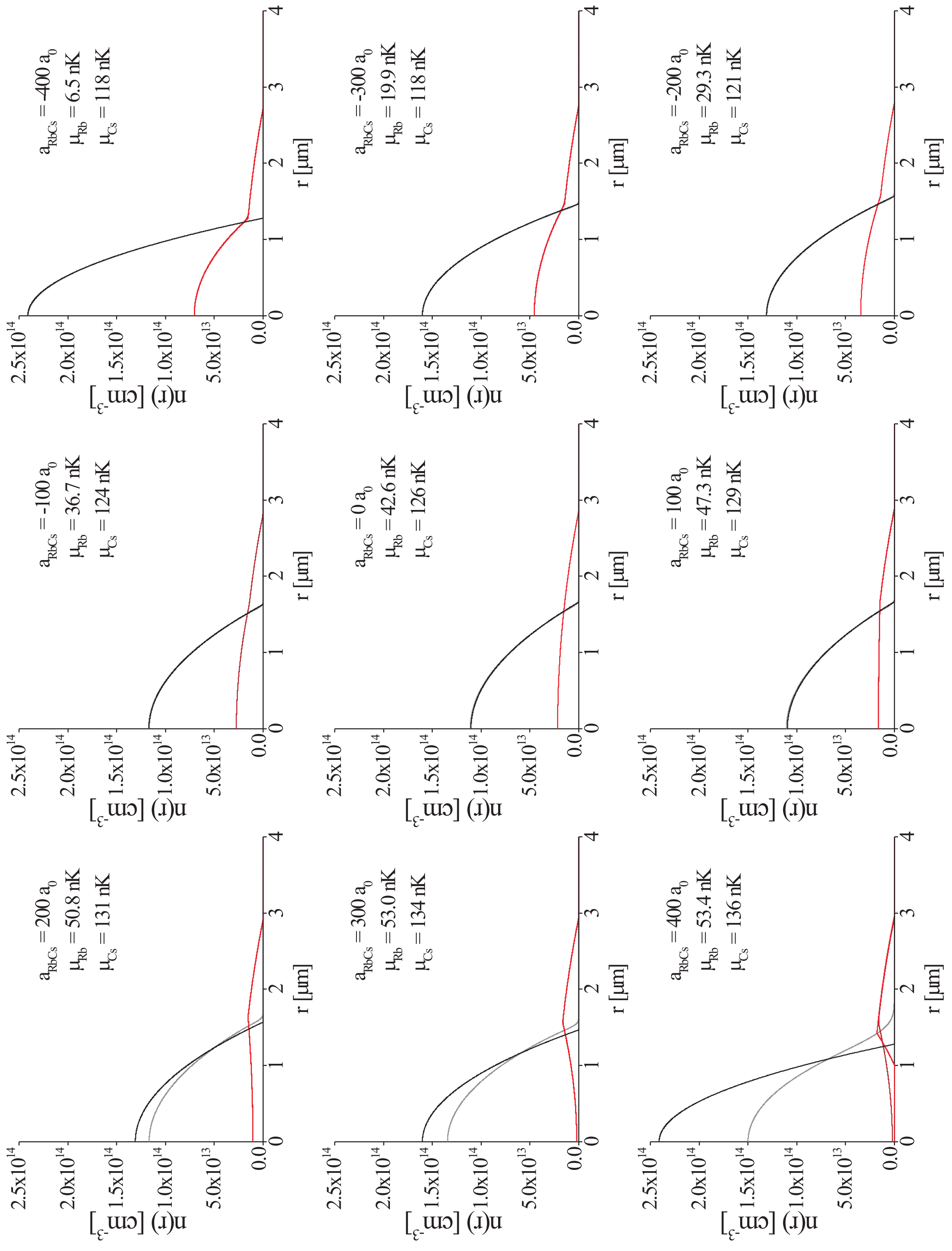

Figure 2.5: Density distributions of ^{133}Cs and ^{87}Rb double condensates with large atom numbers. The quoted chemical potentials are determined within the Thomas-Fermi approximation. For details see the description in the text.

In order to show the dominant influence of this parameter on the mixture structure, in figure 2.5 density profiles for 10^4 Cesium and 10^4 Rubidium atoms are shown with $a_{\text{Rb,Cs}}$ varying from $-400\ a_0$ to $+400\ a_0$. Profiles calculated according to the Thomas-Fermi approximation are plotted in black (Rubidium) and red (Cesium). Density profiles calculated numerically according to the more exact Gross-Pitaevski equation (2.18) are plotted in gray (Rubidium) and wine red (Cesium). In most plots the approximation fits so well to the numerical solution, that the lines overlap nearly completely. Deviations can still be seen in these cases at phase boundaries, where steep edges within the approximation are smoothed out in the numerical calculation. For higher repulsive interactions, there are clear deviations from the approximation. In these situations, the Rubidium is located at the phase boundary, such that the density distribution varies fast in space and the derivative terms can not be neglected any longer.

One can clearly observe in the plots how Cesium is dragged into the Rubidium cloud for attractive interactions and pushed out more and more for repulsive interaction. Because of the much greater interaction between the Cesium atoms as compared to the interaction between Rubidium (scattering length for Cesium-Cesium collisions is 2400 a_0 whereas the figure for Rubidium-Rubidium collisions is 105 a_0), Cesium is pushed towards the outer part, occupying a larger volume and reducing thus its density and interaction energy.

The results confirm that in the domain of many atoms for both species, the mixture can be understood analogously to the single species case. As in the single species case, the Thomas-Fermi approximation yields overall an satisfactory agreement with the Gross-Pitaevski equation.

A similar theoretical investigation has been performed in 1998 for double condensates consisting of Rubidium and Sodium in a spherical trap [56]. Qualitatively similar results as in figure 2.5 were obtained by implementing the numerical code on a Cray supercomputer system. Due to technological advances and a different algorithmic approach, the same problem in its full cylindrical geometry can be treated six years later with an off-the-shelf PC (2 GHz clock speed, 1 GB RAM). Details on the numerical algorithms are presented in appendix C.

2.2.2 Few particles interacting with a macroscopic quantum wave

Transition temperature

For a bosonic system of few atoms, most approximations applicable for many particle systems used above fail. This is due to the much lower density and correspondingly lower critical temperatures. I concentrate here first on the implications for the phase transition behavior, and later on the shape of the ground state.

Because the system can not be described by formulae of the preceding section valid in the thermodynamical limit, the macroscopic occupation of the ground state is qualitatively different as compared with the many particle case. Particularly the semiclassical approximation of a continuous function for the density of states breaks down. Leading to the definition of the energy density $\rho(E)$ in equation (2.2) was the assumption, that all

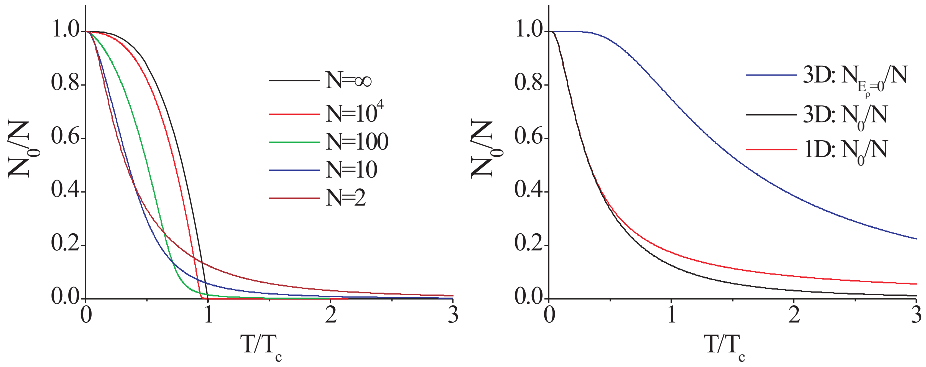

Figure 2.6: Population of the ground state for small samples of an interaction free bosonic gas. The atoms are assumed to be trapped in an atom trap with the same cylindrical symmetry and steepness as the atom trap used in the experiments for many atoms. T_c is the critical temperature of a many particle system as calculated via (2.5). In the left picture the ground state population is calculated for several total atom numbers. On the right side, for the case $N = 2$ the population in the ground state (black), the total population in the radial ground state (red) $n_{E_\rho=0} = \sum_{E_z} n_{E_z,E_\rho=0}$ summed over all axial states and the population of the ground state according to a one dimensional model (blue) is shown. For details see the text.

temperatures of interest - namely T_c - be small compared with the discrete spacing $\hbar\omega$ between energy levels. Without this approximation the defining equation for the chemical potential takes the form

$$\sum_{\text{all states } |n>} f_{\mathrm{B}}(E_n) = \sum_{\text{all states } |n>} \frac{1}{\exp\left((E_n - \mu)/kT\right) - 1} = N \tag{2.22}$$

As the energies of a harmonic potential are well known, for low temperatures and small particle numbers this sum can be performed directly [37]. In figure 2.6 the population of the ground state for such systems confined in an atom trap is plotted. Again, the characteristics of the trap are the same as for the trap implemented in the experiments. The black curve for $N = \infty$ is the theoretical curve according to (2.8). The red curve for $N = 10^4$ atoms is still in good agreement with the theoretical curve, T_c deviating by a few percent from the expected value in the theoretical limit.

For less atoms, the transition to a macroscopically populated ground state is much smoother than in the many particle case. This can be explained by the fact that for few particles the role of fluctuations is not as suppressed as in the thermodynamic limit, leading to much less pronounced transition behavior. Also the macroscopic population of the ground state takes place at lower temperatures than predicted. Intuitively one can also understand this behavior as a consequence of a smaller bosonic amplification of scattering events into the ground state. This bosonic enhancement factor is proportional to the number of atoms already populating the ground state.

In a more quantitative way, the different shape of the population curves for small atom numbers as compared to the large atom limit can be understood by taking the cylindrical shape of the trap into account. The geometry of the trapping potential becomes more important for the system's behavior as soon as the interaction between the particles is reduced due to the lower density. As mentioned above, the radial trap frequency ω_ρ is roughly ten times higher than the axial frequency ω_z, leading to a much smaller energy level difference for axial levels. The overview in table 2.1 shows, that for small atom numbers the expected transition temperature gets close to the radial energy spacing $\hbar\omega_\rho$. Thus by lowering the temperature, the radial degrees of freedom freeze out first, limiting the available number of states for the system. This can be seen in the right half of figure 2.6 (blue curve). Lowering the temperature further, all atoms are in the radial ground state and the sum in equation (2.22) is effectively performed over the states of a one dimensional harmonic oscillator describing the axial energy eigenstates. Due to the lower degeneracy the available phase space for the system is thus much smaller than in the three dimensional case, resulting in a change of the shape of the population curve (black curve). Using a strictly one dimensional model by neglecting all radial states in (2.22) reproduces the ground state population very well in the region of frozen out radial degrees of freedom (red curve).

While for the case of 100 atoms in the sample it might be still justified to use the concept of a phase transition, the onset of macroscopic ground state population is smeared out over a large temperature range for the cases of $N = 10$ and $N = 2$. Nevertheless, in the following I use the term *condensed phase* for the atoms in the ground state. The transition has lost its sharply defined transition temperature, but still shows a clear bosonic signature. The system populates the ground state with a large fraction at a finite temperature, in marked difference to particles obeying Boltzmann statistics.

In order to cool down a small number of atoms close to the ground state, a sympathetic cooling technique using a second atomic species seems advantageous. The application of the standard evaporative cooling technique offers only poor control on the number of atoms remaining at the and of the cooling process. Also, this technique would require different starting conditions than can be realized within our experiment.

If another atomic species is present in the trap, characteristics of the transition to the condensed state are changed by the interspecies interaction. In the following I examine

Table 2.1: Transition temperatures for different atom numbers. Listed are the transition temperature $T_{c,\mathrm{cont}}$ as derived from the semiclassical ansatz of a continuous energy spectrum (2.5) and the transition temperature $T_{c,\mathrm{dis}}$ obtained by discrete summation taken from figure 2.6. For small atom numbers the last number is an extrapolation of the last, linearly rising part of the curve towards $N_0/N = 0$, since no clear transition is observed. For comparison, the radial energy levels differ by $\hbar\omega_\rho = 13$ nK and the axial energy levels by $\hbar\omega_z = 1.1$ nK.

N	$T_{c,\mathrm{cont}}$	$T_{c,\mathrm{dis}}$
10^4	117 nK	110 nK
100	25 nK	≈ 22 nK
10	12 nK	≈ 7 nK
2	6.8 nK	$\approx 3 - 4$ nK

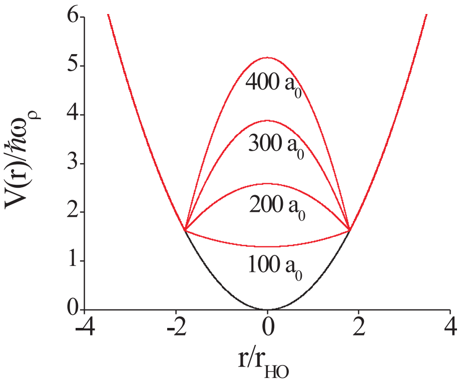

Figure 2.7: Effective potentials for a few Cs atoms in a harmonic trap with Rb atoms. Shown are the resulting potentials due to an external magnetic field and a mean field interaction with 10^4 Rb atoms. The different potentials result from interspecies scattering lengths ranging from $100 \ldots 400$ a_0, a_0 being one Bohr radius. Length units are in harmonic oscillator units $r_{\mathrm{HO}} = \sqrt{\frac{\hbar}{m_{\mathrm{Rb}}\omega_\rho}}$ and energy units in multiple of $\hbar\omega_\rho$.

these modifications. For the relevant case of this other species having a much larger atom number than the few particle system, further approximations facilitate a quantitative description. Due to the low density of the small system, all interactions within the small system and also effects onto the larger system can be neglected. The larger system acts thus like a reservoir at zero temperature, to which the small system couples to via the interspecies interaction.

The large system can described by a Thomas-Fermi-profile. In analogy to figure 2.3, it acts like another external potential V_{TF} on the small sample according to

$$V_{\mathrm{TF}}(\vec{r}) = \begin{cases} \mu_1 \frac{a_{11}}{a_{12}} \frac{m_1}{2m_{12}} \left(1 - \sum_{i=1}^3 \frac{r_i^2}{R_i^2}\right) & \text{for } \sum_{i=1}^3 \frac{r_i^2}{R_i^2} \leq 1 \\ 0 & \text{for } \sum_{i=1}^3 \frac{r_i^2}{R_i^2} \geq 1. \end{cases} \tag{2.23}$$

Here the larger system is denoted by 1, the smaller by index 2. μ_1 is the chemical potential of the larger system and m_{12} the reduced mass; the Thomas-Fermi radii are defined as for equation (2.15).

The effect of this additional potential is studied for the case of 10^4 Rb atoms and a few Cs atoms. Depending on the number of atoms in the large system and on the interspecies interaction strength parameterized by a_{12}, the resulting total external potential $V(\vec{r}) = 1/2m(\omega_\rho^2\rho^2 + \omega_z^2 z^2) + V_{\mathrm{TF}}(\vec{r})$ is determined. For $\frac{a_{11}}{a_{12}} \leq 0$, i. e. an attractive interaction $a_{12} \leq 0$ for the Rubidium-Cesium system, the total potential remains harmonic in its inner part with higher trap frequencies. As a consequence, except of a shift to higher transition temperatures the system will behave very similar to the one species case. I concentrate in the remaining part of this chapter on the case $a_{12} > 0$, for which the system can behave in a qualitatively different way, if the curvature of the added potential due to the interspecies interaction exceeds the curvature of the external trap potential. For values ranging from $a_{12} = 100 \ldots 400$ a_0, resulting effective potentials are plotted in figure 2.7.

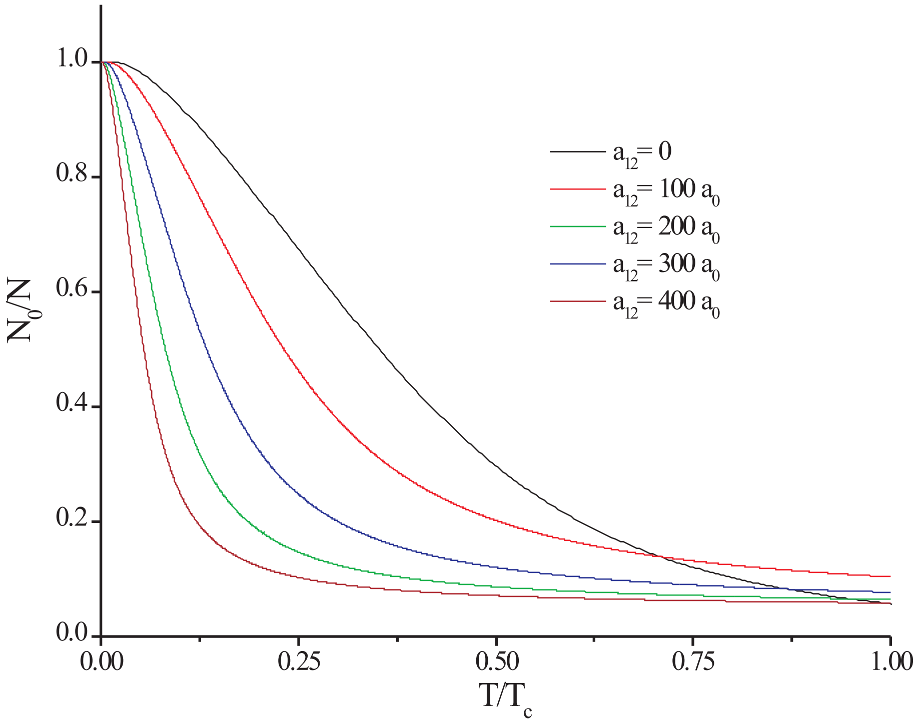

Figure 2.8: Population of the ground state of a system 10 Cesium atoms interacting with a condensate of 10^4 Rubidium atoms. The population is calculated for five different Rubidium-Cesium scattering lengths a_{12}. $T_c = 12$ nK is the critical temperature according to the semiclassical large-system approximation given in equation (2.5).

Because of the neglected Cesium–Cesium interaction, the Cesium sample can be described with a linear Schrödinger equation with the effective potentials plotted in figure 2.7 being used as the potential term. The 30 lowest eigenvalues of this equation were determined numerically. Details of the numerical method are given in appendix C. Truncating the infinite sum given in equation (2.22), these eigenvalues can be used to calculate the chemical potential $\mu(T)$ and the ground state population $N_0(T)/N$ of the Cesium sample in analogy to the calculations presented in figure 2.6. The results for a sample of 10 Cesium atoms immersed in a BEC of 10^4 Rubidium atoms, with the interspecies scattering lengths varying from 0 to 400 Bohr radii, are plotted in figure 2.8. The error due to the truncation of the infinite sum in equation (2.22) can be estimated to be less than a few percent over the plotted temperature range.

For increasing values of the interspecies scattering length, the ground state is populated at lower temperatures. The reason for this effects is the smaller spacing of the energy levels with increasing interaction strength, as revealed by the numerical calculation. This scales down all energies appearing in the problem, including T_c.

Further the population increases less smooth in dependance of the temperature. Thus the condensation has a more transition-like behavior than without the interspecies interaction.

Ground state

In analogy to the discussion of condensed many particle systems, I will now describe the ground state of a system with N atoms in the condensed phase, neglecting atoms in thermal states with a higher temperature. For large systems, this approach is justified ultimately by the excellent agreement between predictions and experimental results. It is however not clear, whether this approach is also valid for small systems, since fluctuations in the atom number by interaction with a thermal atom cloud may have a stronger relative impact here. A detailed analysis of this question requires a treatment of the many particle Hamiltonian without the approximation $T = 0$, which is beyond the scope of this thesis [57, 58].

The aim in the remaining part of this chapter is to gain insight into the structure of the ground state and to identify qualitatively different behavior from the many particle case. Note, however, that the results might still have to be modified according to a more exact albeit more complicated theory.

While the general operator equation (2.17) describing coupled systems is also valid for small systems, the coupled Gross-Pitaevski equations (2.18) derived thereof are certainly not correct. This stems from the fact that the approximation $\sqrt{N} \approx \sqrt{N-1}$ has been used, allowing to replace e. g. the operator $\hat{a}^\dagger$ by $N\,\hat{\mathbf{1}}$. Instead we can simplify the expansion (2.11) for the field operator as

$$\Psi^\dagger(\vec{r},t) = \psi(\vec{r},t)\hat{a}_0^\dagger. \tag{2.24}$$

This uses explicitly the fact that we assume all atoms being in the ground state. Note that, according the discussion on the transition behavior on small atomic samples, this simplification becomes valid only at significantly lower temperatures than the semiclassically calculated temperature T_c. Inserting this expression into the Hamiltonian and using the Heisenberg equation of motion, we obtain a differential equation for $\psi(\vec{r},t)$. Using the ansatz $\psi(\vec{r},t) = \psi(\vec{r})e^{-i\mu t/\hbar}$ this reduces again to a Gross-Pitaevski like equation. The other half of the coupled equation describing the large system can be obtained as above, so that corrections only apply in the equation describing the small system:

$$\begin{aligned}
\mu_1\psi_1(\vec{r}) &= \left(-\frac{\hbar^2\nabla^2}{2m_1} + V_{\text{ext}}(\vec{r}) + \frac{4\pi\hbar^2 a_{11}}{m_1}\left|\psi_1(\vec{r})\right|^2 + \frac{2\pi\hbar^2 a_{12}}{m_{12}}\left|\psi_2(\vec{r})\right|^2\right)\psi_1(\vec{r}) \qquad (2.25)\\
\mu_2\psi_2(\vec{r}) &= \left(-\frac{\hbar^2\nabla^2}{2m_2} + V_{\text{ext}}(\vec{r}) + \frac{4\pi\hbar^2 a_{22}}{m_2}\frac{N_2-1}{N_2}\left|\psi_2(\vec{r})\right|^2 + \frac{2\pi\hbar^2 a_{12}}{m_{12}}\left|\psi_1(\vec{r})\right|^2\right)\psi_2(\vec{r})
\end{aligned}$$

Formally the only difference is the factor $\frac{N-1}{N}$ in front of the mean field part of $\psi_2(\vec{r})$, which has a clear physical interpretation. So one expects no collisional interaction for only one particle present, which is reflected by the fact that the whole mean field term vanishes for $N = 1$. For $N \gg 1$, we have $N(N-1) \approx N^2$, which recovers the expressions for many particle systems (2.18) as expected.

Although the rest of the equations is formally identical, the mean field energy due to $\psi_2(\vec{r})$ is much smaller than in the many particle case. This is incorporated into the equations by the normalization condition for $\psi(\vec{r})$, and also in a much smaller resulting chemical potential. For the small system, the kinetic energy operator can not be neglected any more, and the Thomas Fermi approximation can only be applied for the large system with index 1.

2.3 Conclusions

In this chapter I have outlined the theoretical framework for the description of ultracold, interacting Bose gases. A semiclassical approach allows to estimate the transition temperature for Bose-Einstein Condensation and provides also an intuitive picture in terms of overlapping atomic de Broglie waves.

Properties of the condensed state are deduced from a fully quantum mechanical treatment. The interaction between the atoms is taken into account with a mean field approach.

A mixture of two degenerate gases can be described in the thermodynamic limit by extending the single species formalism. A new parameter, the interspecies interaction strength, is added to the system and determines to a large extent properties of the mixture.

First steps for the realization of such experiments with two atomic species have been performed within this thesis. This is the focus of the last part of this thesis. The experimental techniques resemble very much the methods employed for the realization of single species condensates.

In view of possible experimental approaches, the most important quantity to consider is the phase space density. As written explicitly in equation (2.7), quantum degeneracy is reached if the phase space density of the atomic ensemble reaches unity. This can be achieved by simultaneously increasing the density of the atoms and lowering their temperature.

Like in most BEC experiments, the Bonn BEC experiment employs a two step process. First, atoms are cooled and trapped in a magneto-optical trap (*MOT*). This step is detailed in section 3.3. Since the phase space density attainable by laser cooling techniques is limited, evaporative cooling is applied as a second step. Evaporative cooling is a very efficient cooling method developed originally for reaching BEC in hydrogen without laser cooling [59]. Section 3.5 is devoted to this topic.

Unfortunately, the two main techniques of collecting atoms in a MOT and cooling the atoms by evaporative cooling are not directly compatible. This is the main origin of the technical complexity of the experimental implementation.

Evaporative cooling works only for an atom cloud confined in a conservative trap, which is not provided by a magneto-optical trap. The experimental solution chosen here is to store the atoms in a purely magnetic trap, generating a nearly perfectly conservative and dissipation free trap. Our magnetic traps are described in 3.4.

Further, evaporative cooling is — compared to most laser cooling techniques — a slow process. It turns out, that the atoms have to be stored for several tens of seconds with only negligible environmental interaction. This is realized by providing a background pressure on the order of 10^{-11} mbar, which implies storage times on the order of 100 s [60]. On the other hand, for a magneto-optical trap to collect efficiently a large number of atoms from the background vapor, a gas pressure on the order of 10^{-8} mbar to 10^{-9} mbar is necessary. This discrepancy is resolved in our experiment by constructing two MOTs in different chambers. One is operated at a pressure suitable for collecting a high number of atoms. The atoms are then transported to a second MOT located in a chamber at a lower pressure well adapted to magnetic trapping and evaporative cooling [61, 62]. This solution lays down the principal design of our vacuum system, which is described in section 3.1.

The experiments envisioned to explore the interaction of two different species are built on very similar techniques, but require also additional methods. This is especially eminent for the case of very few or even single atoms, since the standard methods applied in BEC experiments are optimized for handling large clouds of atoms. The issue of tracing such small samples is discussed briefly in connection with the description of the detection methods used in our experiment. Further, possible techniques not implemented yet are outlined in the outlook at the end of this thesis.

Chapter 3

The route towards BEC

This chapter covers the main experimental steps and results on the way to our Rubidium BEC. After a brief description of the overall vacuum system and key components of the experiment, I report on the principal stages of our experiment. The order of the corresponding sections follows the sequence of the experimental steps as applied in a standard creation of a BEC. This comprises consecutive collecting of atoms in two MOTs, storing them in a magnetic trap and cooling them evaporatively.

In a conclusion at the end of the chapter I highlight the most critical points in this process.

3.1 Experimental setup

3.1.1 Vacuum system

The vacuum system serves as the experiment's backbone. The setup of the main apparatus is shown in figure 3.1. As mentioned in the last section, two regions of different pressure are necessary for the realization of our "road map" towards BEC. These two parts are at the top and the bottom of the setup.

The last steps for obtaining BEC are performed in the glass cell at the bottom of the apparatus. A pressure on the order of 10^{-11} mbar is achieved through the combination of a turbo molecular pump and a NEG pump. This pressure is measured with an UHV gauge (Leybold Ionovac IE 514). It is located at the central part of the apparatus, roughly 20 cm above the glass cell. The gauge is switched off during experiments to avoid a degradation of the vacuum by the hot ionizing wire. The turbo pump (Pfeiffer TCM180) provides a pump rate of 180 l/s. For its operation, a prepump providing a vacuum of 10^{-3} mbar is necessary. In our setup a combination of a membrane pump and another small turbo pump is used (not shown in figure 3.1). The turbo pump has magnetic bearings and thus introduces only little mechanical vibrations. The stray magnetic fields from the bearings are negligible at the place of the experiment. The pump can be separated from the experiment by an all-metal valve. The controller and the power supply of the pump are connected to mains through an uninterruptible power supply, since a power failure results

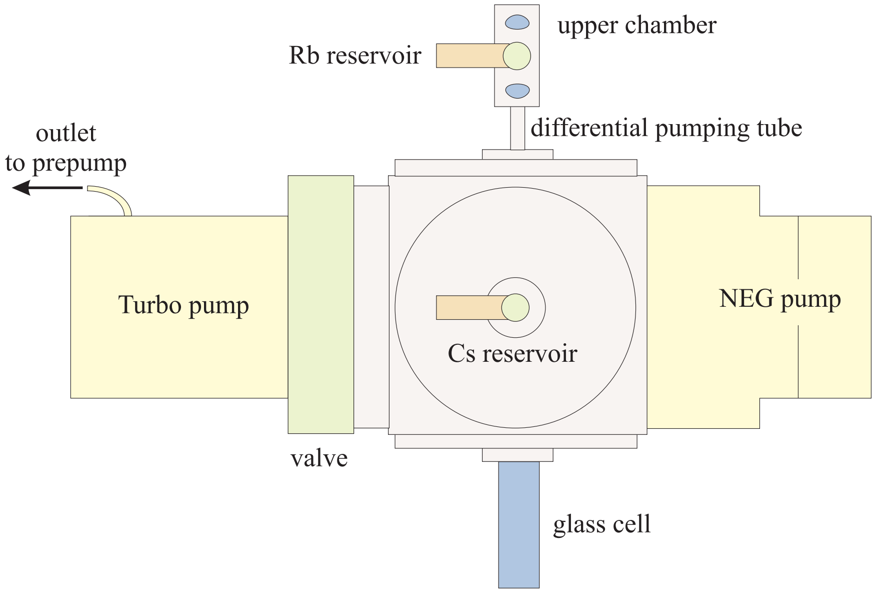

Figure 3.1: Setup of the main vacuum system, side view. Vacuum components are drawn in yellow, the vacuum gauge is opposite to the Cesium reservoir and not visible in this sketch. Atom reservoirs are in orange and connected via valves (green) to the apparatus. The crucial parts for the experiments are the glass cell at the bottom and the upper chamber at the top. The upper chamber is connected via the differential pumping tube to the main part. The distance between upper chamber and glass cell is about 50 cm.

otherwise in flooding the apparatus with atmospheric air.

Because turbo pumps are inefficient for light gases such as H_2 or He, a second UHV pump with high efficiency for these gases is implemented in the system, a Nonevaporable Getter Pump (NEG, type Saes-Sorb-AC, SAES Getters Group). This pump provides a large surface of a getter material (a Zr-V-Fe alloy), which binds chemically most elements and resolves hydrogen.

The use of the Cesium reservoir shown in figure 3.1 is described in chapter 5.1. For the experiments described in this and the next chapter it was sealed.

The other main part of the apparatus is an octagonally shaped recipient at the top together with the Rubidium reservoir. It is connected to the lower part by a tube of 8 mm length and an inner diameter of 3 mm (*differential pumping tube*). Due to these small dimensions, the tube exhibits only a small flow conductance. Therefore the upper chamber is pumped much less efficiently than the lower part. This configuration leads to significantly higher pressure in this part, such that a MOT collecting a large number of atoms (typically several 10^9 atoms) can be operated there. From the loading curve of the installed MOT, a pressure of $8 \cdot 10^{-9}$ mbar can be inferred [63]. The pressure is the result of a dynamical equilibrium between the gas flow out of the reservoir (which can be adjusted with the help of a valve) and the pump rate fixed by the connection tube.

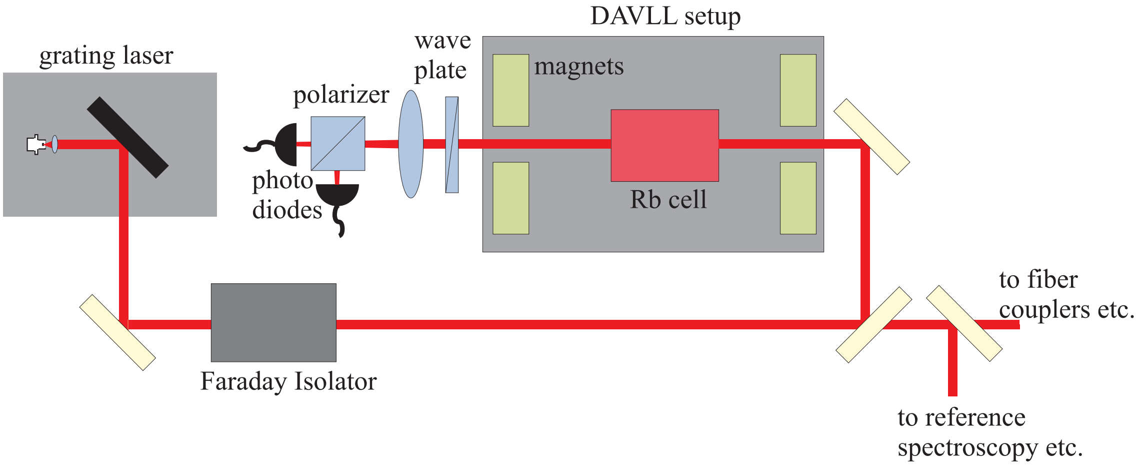

Figure 3.2: Schematic laser setup. The beam from the Littrow type grating laser is passed through a Faraday Isolator (60 dB, Gsaenger). Part of the power is split for locking the laser onto an atomic resonance, some other part is split for an additional reference method (e. g. saturation spectroscopy or beat signal measurement). The main part of the laser power is coupled into fibers (single mode polarization maintaining fibers), which guide the light to the experiment.

3.1.2 Laser system

The magneto-optical traps (cf. section 3.3) and the imaging system (cf. section 3.2.2) require near resonant laser light. The absolute frequency of these lasers has to be controlled within fractions of the natural linewidth of the trapped atoms, which is 6.1 MHz in the case of Rubidium [51]. As the optical frequency itself is on the order of 384 THz, this implies a relative precision of 10^{-8}. This can only be achieved by an active stabilization.

All used lasers are diode lasers of the external grating Littrow type [64]. Altogether four laser systems are required: two for the operation of the MOTs, one for the detection of the atoms and one reference laser to provide a frequency standard for the other three lasers. One of these lasers is homebuild and three are of the commercial DL 100 type by Toptica Photonics (München). For the operation of the two large MOTs one laser is amplified by a tapered amplifier chip. Laser and amplifier are bought as one unit from Toptica Photonics (TA 100), delivering on the order of 0.5 Watt power.

The schematic setup for one laser is illustrated in figure 3.2. The lasers are actively stabilized to an atomic transition by the *Dichroitic Atomic Vapor Laser Lock (DAVLL)* technique [65, 66]. This technique relies on the Zeeman shift of the m_F levels of the atomic gas in a magnetic field in the range of 100 G. The two orthogonally circular components of a linearly polarized laser beam have different resonance frequencies due to this shift. Two separate Doppler profiles can be obtained by scanning the laser frequency over the transition. The difference signal between these profiles yields a dispersive signal, which can be used to implement a feed-back loop in order to stabilize the laser. Details on our implementation of this technique are given in the Staatsexamenarbeit [67]. The achieved stability of the laser frequencies is limited on a short timescale by the bandwidth of the servo loop and on longer timescales by drifts induced e. g. by temperature changes. The short-time stability can be characterized with a typical linewidth of the lasers of $1-2$ MHz and the long-time stability by a drift rate of usually less than 1 MHz/h.

One drawback of the DAVLL technology is the lack of sub Doppler resolution in the obtained atomic spectra. In order to adjust the laser frequency correctly with respect to the corresponding hyperfine transition, this information is either obtained by additional saturation spectroscopies [68], or by heterodyning with the reference laser. Both the saturation spectroscopies as well as the heterodyne beat signal are displayed throughout the experiment and serve as independent monitors for the laser frequency. The beat signal, occurring at the difference signal of the heterodyned lasers, is detected with a spectrum analyzer (Advantest R4131C).

The main part of the laser power is fed into optical fibers and led to the experiment. Because of the low transversal beam quality typical of diode lasers, only about 50% of the power can be coupled into the fiber. The coupling efficiency of the amplified laser is only approximately $30-40$ %.

All lasers can be shut off by electromechanical shutters (Uniblitz, Vincent Associates) placed in the focus of telescopes before the fibers. Shutter speeds are around $20-40$ μs. All light sources and shutters are contained in a closed box to avoid any stray light.

3.2 Characterization of cold atomic clouds

This section describes the detection methods implemented at our experiment. The first part covers near resonant atom–light interaction, which is used in all detection methods, and the imaging system which was used to obtain most of the presented results.

Apart from the spatial profile of the cold cloud, the two quantities of primary interest are the atom number and the temperature of the cloud. The techniques used for obtaining these parameters are detailed in the remaining part.

3.2.1 Near resonant interaction with light

Close to resonance the main observable signals of the atom–light interaction are due to absorption and emission processes. This can be exploited either by observing absorption of a probe beam or by detecting atomic fluorescence. In the experiment both approaches are used, although absorption measurements make up the main methods.

Other methods, exploiting refractive effects of the cloud at higher detunings are not as invasive as near resonant interactions, but are more involved concerning their experimental realization and the required image processing routines. Furthermore they prove to be less sensitive than absorption imaging [34].

For near resonant light the photon scattering rate γ is given by [69]

$$\gamma = \frac{\Gamma}{2}\frac{s}{1+s+\left(\frac{2\Delta}{\Gamma}\right)^2}, \tag{3.1}$$

where Γ is the natural linewidth of the transition and $s = I/I_{\mathrm{sat}}$ is the saturation parameter. The saturation intensity I_{sat} is defined as the intensity at which the induced emission processes according to the Einstein B coefficient appear at the same rate as spontaneous emissions according to the Einstein A coefficient [70]. I_{sat} is given by [51]

$$I_{\mathrm{sat}} = \frac{\epsilon_0 c \hbar^2 \Gamma^2}{4\left|\vec{\epsilon}\cdot\vec{d}\right|^2}. \tag{3.2}$$

In this equation $\vec{\epsilon}$ is a unit vector describing the polarization of the light, e is the elementary charge and $\vec{d}$ is the expectation value of the atomic electric dipole moment operator

$$\vec{d} = e\langle F m_F|\hat{\vec{r}}|F' m'_F\rangle. \tag{3.3}$$

Here, atomic states are described by the quantum numbers F and m_F. Usually one writes $\vec{d}$ and $\vec{\epsilon}$ in spherical tensor notation, such that $\vec{\epsilon}$ has three components ϵ_{+1}, ϵ_0 and ϵ_{-1} describing σ^+, π and σ^- polarized light. The dependance of the component d_q on m_F and m'_F can then be expressed with the Wigner-Eckart theorem [71] as

$$d_q = (-1)^{F'-1+m_F}\sqrt{2F+1}\begin{pmatrix} F' & 1 & F \\ -m'_F & q & m_F \end{pmatrix}\langle F||\hat{r}||F'\rangle. \tag{3.4}$$

In the case of the ^{87}Rb atom, the ground state has two hyperfine ground levels with $F = 1$ and $F = 2$, while the F' quantum numbers in the excited state run from 0 to 3.

These formulae allow the determination of the photon scattering rates for arbitrary polarized light incident on atoms with a given population distribution in the m_F states of its ground state. Conversely, in order to interpret either fluorescence or absorption signals correctly, one has to know the polarization of the light and the state of the atoms. In an experimental situation there is usually no complete knowledge on these parameters. However, it is normally possible to approximate the m_F population distribution and to interpret obtained signals with satisfactory confidence.

3.2.2 Imaging system for absorption measurements

The principal setup for absorption measurements is shown in figure 3.3. A laser beam is collimated and directed through the atomic cloud. The cloud is imaged by two lenses onto a CCD chip. The lenses (achromats with focus length f=12 cm, 4 cm aperture) are placed to achieve a one to one imaging of the object plane onto the image plane (*4f imaging system*). The CCD chip (FT18, Philips) has 1024x1024 pixels with a size of 7.5x7.5 μm^2.

The system is used in our experiment by imaging the shadow cast from the atoms onto the CCD chip. The imaging beam is superimposed with polarizing beam splitters onto a beam of the MOT.

The resolution of the system is limited by the smallest apertures within the system and by aberration effects [72]. The smallest apertures are the opening in the coil for the creation of the magnetic trap (2 cm) and the polarizing beam splitter (cube of 2 cm length), and

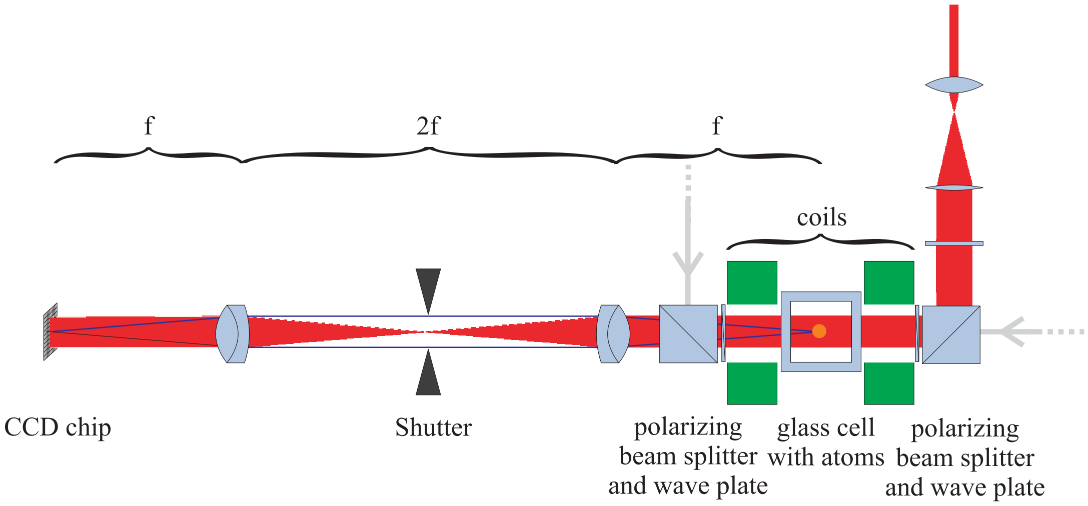
f
2f
f
coils
CCD chip
Shutter
polarizing beam splitter and wave plate
glass cell with atoms
polarizing beam splitter and wave plate

Figure 3.3: Schematic overview of the imaging system. Superimposed on the imaging beam (light red) is a beam of the optical trap (grey). The two beams are separated due to their orthogonal polarization. A shutter (Compur) is used to protect the CCD chip from leaking trap laser light. Figure not to scale.

the shutter aperture (2 cm). Aberrations are mainly induced by the 5 mm thick glass window of the glass cell and the 20 mm long beam splitter. These effects can be estimated best with a raytracing algorithm, taking into account also the imperfections of the used achromats. The point spread function was calculated using the program OSLO (OSLO LT 5.40 by Sinclair Optics). The width of the resulting spot is 34 μm. OSLO predicts a spot width of 8 μm for an optimized geometrical arrangement of the same optical components. The difference stems mainly from a different placement of the stray light shielding shutter. Also the actual alignment of the elements, which was taken to be perfect in the simulation, possibly deteriorates the achieved resolution.

Apart from the limit for the resolution due to the optical imaging system, some smearing of the imaged atom cloud stems also from the measurement principle itself. Under typical experimental conditions (imaging intensity approximately 10% of the saturation intensity, light exposure time 200 μs, controlled by the switching of an AOM (*Acousto-Optical Modulator*) about 75000 photons are scattered by one atom. One scattering process consists of an absorption process, which transfers momentum from the photon onto the atom along the direction of the imaging beam, and an emission event, which adds a recoil momentum to the atomic momentum. The spontaneous emission of photons is equally distributed over the complete solid angle. Thus the recoil momenta added up to the atomic motion constitute a random walk in momentum space. The absolute value of the transferred momentum is proportional to the square root of the total number of scattered photons. For the experimental conditions mentioned above, this amounts to about 300 recoil momenta, leading to an additional smearing of approximately 2 μm.

In figure 3.4 a comparison between the calculated resolution and the measured point

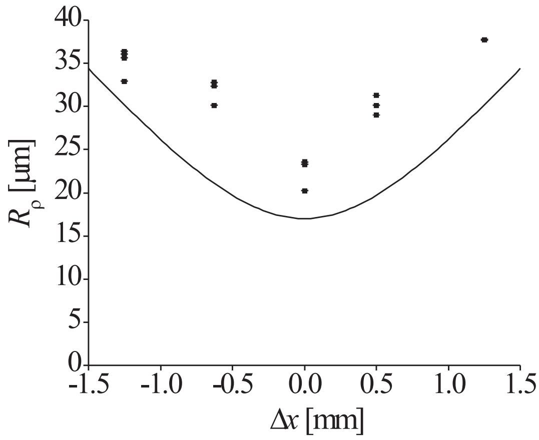

Figure 3.4: Experimental test of the imaging resolution. On the vertical axis the measured Thomas-fermi radius R_ρ of a BEC is plotted against a deviation Δx of the last lens from its optimum position. The solid line is the theoretical prediction according to a calculation using the program OSLO.

spread function is shown. As a point source a BEC was used. The Thomas Fermi radius in radial direction R_ρ has a theoretical value of 2.2 μm±0.2 μm large, as determined from the measured atom number (cf. 4.2).

The curve shows a qualitative agreement between a calculation based on the OSLO simulation and a measured defocussing due to moving the last lens of the imaging system by an amount of Δx. However, the theoretical prediction stays always below the measured values. The difference might be due to misalignments of the optical elements (e. g. off-axis centering of elements, lenses tilted with respect to the optical axis) not entering the model in OSLO.

Image Processing

In order to derive quantitative results, several images must be taken for one complete absorption measurement. If no atoms are present, the detected image $I_B(x, y)$ will have within a good approximation a structure according to

$$I_B(x, y) = P(x, y) + N(x, y). \tag{3.5}$$

Here $P(x, y)$ is the profile of the imaging beam and $N(x, y)$ sums up all noise components present without light, in particular the readout noise of the CCD chip.

If atoms are present, the term describing the light passing through the object plane will be attenuated by the atomic absorption according to Beer's law, and the detected image is

$$I_A(x, y) = P(x, y)e^{-D(x,y)} + N(x, y). \tag{3.6}$$

For a given atomic absorption cross section σ, $D(x, y)$ is proportional to the atomic cloud

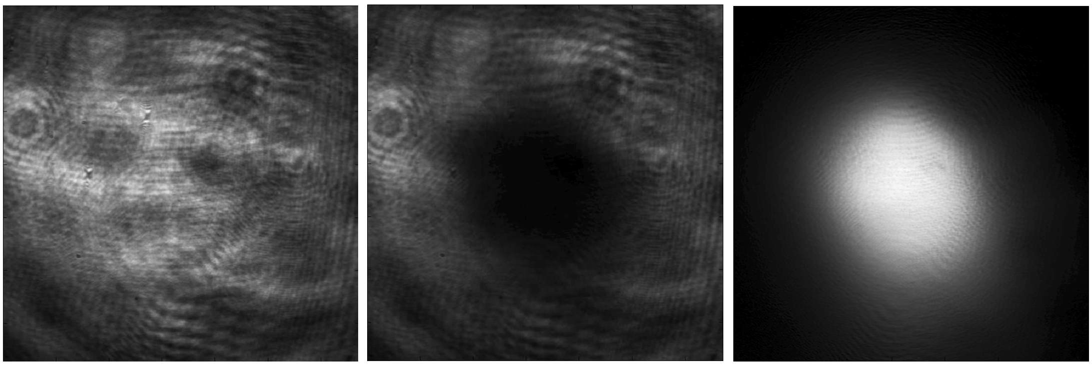

Figure 3.5: Images used for the standard image processing. The left picture shows an image obtained without atoms present. The middle picture was taken a short time before, with atoms present. The shadow in the middle stems from the atomic absorption. Both pictures are scaled to the same color encoding. The right picture shows the cloud's column density, constructed from the two previous images with the processing described in the text. The maximum intensity in the grey color code for this image corresponds to a peak column density of $2.7 \cdot 10^9$ cm^{-2}. The field of view is in all cases 5x5 mm.

column density $n_c(x,y) = \int dz\, n(x,y,z)$ along the imaging beam direction via

$$D(x,y) = \sigma n_c(x,y). \tag{3.7}$$

The relation between the absorption cross section σ and the photon scattering rate γ is given by

$$\sigma = \frac{\hbar\omega}{\Gamma I}\gamma = \frac{\hbar\omega}{2I_{\mathrm{sat}}} \frac{1}{1 + s + \left(\frac{2\Delta}{\Gamma}\right)^2}. \tag{3.8}$$

For typical atom numbers the noise term $N(x,y)$, specified by the manufacturer as 4-5 e^- is small compared to typical values of $P(x,y) \approx 1000 - 10000$ counts per pixel. If $N(x,y)$ is neglected, $D(x,y)$ can be measured by taking only two pictures. $D(x,y)$ can then be calculated as

$$D = -\ln(I_A/I_B). \tag{3.9}$$

In figure 3.5, a typical application of this algorithm is illustrated. It is striking, that even beam profiles far from a perfect Gaussian shape lead to very clean and low noise results $D(x,y)$. A more careful analysis of the neglected terms and also of other noise issues is necessary in order to obtain optimal results in the case of smaller signals, as expected for small particle numbers. This is carried out at the end of this section.

3.2.3 Temperature measurements

Temperature measurements are experimentally realized by the *time of flight* (TOF) method. The basic idea is to shut off all traps fast enough such that the cloud does not change significantly during the switching time. As the atomic clouds falls, it expands

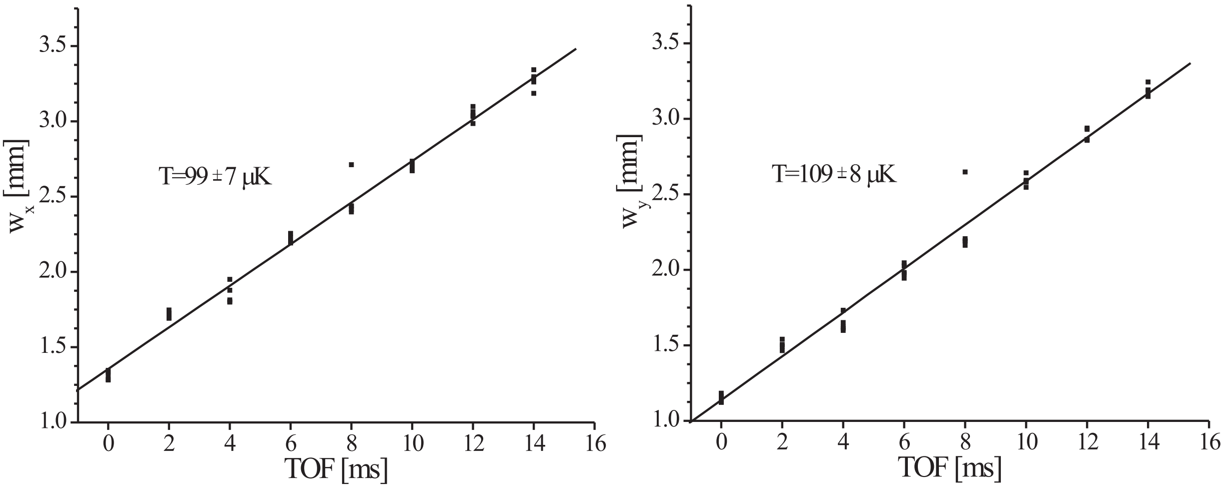

Figure 3.6: Temperature measurement by TOF (time of flight). The widths in horizontal (x) and in vertical (y) direction are plotted versus the time of flight. For each time, five measurements have been performed in order to demonstrate the reliability of the method. The temperatures calculated from the expansion velocity are given in the plots.

due to the kinetic energy of the freed atoms. The temperature can then be deduced from the expansion velocity.

The connection between the cloud expansion velocity v_{exp} and the temperature is very simple for an ideal classical gas. A gas at a given temperature T expands isotropically for expansion times long enough such that the expanded cloud is large compared to its initial size. The mean velocity v_{exp} of the expansion is given by

$$v_{\text{exp}} = \sqrt{\frac{2k_{\text{B}}T}{m}}. \tag{3.10}$$

This velocity is obtained experimentally via the evaluation of a series of pictures taken after defined expansion times. For each picture the width of the cloud is determined by fitting an appropriate function onto the data. In the case of a classical gas the cloud is described very well by a Boltzmann statistics and its density can be fitted with a Gaussian function. Indeed, a Boltzmann distribution can be assumed down to very low temperatures, as was apparent from the energy distributions of a Bose gas in a harmonic trap 2.1.

In figure 3.6 typical data obtained for a temperature measurement is displayed. As the cloud expands vertically and horizontally, two orthogonal widths can be measured and a horizontal expansion as well as a vertical expansion velocity can be deduced. For a consistent measurement, the temperatures derived from these velocities should be equal within their error bars.

To illustrate the reliability of the method, five measurements have been carried out for all expansion times. Many points are so close together, that they overlap. The remaining differences between the measurements stem most likely from differences in the preparation of the clouds, induced by imperfections and drifts within the experiment.

During an experimental run, the evaluation of a series of TOF images is automated by specialized software. Computer time intensive tasks as e. g. fitting a two dimensional Gaussian onto the data, is performed by compiled C programs. The executables are called by a TCL[1] script, that also provides a graphical user interface, plots the data and calculates the temperature and related information. This software combination enables to perform a quantitative analysis and to take data simultaneously.

An important point to note is that only the shape of the cloud is important for the determination of the temperature. The strength of the absorption signal is only important in the sense that the absorption must be high enough in order to grant an acceptable signal to noise ratio. In contrast, measurements of the atom number rely heavily on the number of scattered photons, making them susceptible to very different systematic uncertainties.

3.2.4 Atom number measurements

The measurement of the atom number can be performed with three different techniques. These methods are described and compared below.

Fluorescence measurements of the atom number

The basic idea behind a fluorescence measurement is the fact that the number of detected photons is proportional to the number of emitting atoms.

Fluorescence measurements are used within our experiment when the atoms are trapped in a magneto-optical trap. As part of the trapping mechanism, the atoms are stored in a light field detuned only a few linewidths Γ from the closed transition $5S_{1/2}\ F = 2 \rightarrow 5P_{3/2}\ F' = 3$ (cf. figure 3.11 in the next section). As will be discussed below, neither the light field distribution nor the m_F distribution of the atoms are well known. However, it has been shown, that the rough approximation of assuming isotropically polarized light impinging on atoms with evenly distributed m_F population leads to reliable results [73].

With these assumptions one defines an effective saturation intensity $I_{\text{sat,eff}}$ by averaging equations (3.2) and (3.4) over all polarizations and m_F-values. This yields together with the knowledge of the reduced matrix element the value $I_{\text{sat,eff}} = 3.57\,\text{mW/cm}^2$. Comparing the detected light power P with the expected photon stream into the solid angle $\Delta\Omega$ covered by the detectors, one obtains for the atom number

$$N = \frac{4\pi}{\Delta\Omega}\frac{P}{\hbar\omega\gamma}. \tag{3.11}$$

The expression depends on the saturation intensity $I_{\text{sat,eff}}$ via the photon scattering rate γ. Example applications of this technique are discussed in section 3.3, since this technique is used extensively to monitor the atom number and loading behavior of our MOTs.

Fluorescence measurements offer in principle the advantage of measuring against a small background. This is the main reason this technique has been used very successfully to monitor the atom number on a single atom level [74] and even for imaging single atoms [75]. However, to obtain a signal to noise ratio comparable to the one reached with absorption imaging requires experimental parameters (long integration times, collecting photons from a large solid angle) which are not easy to realize within our experiment.

---

[1] TCL is a scripting language in the public domain available from `www.tcl.tk`. It runs on several platforms and provides as well a GUI toolkit as special functions to facilitate control of external programs.

Absorption measurements of the atom number

For each processed absorption image one retrieves the atomic absorption $D(x, y)$, which is proportional to the column density $n_c(x, y)$ according to equation (3.7). For a known cross section σ, the atom number can then be determined by integrating over the reconstructed $n_c(x, y) = D(x, y)/\sigma$. Since $D(x, y)$ is recorded on a CCD chip with finite pixel size, the integral has to be replaced by a finite sum over the exposed pixels. Thus the atom number is extracted by

$$N_{\text{atoms}} = \sum_{\text{all pixels } (i,j)} AD(x_i, y_i)/\sigma, \tag{3.12}$$

where A is the area of one pixel of the CCD chip. The formula assumes a magnification factor of 1.

In principle, absorption imaging suffers from the same systematic uncertainties as fluorescence imaging regarding a quantitative examination, since a determination of σ is equivalent to a determination of γ. It turns out, however, that atom numbers determined by absorption measurements in our experiment are more robust with respect to experimental imperfections than those obtained by fluorescence measurements. Absorption imaging is usually carried out in the range $s \ll 1$, i. e. the absorption rate is basically proportional to the intensity I (cf. equation (3.1)). Since the profile of the imaging beam is proportional to I within this linear ansatz, the value of I does not enter the imaging processing. This eliminates uncertainties due to saturation effects and absolute power calibration from the analysis.

Furthermore, absorption measurements usually have a much better signal to noise ratio compared with fluorescence measurements in our experiment. There are two main reasons for this. First, because of the application of resonant light, the effect of one atom is stronger than for detuned light. Second, the complete signal due to absorption is delivered within a small solid angle to the detector, namely within the dimensions of the imaging beam. In contrast, fluorescence is distributed over the whole solid angle, of which in our setup only a small fraction (less than one percent) can be captured with imaging optics.

Atom number measurement via optical pumping

A third method for measuring the atom number of a cloud can be implemented using an optical pumping technique [76, 77]. For absorption measurements the atoms are probed on a cycling transition, where the atoms fall back from the excited state into the same ground state. In contrast to that, this method relies on the excitation of the atoms on an open transition. The atoms are excited resonantly to the transition $5S_{1/2}$ $F = 2 \rightarrow 5P_{3/2}$ $F' = 2$. According to the selection rules for dipole transitions, atoms excited to $F' = 2$ can

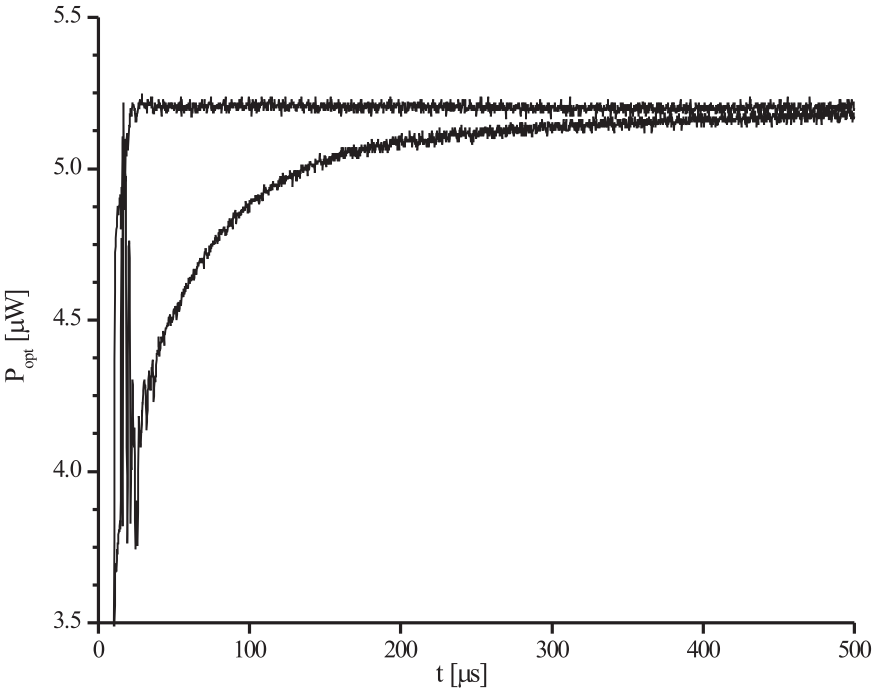

Figure 3.7: Measurement of the atom number via optical pumping. The upper curve is the photo diode signal without atoms present, the lower with atoms. The fast modulations at the beginning of the atomic signals probably stem from frequency noise of the laser due to acoustic distortions (e. g. from mechanical shutters). The atom number extracted from this particular measurement is $1.8 \cdot 10^8$.

fall back spontaneously either into the $F = 2$ or into the $F = 1$ ground state by reemitting the photon. The branching ratio between these possibilities is 1:1 for intensities well below the saturation intensity [51]. Thus on average after two absorption–emission cycles the atom is in the $F = 1$ state and can not be excited any more. In the weak intensity limit, this constitutes an optical pumping process whose time constant depends linearly on the incident light intensity.

In figure 3.7 the transmission of the probe beam is recorded for a light pulse switched on by an AOM in less than 1 μs by a fast, sensitive and power-calibrated photo diode. If no atoms are present, the recorded signal is the expected step function. If an atomic cloud is present, the light is first attenuated and the signal reaches asymptotically the light level as measured without atoms. The fast modulation of the absorption signal at the start of the measurement is due to a fast frequency jitter of the laser caused by mechanical vibrations which are created by the fast shutters.

After the light has interacted with the atoms, it passes eight glass surfaces before reaching the detector. This leads to an attenuation of the signal, that has to be taken into account. A loss of about 15% can be deduced from measurements, which is also consistent with the properties of the involved surfaces and elements. Thus in order to correct for this loss, all measured signals at the place of the photo diode have to be multiplied with a factor of

1.18.

For low intensities and on resonance, the photon scattering rate as given in equation (3.1) is linearly dependant on $I/I_{\mathrm{sat,eff}}$. Since two photons are needed on average to transfer the atom into the $F = 1$ state, the optical pumping time can be estimated as

$$\tau_{\mathrm{pump}} = 2/\gamma = \frac{1}{\Gamma}\frac{I_{\mathrm{sat,eff}}}{I}. \tag{3.13}$$

Assuming an initially uniform distribution of the atomic population among all m_F leads to a calculated saturation intensity $I_{\mathrm{sat,eff}} = 7.7\mathrm{mW/cm}^2$ for the $F = 2 \to F' = 2$ transition according to equations (3.2) and (3.4). However, since the atoms are optically pumped before decaying to the dark state $F = 1$, the m_F-distribution and therefore also the effective saturation intensity will change. Ignoring this for a rough estimate and inserting the used light power of $P \approx 1.18 \cdot 5.2\ \mu\mathrm{W} = 6.1\ \mu\mathrm{W}$ and a cross section area of the probe beam of $A \approx 0.5\ \mathrm{cm}^2$, an optical pumping time $\tau_{\mathrm{pump}} \approx 39\ \mu\mathrm{s}$ can be expected. This is consistent with the measured pumping time of $\tau_{\mathrm{pump}} = 65\ \mu\mathrm{s} \pm 3\ \mu\mathrm{s}$ in figure 3.7 within a factor of 2. Since the distribution of the m_F states will evolve towards the outermost state $m_F = 2$, leading to greater saturation intensities I_{sat}, this discrepancy can possibly be explained by this optical pumping effect. However, the agreement is good enough to conclude that the behavior of the atoms can be explained with the simple model given above.

The main importance of this method lies in the fact that the atom number can be inferred from the integrated absorption signal alone. Since it takes on average two photons to pump one atom into a dark state, each atom consumes an energy of $2\hbar\omega$ from the light beam, ω being the resonance frequency. The total energy taken out of the light beam by the atoms can be experimentally determined by integrating the difference between the recorded power with and without atoms present. This value must equal $2N\hbar\omega$ (N is again the atom number):

$$N = \frac{\int dt\, P_{\text{without atoms}}(t) - P_{\text{with atoms}}(t)}{2\hbar\omega} \tag{3.14}$$

External factors like detunings, the distribution of the population over specific m_F states or intensities can only change the time constant of the optical pumping process or, more generally, the shape of the recorded curve, but not the integral appearing in equation (3.14). This makes the scheme very robust against experimental imperfections.

The main application of this method within our experiment is to verify the reliability of the other two methods. Such a comparison between the fluorescence measurement and the optical pumping technique is shown in figure 3.8. Since these two methods can be compared by measuring the *same* cloud, errors in evaluating the results due to different preparation of the atomic ensembles can be avoided.

Figure 3.8 shows the number of atoms obtained with the fluorescence technique versus the number obtained with the optical pumping method. For perfect coincidence the points should lie on one line. On average, the fluorescence method yielded slightly higher values. This is probably due to a not perfectly isotropic m_F distribution of the atoms, which

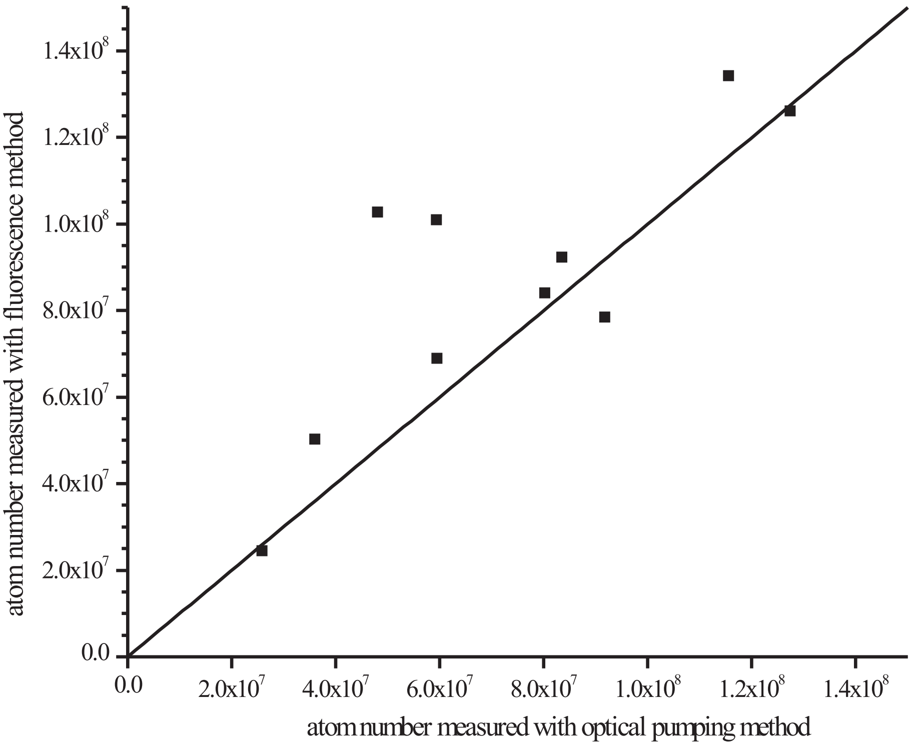

Figure 3.8: Comparison of optical pumping and fluorescence method for the atom number determination. Atomic clouds have been measured simultaneously with both methods. For perfect coincidence the data must be on the black line.

can influence the results of the fluorescence measurement. Still the coincidence is very good for most data points, but occasional outliers occur (e. g. between $4 \cdot 10^7$ and $6 \cdot 10^7$ atoms). Taking this outliers into account, the relative rms difference is 18%. This value characterizes the precision with which we can determine the atom number in our experiment. This level of precision is comparable if not better than other published results from similar experiments (cf. e. g. [76]).

3.2.5 Limits for the detection of small particle numbers

The imaging system at the experiment is very well suited to extract data from atomic clouds with many atoms. For obtaining equally good data in the case of few particle systems however, the remaining noise sources within the system must be identified and minimized. In the remaining part of this section I therefore model the signal to noise ratio attainable with the setup and compare it to the status quo.

As already pointed out in section 3.2.1, equations (3.5) and (3.6), it is necessary to record the three images I_A (picture with atoms), I_B (picture without atoms) and I_D (picture without operating lasers, yielding the noise term $N(x, y)$), for optimal results in the case of low signals. I neglect here noise contributions which can arise due to multiply scattered light from the optics reaching the detector.

The influence of the dark noise terms can be eliminated by subtracting I_D from the other pictures. Since the term $N(x,y)$ fluctuates, these subtractions are not error-free and contribute to the overall noise budget. Also the profile of the probe beam fluctuates and thus gives rise to errors. For practical purposes slight pointing instabilities of the imaging will dominate the fluctuations in the profile $P(x,y)$, because the interference pattern on the chip will change slightly. This in turn will induce differential fringes in the final image due to the image processing. The effect can be minimized by choosing short free beam paths, fixing the whole setup rigidly onto one common base and using only short time intervals between taking the two pictures I_A and I_B. We have learned from other groups, that the fluctuations of our probe beam profile concerning shot to shot comparisons is already fairly small [78].

After the discussed steps one arrives thus at corrected pictures $\tilde{I}_A$ and $\tilde{I}_B$ defined by

$$\begin{aligned} \tilde{I}_A(x,y) &= I_A(x,y) - I_D(x,y) = P(x,y)e^{-D(x,y)} && (3.15) \\ \tilde{I}_B(x,y) &= I_B(x,y) - I_D(x,y) = P(x,y). && (3.16) \end{aligned}$$

The analysis can then proceed just as discussed above with these corrected images and extract the column density $n_c(x,y)$ from $D(x,y)$. The obtained signal $n_c(x,y)$ has to be compared with the noise level accumulated through the image processing and the initial noise in the raw data.

For the purpose of determining the ultimate attainable signal to noise ratio, I restrict myself to shot noise contributions and assume the following noise levels for the relevant terms $P(x,y)$ and $N(x,y)$:

$$\begin{aligned} \Delta P(x,y) &= \sqrt{P(x,y)} && (3.17) \\ \Delta N(x,y) &= \sqrt{N(x,y)}. && (3.18) \end{aligned}$$

I neglect in the following fluctuations due to the Poissonian distribution of photon scattering events, which would result in uncertainties in the cross section σ connecting the column density n_c and the optical density D. For the exposure times used in our experiments this factor becomes relevant only for single particles.

Applying the Gaussian law of error propagation, the expected noise on the retrieved signal for the column density is given by

$$\Delta n_c(x,y) = \frac{e^{\sigma n_c(x,y)}}{\sigma P(x,y)} \sqrt{2e^{-2\sigma n_c(x,y)} \left(N(x,y) + P(x,y)\right) + 2N(x,y)}. \qquad (3.19)$$

A signal to noise ratio of 1 is reached if $\Delta n(x,y) = n(x,y)$. For a homogenous cloud and for the numbers quoted above ($P \approx 10000$ counts, dark current of the camera $N \approx 5$ counts), this condition is reached at a column density of about $7.3 \cdot 10^6$ particles/cm^2.

In the case of trapped atomic clouds the density is not a homogeneous function but peaked in the center of the trap. For the parameters of a parabolic trap with trap frequencies of $\omega_z = 2\pi \cdot 21.5\ \mathrm{s}^{-1}$ and $\omega_\rho = 2\pi \cdot 271.6\ \mathrm{s}^{-1}$ (as realized within our experiment), I calculate

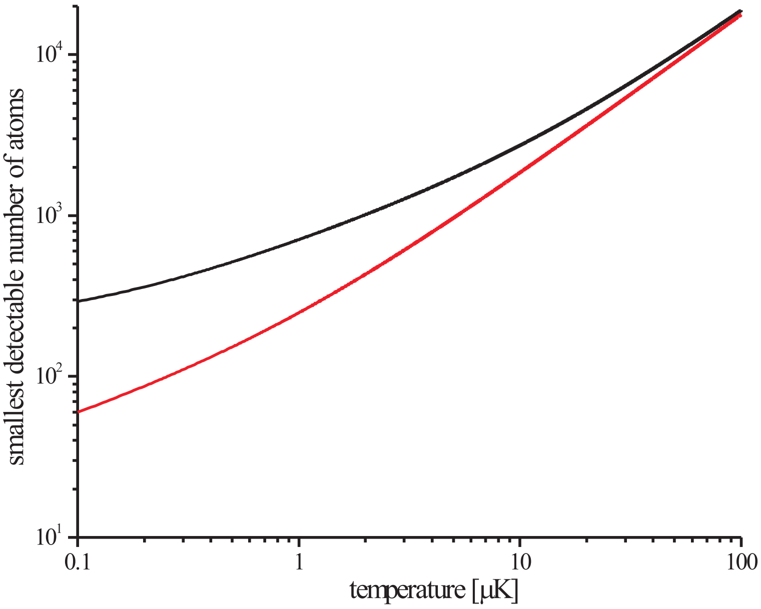

Figure 3.9: Smallest detectable number of atoms by absorption measurement versus temperature. The upper black curve shows the number of atoms required to reach a signal to noise ratio of 1:1 in the peak of the density distribution, given a point spread function width of the system of 34 μm. The lower red curve corresponds to the case of a point spread function width of 8 μm.

the atom number, for which the above condition is fulfilled at a given temperature. The resulting plot is shown in figure 3.9. At lower temperatures and constant atom numbers, the density in the center increases and thus a smaller number of atoms can be detected. For very low temperatures the resolution of the imaging system becomes one limiting factor. In the plot two curves are displayed, corresponding to the resolution of the system as it was measured and to the resolution which can be expected according to the calculation in section 3.2.

Note, that we have required the signal to noise ratio being equal to 1 in order to call an atom number detectable. This definition is reasonable, but still somewhat arbitrary. By averaging over some carefully chosen area within the picture, or by taking several images for averaging, it might still be possible to recover meaningful information even with less atoms present.

A typical number to characterize the current imaging system is a measured signal to noise ratio of 4.9 at a peak column density of approximately $2.4 \cdot 10^7/\mathrm{cm}^2$, which is comparable to the theoretically attainable ratio as outlined above.

3.3 Magneto-optical traps as the precooling stage

Laser cooling in magneto-optical traps serves as the first cooling stage in the experiment. Since their first realization in 1987 [79], magneto-optical traps have become the most widely used tool for experiments performed with cold and ultracold gases. Standard magneto-optical traps cool within seconds about 10^8 atoms from an initial temperature of 300 K by more than six orders of magnitude down to 100 μK. From a technical perspective, the hardware requirements are such that simple MOT systems have been proposed (and realized) even for undergraduate lab classes [80]. On the other hand, for more elaborate and advanced systems, the technical requirements soon become more difficult to fulfill. Indeed, in our experiment most of the installed technical equipment is more or less directly devoted to a reliable and effective operation of the two implemented MOTs.

3.3.1 Working principles and limits

General setup and Doppler cooling

An intuitive understanding of a MOT can be gained in terms of light pressure acting on the trapped atoms. Let us first examine a simplified, one dimensional picture, as displayed in the left half of figure 3.10. Shown is the interaction of two near resonant and counterpropagating laser beams of equal intensity with an atom. The laser frequency is chosen a few natural linewidths below the atomic resonance (a so called *red detuning* of the lasers). For an atom at rest, the interaction with each beam will be of equal strength. However, in the rest frame of a moving atom, the frequency of the beam opposite to its direction of movement will be closer to resonance than the frequency of the other beam, due to the Doppler effect.

Thus the atom will scatter more photons from the counterpropagating beam than from the copropagating beam. Each absorbed photon transfers a momemtum $\hbar k$ along the propagation direction of the corresponding laser beam. For spontaneous emission processes, the photons emitted from the atom are distributed over the complete solid angle. Thus the recoil momenta acquired by an atom vanish on average for many scattered photons. Therefore the effects of the emission processes can be neglected at first for a conceptual understanding of the MOT.

The force exerted onto the atom can be estimated in quantitative form by simple arguments. Averaging over times larger than one emission–absorption cycle, one can approximate the stochastic kicks experienced by the atoms by a continuous force. Using $F = \frac{d}{dt}p$ and the photon scattering rate γ introduced in equation (3.1), the force on an atom with velocity v between the two laser beams as shown in figure 3.10 is given by

$$F = \hbar k \left(\gamma_{\text{beam1}}\left(\Delta = \Delta_{\text{laser}} + kv\right) - \gamma_{\text{beam2}}\left(\Delta = \Delta_{\text{laser}} - kv\right)\right) \tag{3.20}$$

Here Δ_{laser} is the detuning of the laser beams in the laboratory frame. The resulting force is plotted in the right half of figure 3.10. The forces of each individual beam in dependance of the atomic velocity v and the resulting total force are shown. For small velocities v, the resulting force F_{om} can be approximated by a Taylor expansion of equation (3.20) around $v = 0$. This expansion yields in first order a linear dependance on v given by [81]

$$F_{\text{om}} = \frac{8\hbar k^2 s \Delta_{\text{laser}}}{\Gamma\left(1 + s + \left(2\Delta_{\text{laser}}/\Gamma\right)^2\right)^2}\, v, \tag{3.21}$$

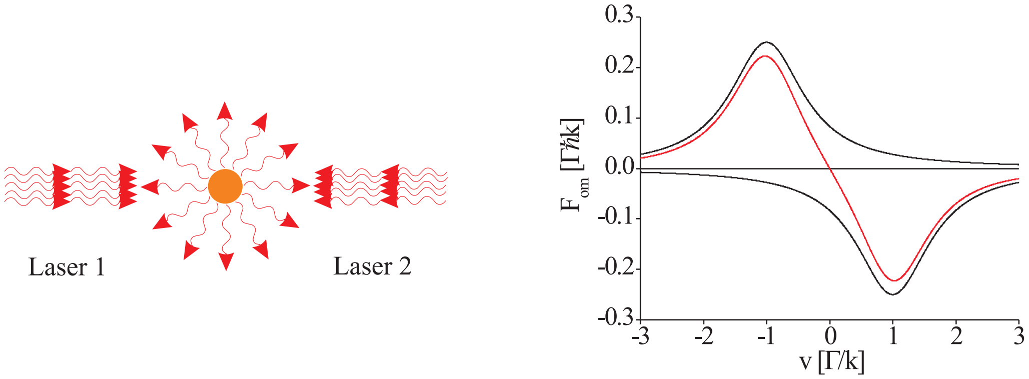

Figure 3.10: One dimensional optical molasses. Left image: An atom between two red detuned laser beams of equal intensity. Right image: Dependance of the light pressure force F_{om} on the atomic velocity. The forces due to the individual beams are shown in black, the resulting force in red color. The plot describes the force for $\Delta_{\mathrm{laser}} = \Gamma$ and $s = 1$, according to equation (3.20).

where $s = I/I_{\mathrm{sat}}$ is again the saturation parameter. Since $\Delta_{\mathrm{laser}} < 0$ (red detuning), the force acts like a friction force damping the motion of the atom. In analogy to a particle being damped in a viscous liquid, this arrangement has been named *optical molasses*. In order to have a significant force acting on a large range of velocities, typical parameters are $s = 1$ (i. e. $I = I_{\mathrm{sat}}$) and $\Delta_{\mathrm{laser}} \approx \Gamma$. These are also the parameters used in the plot 3.10.

Because the momentum transfer due to one photon is very small, the scheme relies on a high scattering rate. This is usually realized by employing the scheme close to resonance of a closed transition. For Alkali atoms, having a $S_{1/2}$ ground state with two hyperfine states, the common choice is to work close to the transition from the higher hyperfine ground state F to the $F' = F + 1$ state of the $P_{3/2}$ manifold (D_2 line). In the case of ^{87}Rb, this is the transition from $5S_{1/2}F = 2$ to $5P_{3/2}F' = 3$ (see the term scheme in figure 3.11). According to the dipole transition selection rules, an atom excited to $F' = 3$ can only decay into the $F = 2$ ground state and will be immediately reexcited by the same laser source. However, due to off resonant excitation, on average after a few thousand absorption–emission cycles an atom is excited into the $F' = 2$ state. From here it can decay into the $F = 1$ ground state. In this state the atom is not in near resonance with the laser field and experiences no light force. In order to reinsert the atom into the cooling cycle, an additional laser resonant to the $F = 1 \rightarrow F' = 2$ transition is shone onto the atoms. Since an atom in the $F' = 2$ state decays with 50% probability into the $F = 2$ ground state, this laser (which is called *repumping laser*) optically pumps atoms very efficiently back into the cooling cycle.

The cooling scheme presented so far is called *Doppler cooling* and the lowest temperature to be expected theoretically is called *Doppler temperature*. The magnitude of this temperature can be estimated by taking into account the emission processes neglected so far.

As stated above, the recoil momenta accumulated by an atom in the optical molasses

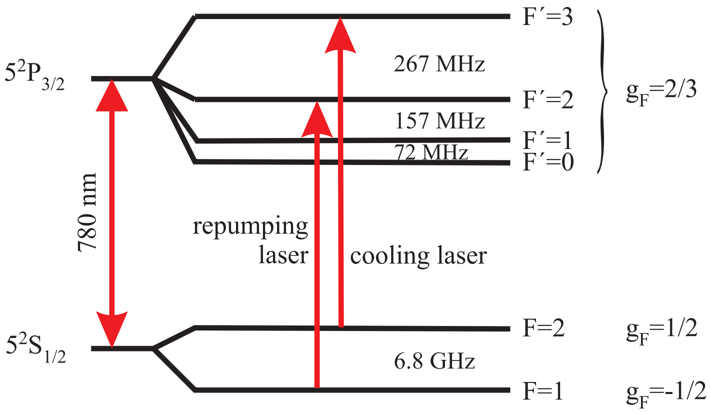

Figure 3.11: Level scheme of ^{87}Rb. The cooling transition and the repumper transition as used in the MOT are marked in red color. Note, that the energy scale indicated by the hyperfine splittings and the optical frequency are not to scale.

average to zero. But the rms momemtum of the atom is finite, as can be visualized by noting that the atom performs a random walk in momentum space. This rms momentum gained by the atom corresponds to a heating process, since the atom gains kinetic energy. Within the Doppler cooling model, the steady-state temperature is reached if this heating rate is equal to the cooling rate due to the damping force of equation (3.21). This condition leads the the expression for the Doppler temperature T_D [81]

$$k_B T_D = \frac{1}{2}\hbar\Gamma. \tag{3.22}$$

For Rubidium atoms one recovers $T_D = 141\ \mu\text{K}$ [51].

The optical molasses scheme as discussed so far is a very efficient way of cooling atoms, but it does not provide a restoring force and is thus not suitable for trapping atoms. This is achieved by adding an inhomogeneous magnetic field to the setup and choosing carefully the polarizations of the laser beams.

The underlying idea is exemplified in the left half of figure 3.12, within a one dimensional simplified scheme. Consider a $J = 0 \rightarrow J' = 1$ transition, such that there is only one $m_J = 0$ state in the ground state and $m_{J'} = -1$, $m_{J'} = 0$ and $m_{J'} = +1$ substates in the excited state. Applying an inhomogenous magnetic field with constant gradient lifts the degeneracy of the three excited states due to the Zeeman effect and introduces thereby different resonance frequencies. As for an optical molasses the laser frequency is red detuned, which means in this case that the laser frequency is below the transition of an atom at rest for an transition without magnetic field.

Moving to the right from $B_z = 0$, the resonance frequency for the $m_J = 0 \rightarrow m_{J'} = -1$ transition approaches the frequency of the laser light, while the resonance frequency for the transition $m_J = 0 \rightarrow m_{J'} = +1$ is detuned even further. A restoring force is established by preparing the incident laser beams in such a way that the laser beam directed from right to left interacts much stronger with the atom than the opposite pointing laser beam,

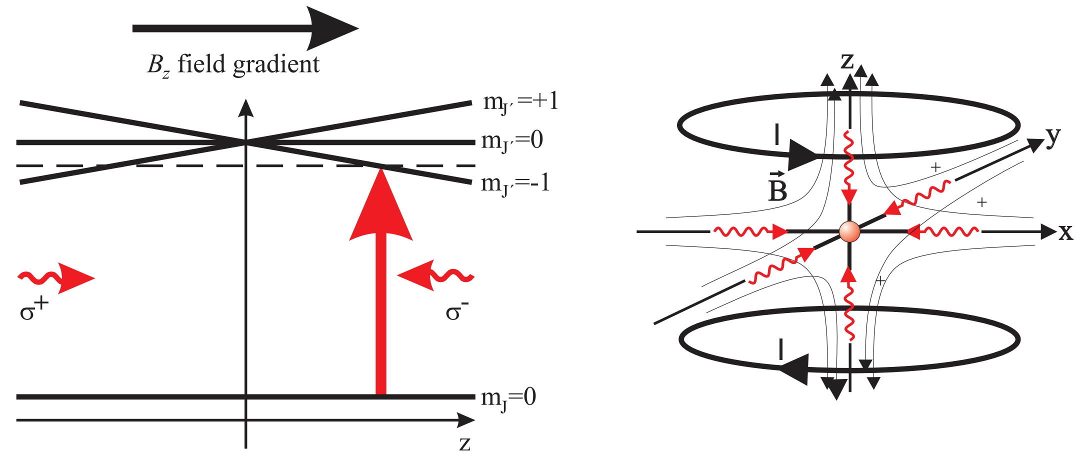

Figure 3.12: Working principle of a MOT. Left image: A simplified one dimensional model to visualize the restoring force obtained by superimposing a magnetic field $B_z = \zeta_z z$. Right image: Three dimensional realization of the MOT. For details see the text.

although both beams carry light of the same frequency. This is achieved by choosing different polarizations for the beams. In this case the beam coming from the right side has a σ^- polarization, while the opposite beam is σ^+ polarized. Due to the m_J selection rules, the beam from the right can only excite the transition $m_{J'} = 0 \rightarrow m_{J'} = -1$ and the opposite laser the transition $m_J = 0 \rightarrow m_{J'} = +1$.

The same argument holds with reversed signs for an atom displaced from the center to the left. The restoring force F_{rest} can thus be written as

$$F_{\text{rest}}(z) = \hbar k \left(\gamma_{\text{beam1}}\left(\Delta = \Delta_{\text{laser}} + \mu B(z)\right) - \gamma_{\text{beam2}}\left(\Delta = \Delta_{\text{laser}} - \mu B(z)\right)\right), \tag{3.23}$$

where μ is the magnetic moment of the atom. A linear expansion gives for a magnetic field $B_z(z) = \zeta_z z$ the expression [81]

$$F_{\text{rest}} = \frac{8\mu\zeta_z s \Delta_{\text{laser}}}{\Gamma\left(1 + s + (2\Delta_{\text{laser}}/\Gamma)^2\right)^2} kz. \tag{3.24}$$

Because of the formal similarity to the friction force F_{om}, the dependance of the restoring force on the coordinate z is just a differently scaled version of the graph displayed for the damping force in figure 3.10.

So far the discussion has been limited to an atom with a $J = 0 \rightarrow J' = 1$ transition. The basic arguments given remain also valid for atoms with more m_J levels in the ground and excited state. However, in this case additional effects arise due to optical pumping phenomena.

Cooling beyond the Doppler temperature

It was first found experimentally that the temperatures in optical molasses were below the expected Doppler limit [82]. Shortly after, the explanation was found in a complex

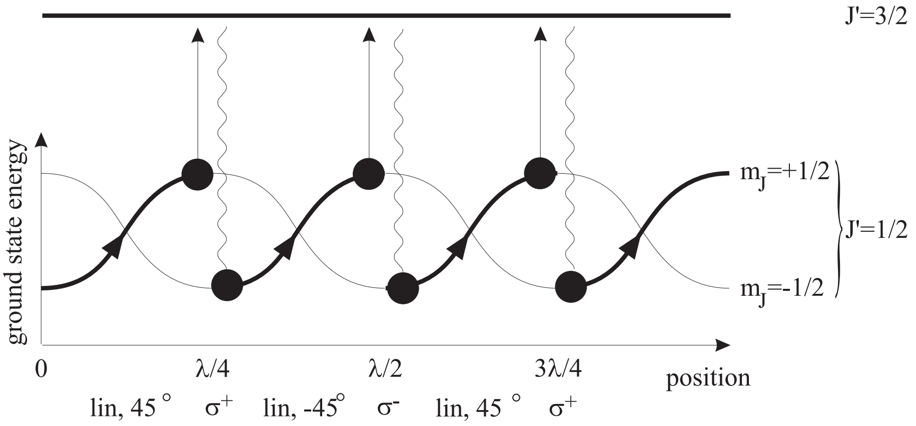

Figure 3.13: Sisyphus cooling. The kinetic energy of an atom travelling through an optical molasses is dissipated due to the Sisyphus cooling mechanism. For details see the text.

interplay of optical pumping effects, position dependant shifts of the atomic ground state energies and the dynamics due to the atomic motion [83, 84]. An essential ingredient is the multilevel structure of the atoms.

Because of the complicated light structure of six interfering light beams, the complete situation in a three dimensional optical molasses or MOT can only be assessed by numerical simulations [85, 86]. However, the overall idea of one of the most prominent mechanisms, which is known as *Sysiphus cooling*, can be explained for a one dimensional molasses acting on an atom on a $J = 1/2 \rightarrow J' = 3/2$ transition.

Near resonant light not only excites atoms to an excited state, but also induces shifts of the ground state level. These shifts, commonly referred to as *light shifts*, arise due to an AC Stark effect in second order perturbation theory. For near resonant light fields, the shift of a m_J ground state is given by [83]

$$\Delta E_g = \frac{1}{2}\frac{\hbar\Delta s}{1+(2\Delta/\Gamma)^2}\begin{pmatrix} J' & 1 & J \\ -m'_J & q & m_J \end{pmatrix}^2 \tag{3.25}$$

The three J symbol describes the dependance of the shift on the m_J quantum number and the polarization q of the incident light. As a rule, the shifts due to the outermost transitions are strongest. Thus an atom in the $m_J = +1/2$ state experiences a stronger light shift if exposed to σ^+ polarized light than in σ^- light. As discussed, the light fields are all red detuned, thus the detuning Δ is negative and the ground state energy is always reduced.

An instructive situation is shown in figure 3.13, where the polarization of the counter-propagating laser beams is chosen linear and orthogonal to each other. The total intensity of the resulting interference pattern is everywhere constant, but the polarization of the resulting standing light field changes rapidly within half an optical wave length. Starting with a 45° tilted linear polarization, it evolves over a σ^+ state, $-45°$ tilted linear state and a σ^- state back to the 45° tilted linear polarization state. Thus the ground state energy of an atom moving slowly through the light field is periodically modulated due to the changing strength of the light shift. Since also the excitation rates from the specific ground state to different excited states depend on the local polarization of the impinging light, the atom is optically pumped and changes accordingly its ground state population during its motion through the light.

The interplay between optical pumping and motion is synchronized here in such a way, that the atom is preferably pumped to the state with less ground state energy, when it has just reached a region with a high ground state energy. So the atom climbs a potential well given by the light shifts, just to be pumped into another state, which experiences a potential "valley" at the very same position. The difference in energy is taken away by the spontaneously emitted photons during the optical pumping process and causes a reduction of the kinetic energy. Because of the changes in the light polarization, the resulting cooling scheme is often referred to as *polarization gradient cooling*.

The resulting friction force can be much larger than the one induced by the Doppler cooling scheme, resulting in lower temperatures. However, this cooling mechanism only works within a much narrower velocity range [83].

The cooling process stops, as soon as the atoms do not have enough energy to climb the next light shift potential barrier. Thus the lowest temperatures which can be reached with this method are determined by the detuning and intensity of the beams, since a larger detuning and less intensity mean a lower light shift barrier [82]. Optical molasses exploiting this cooling scheme are commonly further detuned from the resonance than lasers operated for a MOT. It has been shown, that a magnetic field applied during this cooling process leads to higher temperatures than a pure optical molasses [87].

Phase space compression and limits of near resonant cooling

From the above discussion it is clear, that the MOT does not provide a conservative potential and is based on mainly dissipative forces. Owing to this an atomic ensemble can be both compressed spatially and cooled at the same time, i. e. the MOT can increase the phase space density of an atomic ensemble. This is not possible in conservative traps due to Liouville's theorem [81]. The limit for the obtainable maximum density is not evident. It turns out, that there are two limiting processes.

First, an increased density, i. e. a higher optical thickness of the sample at the center of the trap leads to the mechanism of *radiation trapping* [88]. At some point, fluorescence light emitted from atoms inside the cloud is not able to leave directly but is reabsorbed by other atoms of the cloud. Due to the recoil momenta of the absorption processes, the atoms feel effectively an repulsive force, which counteracts further spatial confinement of the cloud.

An increased density leads also to an additional loss mechanism. Although the MOT is not a conservative trap, one can assign an effective trap depth by estimating the minimal velocity necessary to escape from the finite trap region. Atoms can gain enough kinetic energy to escape from the trap by inelastic collisions among the atoms. The probability of collisions — and thus also of inelastic collisions — scales quadratically with the density n. The resulting loss processes limit the attainable density within the MOT.

It should be noted, that this density limiting effect is much stronger in the presence of near resonant light (as in the MOT) than in traps avoiding the excitation of the atoms. The cross section for collisions involving one excited atom is larger than the cross section for a collision of two ground state atoms. This leads to a higher overall collision rate [81].

As shown below, there is experimental evidence that the MOTs realized in our experiment are influenced by both processes. One obvious solution to overcome these limits is the use of a trap without resonant excitation of the atoms.

Although traps relying on near resonant light can not provide a complete solution for the technical problems in achieving BEC, it is still instructive to compare typical figures obtainable with the MOT as compared to the background vapor. In a typical experimental setup, the atomic partial pressure may be 10^{-9} mbar, yielding a particle density of about 10^7 cm^{-3} at a temperature of 300 K. Typical figures for an optimized MOT are a density of 10^{11} cm^{-3} and a temperature of 50 μK. This leads to a phase space density on the order of 10^{-20} for the vacuum and 10^{-6} for the MOT. Although these figures vary slightly depending on the particular implementation of the MOT and the settings of the vacuum system, they illustrate the great impact of these traps for achieving quantum degeneracy requiring a phase space density of unity. Owing to these numbers, a MOT can also be viewed as a very effective "phase space compressor".

3.3.2 The reservoir MOT as a cold atom source

In our experiment this first and largest enhancement of the phase space density takes place in a MOT in the upper vacuum cell (cf. figure 3.1 for the overall experimental setup). The atoms captured by this MOT are low velocity atoms from the background vapor. The partial Rb background pressure is about 10^{-9} mbar [63]. A more detailed view is given in figure 3.14. The MOT consists of three retro-reflected beams of laser light. The width of the beams is limited to 2 cm by the apertures of the vacuum windows. Typically, about 30 mW of cooling laser power is present in each beam. The light is 15 MHz (≈ 2.5 natural linewidths) detuned below the resonance $5S_{1/2}F = 2 \rightarrow 5P_{3/2}F = 3$.

The repumper beam has a power of 3 mW. It is superimposed onto the cooling laser beam which runs vertical to the breadboard shown in figure 3.14.

The magnetic field is provided by two coils approximately in anti-Helmholtz configuration. They produce a quadrupole field with a gradient of about 12 Gauss/cm along the symmetry axis.

This MOT serves as a reservoir of cold atoms for the remaining experiment. The most important quantity for this MOT is the atom number it collects. Thus the trap is monitored by observing the fluorescence and deducing therefrom the atom number as described in section 3.2.4.

The signal obtained for this MOT is exemplified by the loading curve in figure 3.15. The shown signal is obtained by imaging the fluorescence onto a sensitive, calibrated

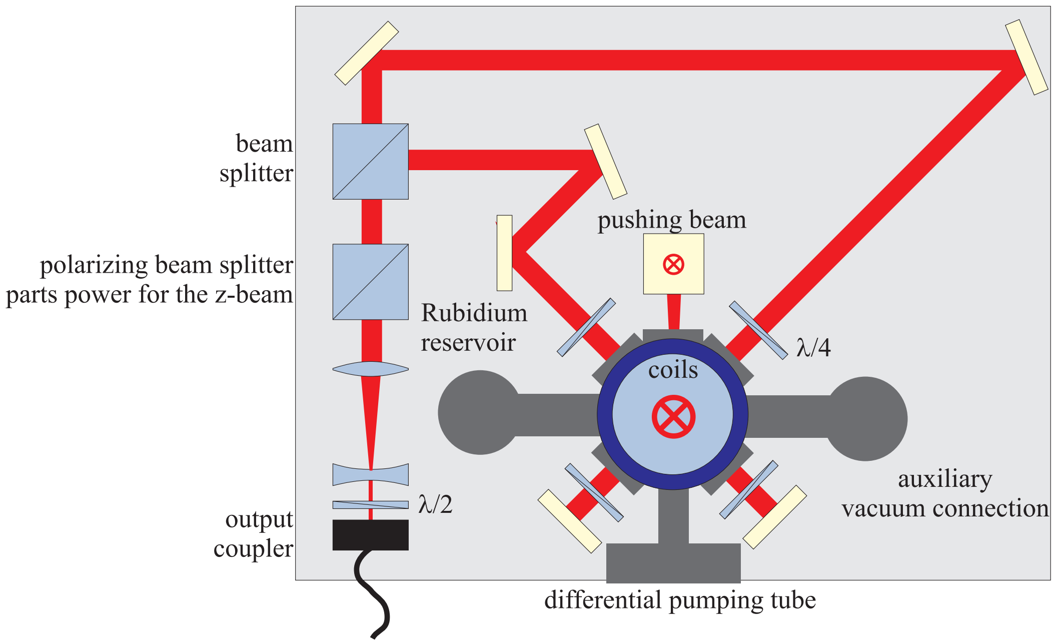
beam splitter
polarizing beam splitter parts power for the z-beam
output coupler
λ/2
Rubidium reservoir
pushing beam
λ/4
coils
auxiliary vacuum connection
differential pumping tube

Figure 3.14: Upper vapor pressure MOT. The main vacuum chamber is an octagon (CF 100 flange sized windows on the flat size and CF 40 flange sized windows on the small sides). Attached are the Rubidium reservoir and a pumping connection sealed with a valve. The optics is vertically mounted on a breadboard (50x38 cm). The breadboard has holes to pass the beam to its other side. Not shown are the optics for the third MOT beam and the repumper beam (which are on the backside of the breadboard) and most optics of the pushing beam.

photodiode. At the end of the curve, the MOT has collected so many atoms, that the resulting fluorescence is clearly visible to the bare eye, even in the presence of daylight.

The curve can be modelled by the rate equation

$$\dot{n}(t) = R - \alpha n(t) - \beta n(t)^2, \tag{3.26}$$

where $n(t)$ is the atomic density, R is the capture rate for collecting atoms from the background vapor and the terms $\alpha n(t)$ and $\beta n(t)^2$ describe losses due to collisions with hot atoms from the background and cold binary collisions, respectively.

Taking into account the boundary condition $n(t=0)=0$, equation (3.26) can be solved analytically, yielding

$$n(t) = \frac{\sqrt{\alpha^2+\gamma}\,\tanh\left(\frac{1}{2}\sqrt{\alpha^2+\gamma}\;t + \operatorname{arcosh}\left(\sqrt{\frac{\alpha^2+\gamma}{\gamma}}\right)\right) - \alpha}{2\beta}, \tag{3.27}$$

where $\gamma = 4\beta R$. A corresponding least square fit is shown in red color in figure 3.15. Neglecting losses due to binary collisions in the model leads to a pure exponentially decaying curve, which gives inferior results when fitted to the data.

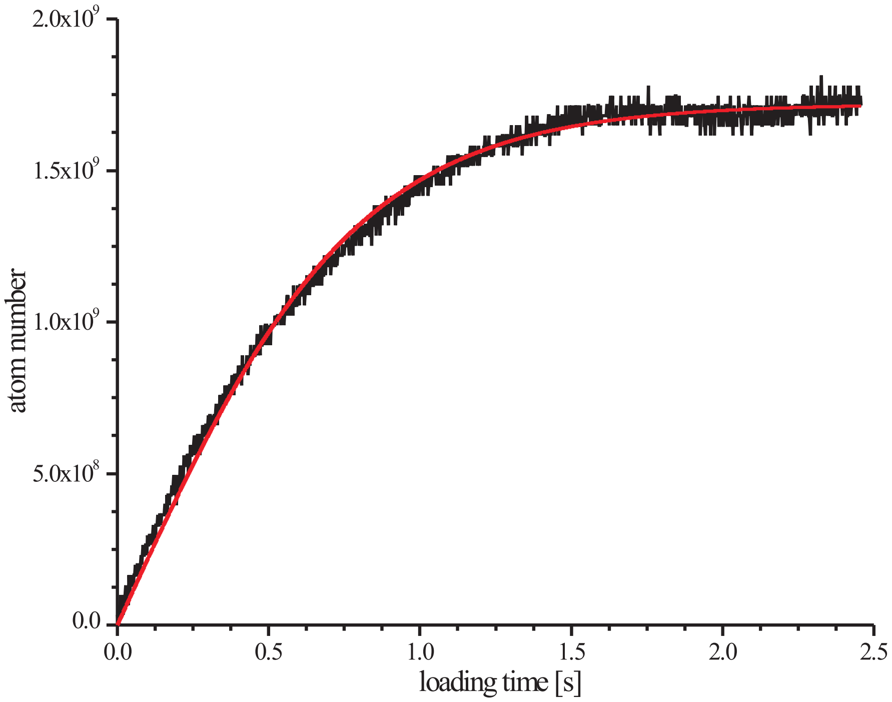

Figure 3.15: Loading curve of the reservoir MOT. The red curve is a fit based on the solution of an appropriate rate equation (see text). Small deviations of the fit from the data possibly occur, because the underlying model describes the density of the cloud while the measured signal is only proportional to the atom number.

During daily operation, the implemented reservoir MOT needed only occasional readjustments. The characteristics of the MOT — given same laser power and detuning — changed only slightly within weeks.

3.3.3 Atomic transfer beam and high vacuum MOT

Transfer to the second MOT

The vacuum in the upper vapor cell is not good enough to allow storage of the atoms for a sufficient long time in a magnetic trap. The atoms are thus transferred into another MOT by pushing them with a near resonant laser beam [89, 90]. In figure 3.16, the effect of this so called *pushing beam* on the first MOT is illustrated. One can clearly see a strong deformation of the atomic cloud.

However, this impact is highly undesirable for the second MOT, since the radiation pressure balance in the trap is changed and the trapping behavior deteriorates. Indeed we could verify that the performance of the second MOT was significantly worse, if the trapped atoms were visibly shifted by the pushing beam. In order to ensure an undisturbed operation of the target trap, the pushing beam is thus aligned as sketched in figure

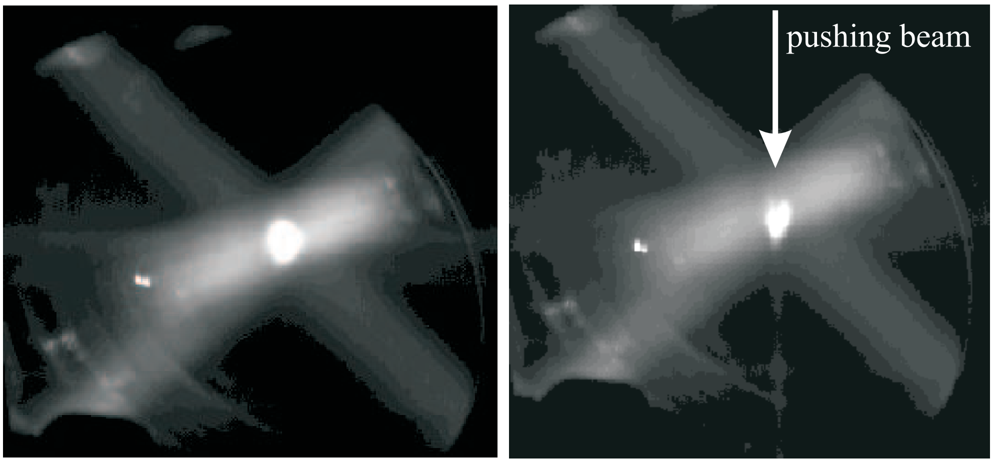

Figure 3.16: Reservoir MOT without (left picture) and with (right picture) pushing beam. The orientation of the pushing beam is indicated by the white arrow in the right picture. The bright spot in the middle (about 3 mm diameter) is the MOT. The trapping beams, which can be seen due to the fluorescence of the background gas, do not seem to be arranged rectangular because of the perspective of the camera.

3.17. The beam is focused into the upper MOT to a waist of about 200 μm. At the position of the lower MOT, the beam has a waist of about 6 mm. In the experiment, the power of the pushing beam varied between 400 μW and 800 μW detuned 15 MHZ from resonance. This is equivalent to about 20 times the resonant saturation intensity I_s of Rubidium at the position of the source MOT, while it amounts to about 1/200 of the saturation intensity at the UHV MOT. Thus the radiation pressure on the upper MOT saturates, while the effect on the lower MOT is very small. No significant changes in the transportation efficiency could be observed within that power range, as expected from the estimates of the radiation force strengths.

Another important detail illustrated in figure 3.17 is the absence of light resonant to the repumping transition during the transport. Except in the two MOT capture regions, the atoms are not pumped back into the $F = 2$ ground state. Given the parameters of the pushing beam, it takes thus only a few hundred μs, until the atoms are excited off-resonantly to the $F' = 2$ state and decay into the $F = 1$ ground state. Since the atoms do not interact then any more with the pushing beam or cooling light, they move without further acceleration by the pushing beam downwards. Also, they can not be deflected by stray light from the cooling trapping laser beams.

The pushing beam is operated continuously and thus produces a continuous atomic beam. To characterize the atomic beam, it was probed rectangular to its orientation with a laser beam. The optical frequency was resonant to the cooling laser transition but modulated with a modulation depth of half a natural linewidth of the transition, with a modulation frequency of 26 kHz. The resulting fluorescence from the atomic beam was collected into an optical wave guide and led to a photomultiplier. The photomultiplier output was demodulated in a lock-in amplifier.

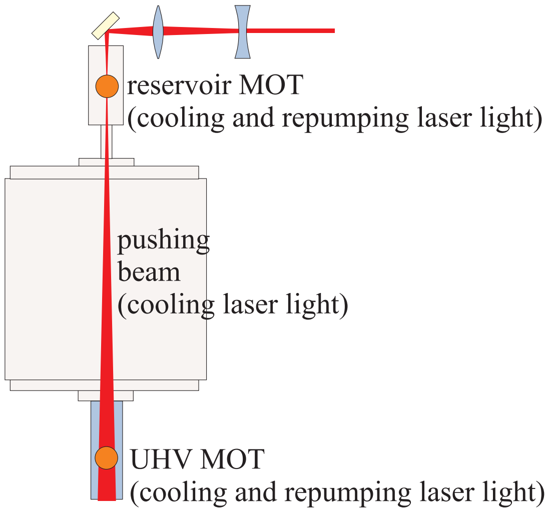
reservoir MOT
(cooling and repumping laser light)
pushing
beam
(cooling laser light)
UHV MOT
(cooling and repumping laser light)

Figure 3.17: Alignment of the pushing beam. The pushing beam is focussed into the upper reservoir MOT. For details see the text.

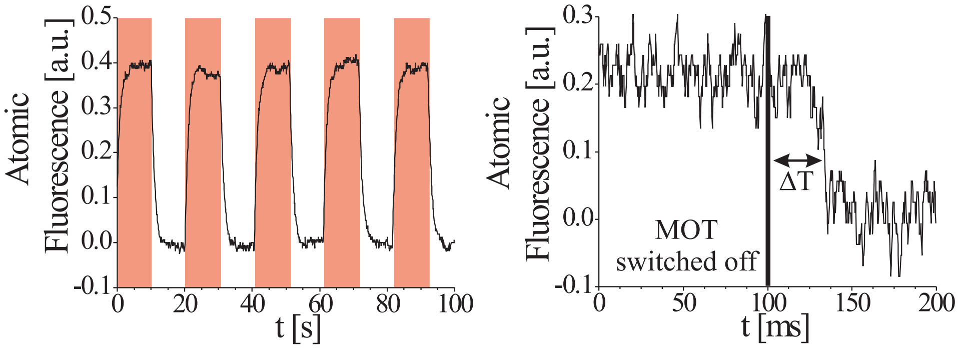

Figure 3.18: Characterization of the atomic transfer beam. The left picture illustrates the dependance of the detected fluorescence signal on the operation of the reservoir MOT. For the durations highlighted in red, the reservoir MOT was operating. The integration time of the used lock-in amplifier was 1 s. The right figure shows a longitudinal velocity measurement of the atomic beam. At $t = 100$ ms the reservoir MOT is switched off; the delay ΔT corresponds to the transport time from the upper MOT to the detection region. Integration time of the lock-in amplifier is 1 ms.

Typical data is presented in figure 3.18. The atomic beam could be effectively switched on and off by turning the magnetic field of the reservoir MOT on and off.

One critical parameter, that can be determined by means of this technique is the velocity of the atoms when they arrive in the capture region of the lower MOT. The time delay ΔT between turning off the MOT and the decay of the atomic fluorescence can be measured with an adequate integration time of the lock-in amplifier. This delay is about 35 ms for the data presented in figure 3.18.

The velocity of the atoms can be calculated from the known travel distance and the time

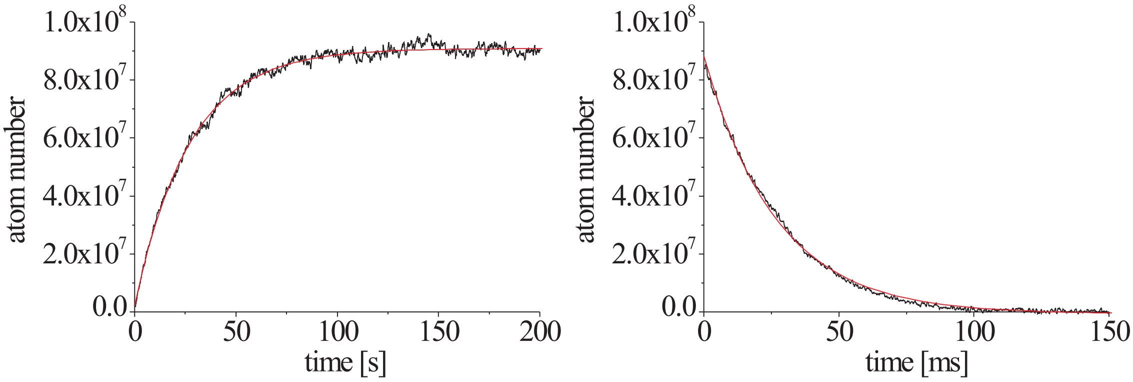

Figure 3.19: Loading and decay curves of the UHV MOT. Left image: Loading of the UHV MOT by the atomic beam from the upper MOT. Right image: Decay of the UHV MOT after switching off the pushing beam. Both data sets can be fitted with exponential curves.

delay ΔT. The measured velocities varied slightly depending on the parameters of the reservoir MOT and the pushing beam, but were usually on the order of 10 m s^{-1}. This velocity is well below the maximum capture velocity of the lower MOT, so that all atoms of the pushing beam entering the MOT region can be decelerated and trapped in principle [81].

The transfer efficiency of the scheme can be estimated using the loading curves of both MOTs. For the reservoir MOT, losses due to the pushing beam are much higher than through other loss channels, which can therefore be neglected. The loading rate of atoms into the trapping region will not be changed much, since the pushing beam acts only within a small fraction of the total capture region. As the upper MOT is in equilibrium, this means that the rate of atoms sent into the atomic beam must be equal to the rate of atoms loaded in the MOT at normal operation (i. e. without pushing beam).

For the lower MOT one can assume that all atoms in the atomic beam reaching the trapping region should be trapped as discussed above. So the rate of delivered atoms can be measured by determining the capture rate of the second MOT.

Thus the efficiency of the transfer beam can be computed as the ratio of the loading rates R_1 and R_2 of the two MOTs. Typical values are $R_1 = 10^9$ s^{-1} and $R_2 = 4 \cdot 10^7$ s^{-1}, leading to an efficiency of 4%. This is considerably lower than predicted in the original papers (efficiency of 50 %) [89, 90], but comparable to results obtained at other experiments (e. g. below 10% at the BEC experiment of Nir Davidsons group [91]).

It should be mentioned, that the alignment of the transfer beam is one of the most sensitive parameters within our setup and requires daily optimization in order to achieve a large atom number in the second MOT. We attribute this fact primarily to small drifts of both the position of the upper and lower MOT.

The UHV MOT

The second MOT in our apparatus is situated in the glass chamber at the bottom of the setup. In contrast to the first MOT, the necessary six beams are not produced by retro-reflecting three beams into themselves, but by aligning six independent beams. This grants greater control of the atomic cloud position than the three-beam setup used in the first MOT. Also, for a large number of atoms in the trap, the cloud becomes optically thick and the profile of a beam passed once through the cloud is severely changed from the initial Gaussian profile (e. g. by diffraction effects). On the one hand, using such a changed beam profile for the counter propagating beam could limit the achievable maximum atom number, on the other hand it might also lead to problems during the transfer into the magnetic trap (cf. 3.4.2).

The detailed setup for adjusting the power balance among two counter-propagating beams is shown in the appendix A.1. The diameter of each MOT beam is about 1.5 cm and each beam about carries a power of about 4 mW. The detuning for the cooling laser is 15 MHz as for the upper MOT, since both MOTs are operated from the same laser source. Just like for the upper MOT, the repumping laser (about 3 mW power) is superimposed only perpendicular to the transfer beam.

In figure 3.19 typical loading and decay curves for the lower MOT are displayed. Both curves are strongly influenced by the alignment of the trap laser beams. Therefore the alignment was checked at the beginning of each experiment with the help of apertures fixed rigidly to the vacuum system. These curves have been obtained with the fluorescence measurement technique. The loading time of the MOT, as determined from these curves, was 27 s ($1/e$ time of the exponential fit). While this time can be regarded as a typical value for the MOT, the decay time — which here is of the same magnitude — has a strong dependance on the MOT alignment and varied accordingly from day to day. Loading curves were also monitored during experiments in order to trigger further experimental steps, thus guaranteeing the same atom number at the beginning of all individual experiments.

We know from absorption images that our MOT is about 4 mm large in diameter (the diameter being defined as twice the $1/e^2$ radius of a fitted Gaussian distribution). Taking into account the other parameters of the MOT one would rather assume from simple theoretical models [81] diameters less than one millimeter. The deviation could be evidence for the density of our MOT being limited by radiation trapping, as explained in 3.3.1.

The temperature in the MOT was usually in the range of 100 μK. Atom numbers varied between $3 \cdot 10^8$ to $4 \cdot 10^8$.

The atom number and temperature of the lower MOT are crucial points that need to be monitored regularly during the experiment. Often the most time consuming part of the daily alignment and preparation process was to optimize these MOT parameters up to a satisfactory level.

3.4 Magnetic traps

Magnetic traps offer a nearly perfect realization of a conservative potential for atom trapping. By choosing a suitable coil arrangement as described below, harmonic potentials can be realized to a very good approximation. The main experimental challenge is to transfer the atoms efficiently from a MOT into a magnetic trap.

3.4.1 Magnetic trapping

Magnetic forces on neutral atoms have already been observed before the advent of laser cooling. A well known example is the Stern-Gerlach experiment [92]. The force exerted on an atom can be deduced semiclassically to be $-\nabla(-\vec{\mu}\cdot\vec{B})$ [93, 81], $\vec{\mu}$ being the atomic magnetic dipole moment. However, only since it was possible to cool atoms to sufficiently low temperatures, it was feasible to trap atoms magnetically. The first magnetic atom trap was realized in 1985 [94].

Magnetic trapping is easier to describe in terms of a conservative potential than in terms of forces. The semiclassical potential $\vec{\mu}\cdot\vec{B}$ corresponds to the variation of the ground state energy by the Zeeman effect. For a spatially inhomogeneous magnetic field $\vec{B}(\vec{r})$, the magnetic potential is thus given by (g_F being the Landé factor and μ_B the Bohr magneton)

$$U_{\mathrm{mag}}(\vec{r}) = \vec{\mu}\cdot\vec{B}(\vec{r}) = g_F m_F \mu_B B(\vec{r}). \tag{3.28}$$

Here the direction of the magnetic field is chosen as the quantization axis for the last equality sign and the atom is assumed to be in one of its m_F ground states. As our atoms are usually very cold and thus move slowly, their spin follows the external field adiabatically. Once the atoms are prepared appropriately (e. g. by optical pumping), the orientation of the atomic spin relative to the magnetic field remains, i. e. they stay in the same m_F state. One notable exception from this is the occurrence of Majorana spin flips at low magnetic fields as discussed in section 3.4.3.

The simplest coil configuration to trap atoms magnetically is the so called *anti Helmholtz* setup. Here two coils are placed in Helmholtz configuration, only that the current sense of one coil is reversed with respect to the other one (as sketched in the graphical illustration for the MOT coils in figure 3.12). Close to the center of the setup, this produces a quadrupole field of the form

$$\vec{B}(\vec{r}) = \zeta \begin{pmatrix} x \\ y \\ -2z \end{pmatrix}. \tag{3.29}$$

ζ is referred to as the *magnetic field gradient.* This gives

$$B(\vec{r}) = \zeta\sqrt{\rho^2 + 4z^2} \tag{3.30}$$

for the absolute value of B appearing in the last part of equation (3.28).

The quadrupole trap is of special importance, because it also provides the necessary magnetic field to operate a MOT. However, the magnetic fields in a MOT are commonly

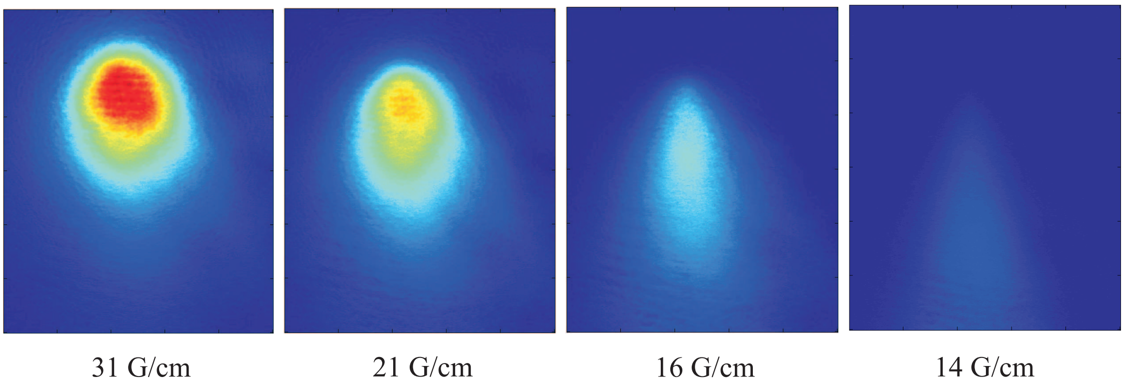

Figure 3.20: Minimum magnetic gradient to support against gravity. The absorption images were taken while the atoms were trapped with different magnetic gradients. For all images the same color encoding scheme is used. The shape and intensity of the recorded images are influenced also by the Zeeman effect. Since atoms farer away from the trap center are detuned from resonance and thus contribute less to the absorption signal.

smaller than those for a magnetic trap. The gradient in the strong direction for our MOT is about 6 G/cm, leading to a gradient of about 3 G/cm in the vertical direction. To overcome gravity by purely magnetic forces, a minimum gradient of 15.2 G/cm is required. For our coil system, this corresponds to a current of 1 A through the coils for the MOT and approximately 5 A for the quadrupole trap. The minimum magnetic gradient necessary to compensate gravity can be verified experimentally as displayed in figure 3.20.

In our setup, the maximum attainable trap depth depends on the maximum current which can flow through our coils, and the spatial extensions of the vacuum cell. The maximum current is limited by our ability to conduct away the heat which is generated by ohmic losses inside the coils. With water cooled coils, we routinely have 25 A passing the coil system, which amounts to a power dissipation of about 500 W. The maximum current leads to a gradient of approximately 150 G/cm in the x and y directions. Given, that the wall of the glass cell is about 1 cm away from the center of the magnetic trap, this amounts to a maximum trap depth corresponding to $k_B \cdot 10$ mK. The properties and parameters of our coil system were examined in detail in [50].

At temperatures of several tens of μK, atom losses in the magnetic trap occur mainly through scattering of resonant light and through collisions with background gas. If near resonant light is present, the atoms can change as well their m_F as their F quantum number. Since the magnetic potential depends on both these quantum numbers, a change might flip the sign of the induced Zeeman energy and converts the trapping potential into an anti-trapping one. This would expel the atoms from the trap.

Collisions with “hot” atoms from the background gas usually transfer enough energy onto a trapped atom for leaving the trapping region. A rule of thumb is to expect a life time of 1 s for a background pressure between 10^{-8} and 10^{-9} mbar.

Heating of an atomic cloud trapped in a magnetic trap can occur due to technical imperfections. Since the trapping potential is not harmonic, atoms of different energies oscillate with different frequencies. If the magnetic trapping field exhibits a significant noise component within that frequency band, the atoms are resonantly heated. Similarly, if atoms are exposed to a frequency component twice their oscillation frequency, they will be heated parametrically.

A noisy magnetic field usually results from a noisy power supply. For BEC experiments requiring storage times of 100 s and more, a relative stability of the power supply below 10^{-3} is sufficient [34]. The power supply used in our experiment (Sorensen DCS33-33E) produces a magnetic field exhibiting noise spikes at 50 and 100 Hz with a relative field amplitude of $2 \cdot 10^{-4}$, as measured with a Hall probe based on the SS94A2 chip by Honeywell.

Another source of heating which has been observed experimentally, is that of a dilute cloud of much hotter atoms (i. e. temperatures in the mK range instead of in the μK range). Since the atoms within such a hot cloud occupy a much larger volume than the cold cloud of atoms, its density is much smaller and it is harder to detect. In analogy to the cloud of comets at the edge of our solar system [95], this cloud has been named *Oort cloud*. Because of its low density, the thermal coupling to the cold atom cloud is rather small. The direct detection of such a hot cloud is difficult and little systematic study on this subject exists in the literature [96, 97]. Nevertheless it is frequently mentioned (e. g. [98, 99, 100]) and from discussions with other groups in the field I know that many groups observe related phenomena. Origin and properties of the Oort cloud are still a matter of discussion and seem to depend largely on experimental details.

3.4.2 Measurements in the magnetic quadrupole trap

Transfer from the MOT into the quadrupole trap

One of the most critical points of our experiment is the transfer of the atoms from the MOT into the magnetic quadrupole trap. The transfer process is designed to achieve a high atomic density in the magnetic trap simultaneously with a low temperature. This leads to an optimized phase space density. Furthermore, this also maximizes the collision rate of the atoms in the trap, which is crucial for the following step of evaporative cooling. The general strategy consists in first preparing the cloud as dense and cold as possible using near resonant light, then pumping the atoms optically to an appropriate hyperfine ground state and at last capturing them in the magnetic trap by switching the magnetic fields on.

The equilibrium distribution of the atoms in the MOT does not necessarily resemble the equilibrium distribution of the cloud in the magnetic trap. If the transferred cloud in the magnetic trap is to far from its equilibrium distribution in thebeginning, it will possibly increase its volume and raise its temperature. Both processes decrease the initial phase space density.

This problem is minimized, if the cloud size in the MOT at a temperature T is comparable to the the size of a cloud trapped in the magnetic trap with the same temperature T. This can be accomplished by manipulating the cloud with light forces immediately before the transfer and by choosing an appropriate magnetic gradient for the quadrupole trap. However, the last option is usually not very flexible. To support the atoms against gravity, a minimum gradient must be applied. We usually found for the temperatures of our MOT, that the adequate size of a magnetically trapped cloud at this gradient was already significantly smaller than our MOT.

Therefore, the first step of the transfer process aims to match the sizes of MOT and magnetic trap by compressing the MOT. For this purpose, the magnetic field gradient is increased from 6 G/cm up to 18 G/cm and the cooling laser detuned from 15 MHz to 25 MHz away from the resonance. The change of the magnetic gradient raises the restoring force of the MOT (cf. equation (3.23)) and leads thus to an increase of the density. The increment of the detuning diminishes the effects of radiation trapping, which counteracts a further compression of the MOT. Since the trap depth of the MOT is greatly reduced with this high current and detuning, the MOT is compressed for only 20 ms. Typically, the radius of the atomic cloud is reduced by a factor of 1.5, leading to an increase of the density by a factor of 3.4.

After this, the magnetic fields are switched off and the atoms are exposed to an optical molasses. To reach optimal results, the cooling lasers have to be further red-detuned. In most runs leading to a BEC we used a detuning of 90 MHz. The molasses is applied for 3 ms. One should note, that the magnetic fields need about 1 ms to decay to a negligible level, which can be explained by eddy currents arising in the copper housing of the coil holder due to the switching process. Therefore pure polarization gradient cooling is applied effectively only for 2 ms. After this cooling stage, we had a cloud with typically $2.8 \cdot 10^8$ atoms at a peak density of $1.0 \cdot 10^{10}$ cm^{-3} and a temperature of 50 μK.

In the next step, the atoms are pumped into the $|F = 2, m_F = 2\rangle$ state (which I refer to as $|2, 2\rangle$ in the following). This state guarantees the tightest confinement in the magnetic trap due to its largest Zeemann shift of all ground states. The optical pumping stage is implemented by two collinear σ^+-polarized laser beams, one of which is resonant to the transition $F = 2 \rightarrow F' = 2$ and the other one resonant to the $F = 1 \rightarrow F' = 2$ transition. Typical parameters were 200 μW for the first and 50 μW for the latter beam. Both beams had a cross section of approximately 1 cm^2. The quantization axis for the atom was given by a homogenous magnetic field on the order of one Gauss parallel to the beam propagation direction. Note, that the quantization axis in the magnetic trap is given by the local magnetic field, which is not homogenous. Since the Larmor frequency of the atoms in the pumping field (which overlaps in time with the magnetic trap field) is greater than 1 MHz, the fastest switching times we can realize with our coil system are still so long, that the spins of the atoms adiabatically follow the external field. Thus in principle all optically pumped atoms can be transferred into the trap.

The pumping scheme is visualized in the left half of figure 3.21. After the atoms are optically pumped into the $|2, 2\rangle$ state, they do not interact any more with any optical pumping laser. In contrast to that, a scheme employing the transition $F = 2 \rightarrow F' = 3$ would increase the number of scattered photons once the atoms are in the $|2, 2\rangle$ state due to the maximally large Clebsch-Gordan coefficient for the transition $|2, 2\rangle \rightarrow |3, 3\rangle$, as indicated by the dashed line in figure 3.21. This would make the scheme much more

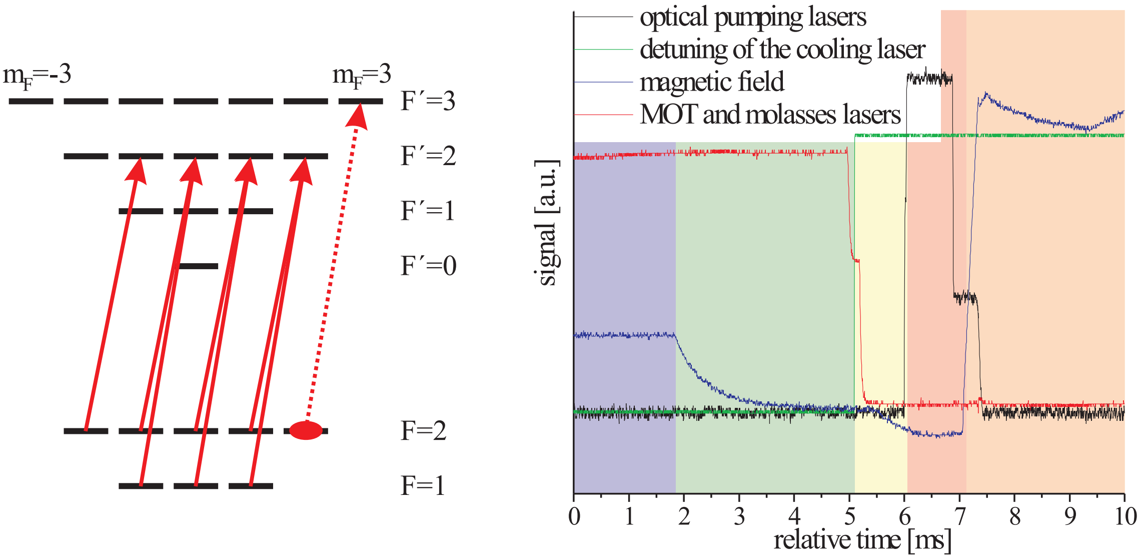

Figure 3.21: Transfer from the MOT into the quadrupole trap. Left figure: Illustration of the optical pumping scheme. Lasers resonant to the $F = 2 \rightarrow F' = 2$ and $F = 1 \rightarrow F' = 2$ transitions are used. The pumping collects the atoms in the $|2, 2\rangle$ ground state (marked with the red ellipse), which does not couple to the σ^+ polarized laser beams. Right figure: Stages of the transfer into the magnetic trap, as described in the text. Blue — compressed MOT. Green — optical molasses. Yellow — delay time for tuning the optical pumping laser. Red — optical pumping. Orange — capture of the atoms in the magnetic trap. Further details in the text.

sensitive to the incident light power.

Nevertheless, we found that the exact parameters at this stage had to be checked regularly by measuring the transfer efficiency into the magnetic trap. Instead of changing the power of the incident beams, it is more convenient to adjust the duration of the optical pumping stage. At a total time of 1 ms, differences of 100 μs often changed the performance of the transfer significantly. The laser resonant to the repumping transition $F = 1 \rightarrow F' = 2$ was left on a few 100 μs longer, to ensure all atoms were in the $F = 2$ ground state.

After the optical pumping stage, the field of the magnetic trap is switched on as fast as possible. We found that a good “mode matching” between the MOT and the magnetic trap could be achieved for a gradient of 54 G/cm in the vertical (i. e. the x-) direction. The rise time of the magnetic field was approximately 300 μs. Temperature and atom number in the magnetic trap varied on a daily basis. We obtained typically 120 μK and $2.3 \cdot 10^8$ atoms.

We achieve a transfer efficiency of 70%, which is comparable or better than values reported from other experiments. In addition to the optical pumping times discussed above, in particular the position of the MOT relative to the magnetic trap has to be adjusted often. By slight changes of the power balances in each MOT arm we arranged the cloud to be at the same position as the magnetic trap.

The whole transfer process is illustrated in the right half of figure 3.21. Shown are photodiode (Hall sensor) signals resulting from the relevant laser sources (the magnetic fields). A more schematic overview is presented in appendix A.2 within the given timing sequence for a complete BEC experiment.

Adiabatic compression in quadrupole trap

Once the atoms are held in the magnetic trap, the current passing through the coils is slowly raised to the maximum value of 25.6 A. The aim here is to increase the density of the atomic cloud, which leads to more favorable conditions for the evaporative cooling step.

The magnetic potential is adiabatically increased with respect to the atomic motion in the trap. A signature of this adiabacity is the conservation of the initial phase space density. This condition can be used to calculate the expected rise in temperature and peak density. According to the discussion on equation (2.7), the dependance of the phase space density PSD on the peak density, temperature T and current through the coils I_{coil} is given by

$$PSD = n_{\text{peak}}\lambda_{\text{dB}}^3 \sim n_{\text{peak}}T^{-3/2} \sim I_{\text{coil}}^3 T^{-9/2}, \tag{3.31}$$

since, within the regime of the Boltzmann distribution, $n_{\text{peak}} \sim (\zeta/T)^3 \sim (I_{\text{coil}}/T)^3$. Here ζ is the gradient of the quadrupole field as defined in equation (3.29). For a constant phase space density, equation (3.31) thus yields the following equations for the ratios of the initial and final density and temperature

$$\frac{n_{\text{peak,final}}}{n_{\text{peak,initial}}} = \frac{I_{\text{coil,final}}}{I_{\text{coil,initial}}} \tag{3.32}$$

$$\frac{T_{\text{final}}}{T_{\text{initial}}} = \left(\frac{I_{\text{coil,final}}}{I_{\text{coil,initial}}}\right)^{2/3}. \tag{3.33}$$

Since the collision rate $1/\tau_{\text{col}}$ of the atoms scales as $1/\tau_{\text{col}} \sim n\overline{v} \sim nT^{1/2}$, the collision rate therefore increases as

$$\frac{1/\tau_{\text{col,final}}}{1/\tau_{\text{col,initial}}} = \left(\frac{I_{\text{coil,final}}}{I_{\text{coil,initial}}}\right)^{4/3}. \tag{3.34}$$

We verified these scaling laws experimentally by increasing the magnetic field from a gradient of 56 G/cm to a gradient of 150 G/cm within different times. The heating of the cloud and the increase of the density was in good agreement with the theoretical predictions, if the rise time was longer than 0.5 s.

In the subsequent experiments, the adiabatic compression was either performed within one second before or during the transport to the QUIC trap (cf. 3.4.3).

Life time

As pointed out, the main purpose of the magnetic trap technology is to provide a container that stores cold atoms for more than 100 s. We checked the life time of the atoms in the

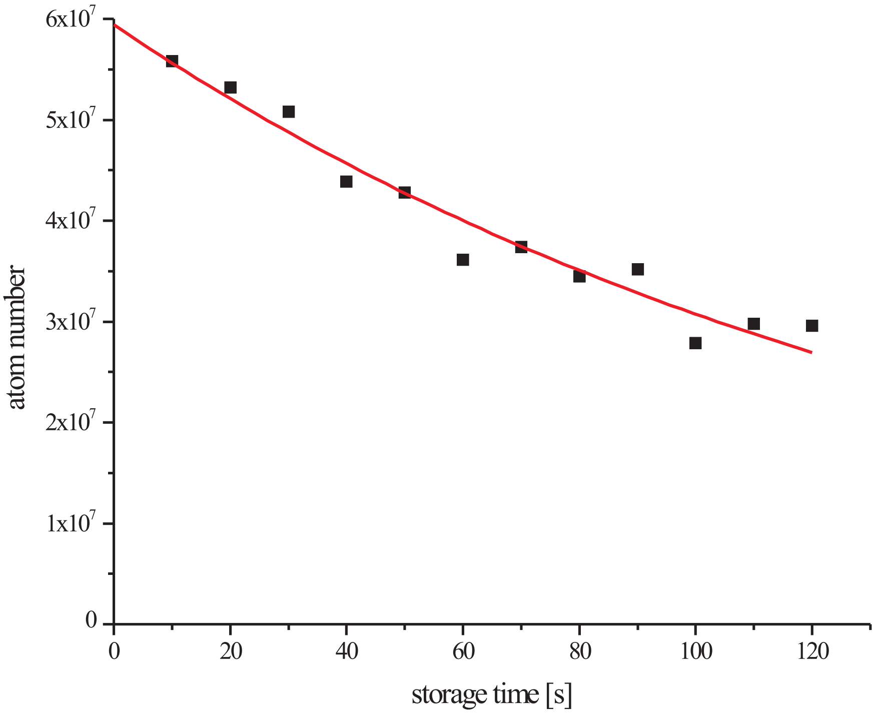

Figure 3.22: Storage time in the quadrupole trap. The atom numbers were determined with the absorption imaging method. The fitted exponential decay yields a $1/e$ life time of (152 ± 11) s.

magnetic trap frequently, especially after modifications that might affected the vacuum conditions.

A typical example is shown in figure 3.22. The data fits well to an exponential decay curve with a time constant of 152 s ± 11 s. The exponential curve is expected for trap losses dominated by background gas collisions. We also observed drastic reductions of the measured storage time if near resonant light from the diode lasers was not shielded properly.

Surprisingly, also the vacuum gauge had a major, not completely reproducible influence on the storage time. If the gauge was operated, the storage time was shortened by a factor of up to three, reducing the measured time down to 50 s. Since the reading of the gauge was always below $2 \cdot 10^{-11}$ mbar, this can not be explained by an increase of the background vapor pressure. The mechanism leading to the shortening of the life time remains still unclear. The gauge stayed switched off for all measurements performed in the magnetic traps.

Heating of the cloud

In all measurements in the quadrupole trap we observed a heating of the trapped atoms. The heating can be described with an exponentially decaying curve. A typical example is

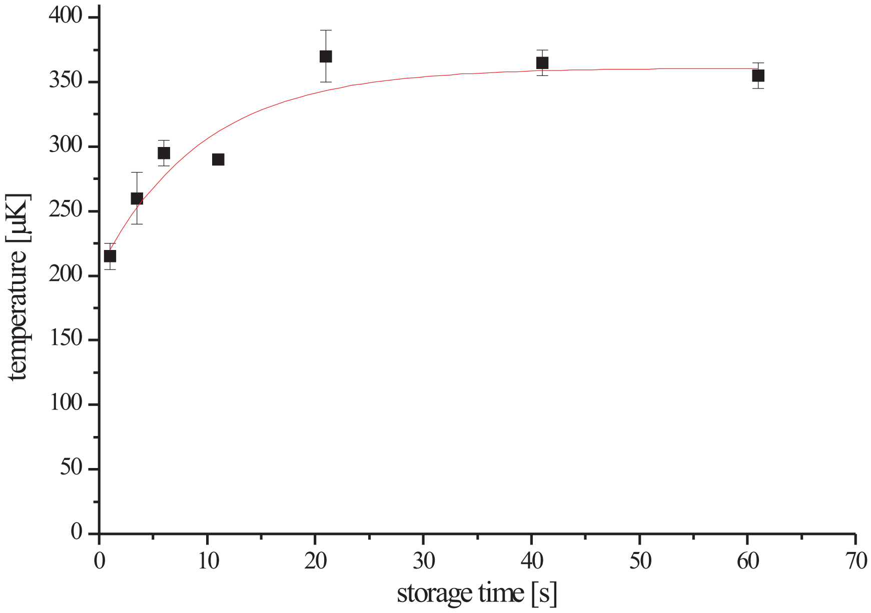

Figure 3.23: Heating of atoms in the quadrupole trap. The red curve is a fitted exponential function with a time constant of (9.5 ± 1.9) s.

displayed in figure 3.23.

Although we spent a significant amount of time on resolving the origin of this heating process, it is still not completely understood. I exclude the above mentioned technical possibilities, i.e. influence of stray light and fluctuations of the magnetic field. Stray light can not be responsible for the heating, as it would also strongly influence the storage time in the trap. This is contrary to our observations. Further, the influence of stray light on the trapped atoms should highly depend on the detuning of the lasers from the atomic resonance, but we could not observe any correlation between the laser detuning and the heating rate in the magnetic trap. The magnetic field was measured with a sensor and its relative noise components in the relevant (for parametric or resonant heating) frequency range is below 10^{-4}. As mentioned above, fluctuations at this level are negligible for the trapping of the atoms.

The range of possible mechanisms is furthermore severely limited by the observation, that the heating process stagnates after some time and the temperature of the atoms remains constant. This suggests some thermalization effect as underlying mechanism, in which additional energy from the loading sequence is distributed among the atoms.

If the shape of the cloud before the transfer into the magnetic trapping is matched badly to the magnetic trap potential, one could expect some heating, since exceedingly much Zeeman energy is added to the atoms. We varied the shape of the cloud before loading into the magnetic trap, but we found no significant correlation between the heating rate and the cloud shape. So I exclude also this possible origin for the heating effect. This is also in agreement with the observation in other groups, that the initial cloud shape is only

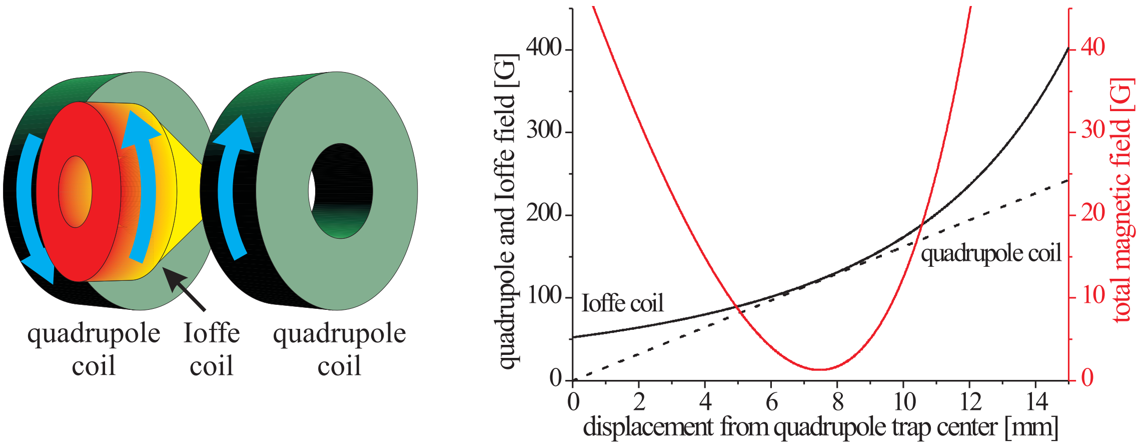

Figure 3.24: QUIC setup. Left image: geometric arrangement of the two quadrupole coils and the Ioffe coil. The Ioffe coil is conical in order to allow the MOT beams to pass. The blue arrows indicate the direction of the current. Right image: magnetic fields on the symmetry axis of the Ioffe coil versus displacement from the position of the quadrupole trap. The quadrupole and Ioffe field have opposite signs and cancel each other partially; in the plot the dipole field has been mirrored at the $x = 0$ G axis. Note the different scale for the resulting field $B_{\text{total}} = |\vec{B}_{\text{quadrupole}} - \vec{B}_{\text{Ioffe}}|$.

of minor importance.

A remaining explanation is an existing Oort cloud. A hot cloud of atoms would thermalize with the cold atoms in the magnetic trap and thus lead to a limited heating. Since such a high energy cloud is not directly observable, there is only indirect evidence for this assumption. One supporting indication is the fact, that no heating is observed once the atoms are transferred to the QUIC trap (see next section). This trap is located closer to the glass wall than the quadrupole trap. Therefore significantly hotter atoms than those trapped initially would collide with the wall and do not contribute to heating any more.

3.4.3 Measurements in the QUIC trap

The quadrupole and Ioffe configuration (*QUIC*)

Because of the spatial overlap between MOT and quadrupole trap, this trap is very suitable for the transfer of atoms from the MOT into a magnetic trap. However, it has a minimum of the magnetic field of 0 G. Atoms close to the zero crossing of the field can undergo *Majorana spin flips* [101]. If the relative change of the magnetic field $|\frac{d}{dt}\vec{B}|/|\vec{B}|$ is comparable or faster than the Larmor frequency $|\vec{\mu} \cdot \vec{B}|/\hbar$, the atomic spin does not follow the external field any more. This is a loss mechanism for atoms trapped in a magnetic trap, since the atoms eventually change the sign of their m_F quantum number and the binding potential is changed into an anti-binding one. Because the Larmor frequency is proportional to the magnetic field, this occurs if the external field vanishes.

This problem is cured in our setup by the addition of a third coil, the *Ioffe coil* (named after M. S. Ioffe, who suggested magnetic traps of similar design in the 60s for the magnetic storage of plasmas). This coil is placed as shown in figure 3.24. In our setup, the two quadrupole coils and the Ioffe coil are mounted on one common holder, ensuring a mechanically stable alignment. In the far field, the Ioffe coil creates a magnetic dipole field, which scales as I_{coil}/z^3. If dimensioned correctly, as shown in the right half of figure 3.24, the combined field of the three coils produces a minimum in the absolute of the field on the symmetry axis of the Ioffe coil. This configuration was introduced in the context of ultracold atom trapping in [102].

The minimum arises if the gradient of the dipole field just compensates the quadrupole magnetic field. Using a Taylor expansion of the total field, one can see that the shape of the field around the minimum is determined by the next lowest, i. e. the quadratic, term. Thus the constructed trap is harmonic around the minimum. Because of its rotational symmetry, the trapping potential $V(\rho, z)$ can be parametrized as

$$V(\rho, z) = \mu B(\rho, z) = \frac{1}{2} m \left(\omega_\rho^2 \rho^2 + \omega_z^2 z^2 \right) + \mu B_0. \tag{3.35}$$

Here m is the mass of the trapped atoms, ω_ρ and ω_z are the trap frequencies and B_0 the magnetic offset field. Note, that the axis labelled with z for the QUIC trap is the symmetry axis of the Ioffe coil and is perpendicular to the z-axis of the quadrupole system as defined by equation (3.29). In the following, if I refer to the z-axis, I always refer to the z-axis of the QUIC trap.

Using the conditions $dB_{\text{quadrupole,z}}/dz = -dB_{\text{Ioffe,z}}/dz$, $\vec{\nabla} \cdot \vec{B} = 0$ and the symmetries of the setup, one can find explicit expressions for the trap frequencies as

$$\omega_z = \frac{2}{6^{\frac{1}{8}}} \sqrt{\frac{\mu \zeta^{\frac{5}{4}}}{m p^{\frac{1}{4}}}} \tag{3.36}$$

$$\omega_\rho = \frac{3}{2} \zeta \sqrt{\frac{\mu}{m B_0}}. \tag{3.37}$$

Here ζ is the gradient of our quadrupole system, p the magnetic dipole moment of the Ioffe coil and m the mass of the trapped atoms.

For achieving high densities and collision rates of the trapped sample, it is desirable to make the trap as steep as possible, i. e. the trap frequencies should be high. According to equations (3.36) and (3.37), this can be realized by choosing a small offset field B_0. For our setup $B_0 = 1.30$ G. This is still high enough to prevent Majorana spin flips and leads to values of the trap frequencies of $\omega_z = 2\pi \cdot 21.5$ Hz and $\omega_\rho = 2\pi \cdot 272$ Hz. A more detailed discussion on the measurement of these parameters is given in section 4.1.1. At a trap depth corresponding to $k_B \cdot 25\ \mu$K, the deviations from a purely harmonic potential are 2.5 % in the radial direction and 0.6 % in the axial direction.

For providing a stable magnetic field it is advantageous to connect all three coils in series. In this case, the noise cancels itself around the minimum to the same degree as the DC fields do. However, this only holds, if the noise from the different coils is perfectly correlated. This is easiest to guarantee if the coils are connected in series.

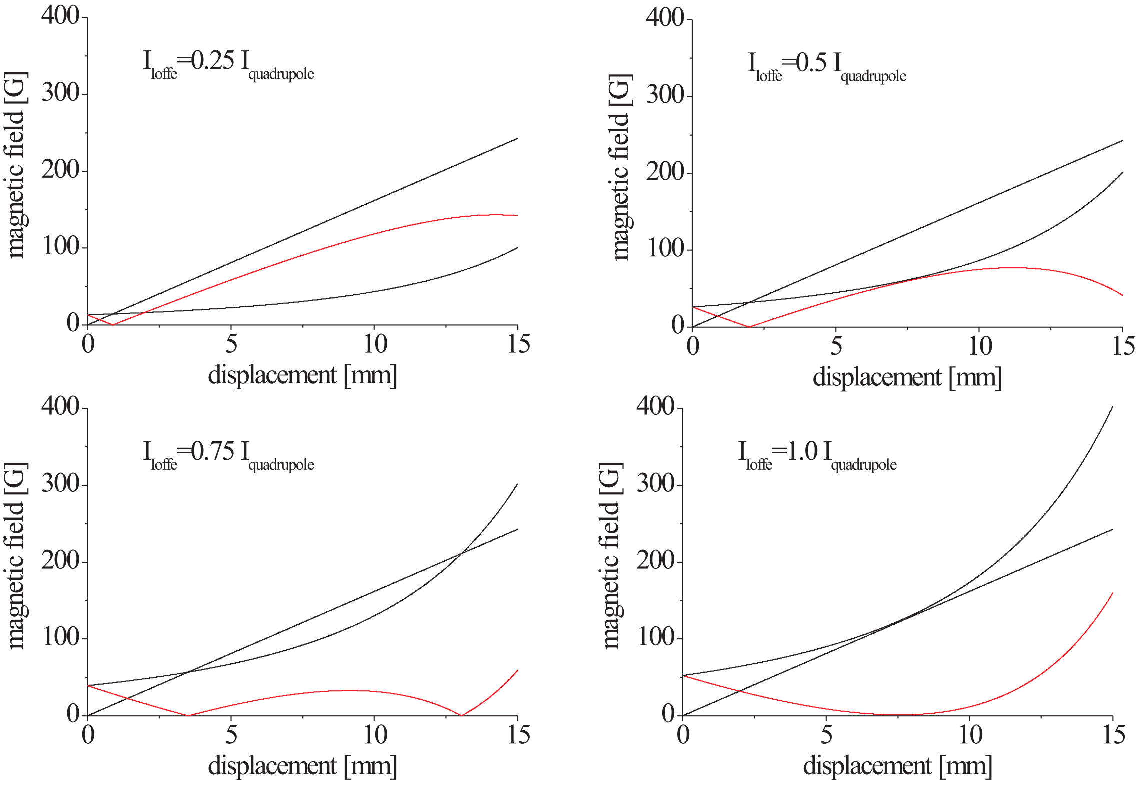

Figure 3.25: Magnetic fields for the transfer into the QUIC trap. The magnetic field due to the quadrupole coils and the negative field of the Ioffe coil for $I_{\text{quadrupole}} = 25.6$ A are shown in black color. The absolute value of the total magnetic field is plotted in red color. The displacement is measured from the center of the quadrupole trap towards the Ioffe coil. In the experiment the current through the Ioffe coil is raised continuously; here four snapshots with increasing Ioffe field are shown.

As a consequence for the construction of the setup geometric misalignments of the coil setup can not be compensated by changing separately the current through one coil. Since the coils have to be arranged, such that fields on the order of 100 G cancel exactly up to 1 G, this requires an exact knowledge of the individual magnetic fields and an alignment with a relative accuracy of 0.1 mm.

Transport into the QUIC trap

The transport from the quadrupole trap into the QUIC trap is realized by increasing the current through the Ioffe coil. This is implemented by controlling two power MOSFETs (MTY55N20E, Motorola), which split the current between the Ioffe coil and a resistance (of similar ohmic resistance as the coil, namely 0.1 Ω). First the FETs are switched such that the entire current flows through the resistance. At the end of the transport, the entire current flows through the Ioffe coil. The used transport time was between 1 s and 10 s.

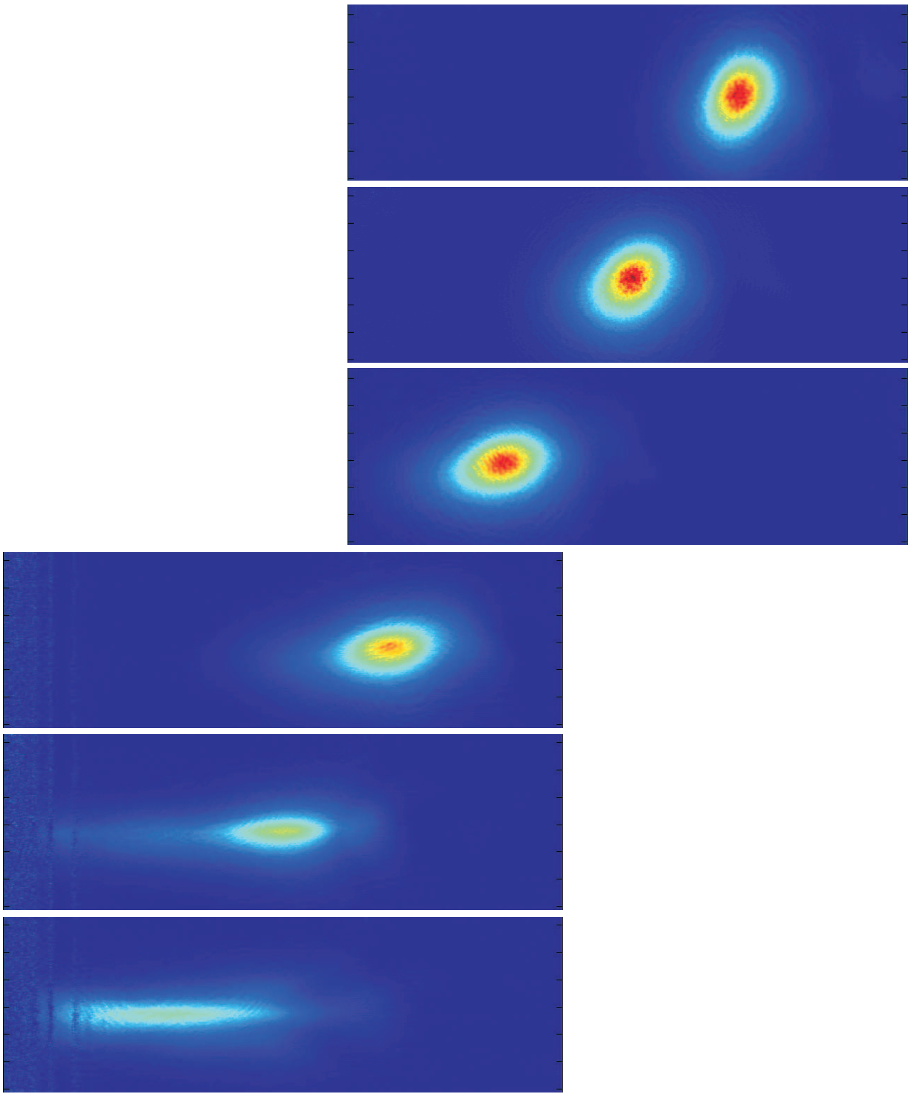

Figure 3.26: Transfer of atoms into the QUIC trap. Shown are absorption images at different positions during the transport. All images use the same color encoding. The most upper picture corresponds to the quadrupole trap, the lowest one to the QUIC trap. In between, the camera position has been shifted. The length of the field of view is 6 mm. The noise at the most left part of the image stems from the edge of the glass cell and resulting diffraction patterns.

As illustrated in figure 3.25, this results in a local minimum, which moves with increasing current from the position of the quadrupole trap towards the position of the QUIC trap. The atom cloud follows the position of this minimum, as long as it progresses slowly compared to the oscillation frequencies of the trapped atoms. As also evident from the figure, another minimum approaches this position from the side of the Ioffe coil. As soon as these two minima meet, the position of either does not change any more with increasing current. Instead, the value of the minimum field is increased from 0 G to 1.3 G.

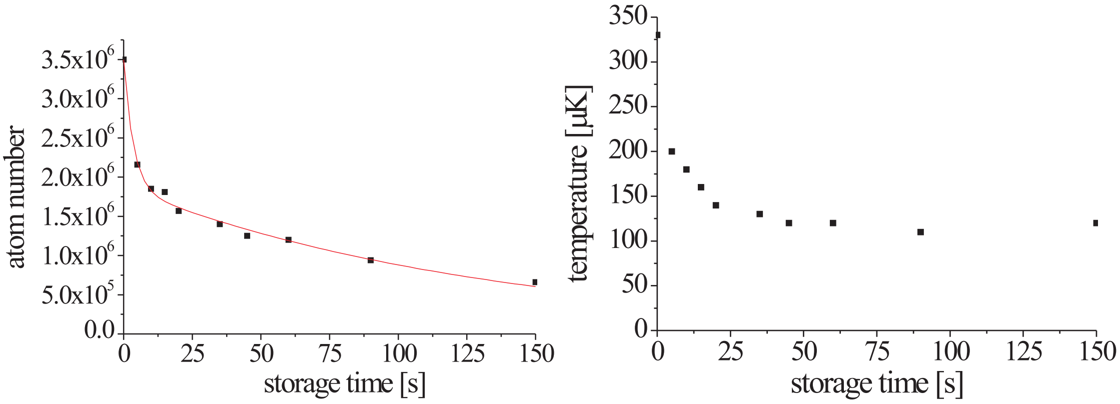

Figure 3.27: Storage in the QUIC trap. Left image: Decrease of the number of atoms in the QUIC trap. The data is fitted with the sum of two exponential functions, taking into account the two loss mechanisms of wall evaporation and background collisions. Right image: Cooling of the atomic cloud, recorded simultaneously with the atom number.

In figure 3.26, this transfer is observed by taking absorption pictures at several positions along the transport. The change of the initially round shape of the quadrupole trap into the lengthy shape of the QUIC trap can be nicely seen. It is also evident, that shortly before reaching the final position, the signal is strongly decreased. The corresponding atom loss results from a too shallow trap at the end of the transport. The minimum trap depth during the transport is reached when the well between the two minima in figure 3.25 is of the same height as the value of the potential at the wall next to the Ioffe coil, since then the atoms with higher total energy are neither held back by the well nor by the potential from colliding with the wall. This trap depth corresponds to $k_B \cdot 240$ μK in our setup. Because this is of comparable magnitude as the atomic cloud's temperature, this leads to a significant loss. This loss was reduced by placing the glass wall as far away from the center of the QUIC trap as possible, which is 3.1 mm in our case. Still, on a transport from the quadrupole trap to the QUIC trap we loose approximately 80 % of the atoms, depending on the temperature of the cloud[2].

Life time and cooling process

The transfer of the atoms into the QUIC trap transports the atoms over a distance of 7.5 mm. As a result, the atoms are now only 3.1 mm away from the next glass wall. This results in an effective trap depth of $k_B \cdot 850$ μK.

We observed a rapid decrease of the atom number, if the atoms were hotter than 120 μK after their transport to the QUIC trap. Simultaneously, the temperature decreased to a steady-state value of about 120 μK. Typical curves, albeit measured in this particular case with less atoms than we usually transferred into this trap, are shown in figure 3.27.

---

[2] This problem was addressed by designing a new coil system, which will be available only after this thesis is completed. The new coil system will facilitate experiments considerably by minimizing the atom loss effect

This observation can be explained by an evaporative cooling effect. The hottest atoms within the sample collide with the wall and are removed from the trapped cloud. This reduces the atom number and the temperature at the same time. The measured data is in good agreement with simple numerical estimates which take the geometry of the trap (e. g. distance to wall, shape of potential) into account.

This initial cooling process in the QUIC trap is not as efficient as the evaporative cooling step applied next. Still, it is important to note, that for typical experimental parameters the phase space density is increased throughout.

After the atoms reach a temperature of about 120 μK, the number of atoms in the sample, which are hot enough to reach the wall, is negligible small and the process stops. As the data points at longer times indicate, the atoms are not heated in the QUIC trap. After 15 s there are typically about $3 \cdot 10^7$ atoms at 120 μK in the trap, yielding a peak density of about $4 \cdot 10^{11}$ cm^{-3} and a phase space density of $2 \cdot 10^{-6}$.

The atom number curve in figure 3.27 is fitted with the sum of two exponential functions. The first function models the loss of atoms by collisions with the wall, while the second curve takes the losses due to collisions with the background gas into account. The life time of atoms in the QUIC trap obtained by this second curve is compatible with the life time in the quadrupole trap.

Typical parameters for the trapped clouds in the various traps are summarized in table 3.1. These are average results, which — according to my experience — guarantee the creation of a BEC in our setup with the last step of evaporative cooling. The figures can thus be regarded as a standard set of parameters, constituting suitable starting conditions for the evaporation process. With moderately worse starting conditions, smaller BECs could usually be achieved with slightly modified evaporation parameters.

Table 3.1: Typical values for the trapped atomic clouds. Given are the atom number N, the peak density n_{peak}, the temperature T and the resulting phase space density PSD. Note, that the average density is a smaller by a factor of 8 for the quadrupole trap and by a factor of $2\sqrt{2}$ for the MOT and the QUIC trap. For details see the text.

Trap	N	n_{peak} [cm^{-3}]	T [μK]	PSD
MOT	$3.5 \cdot 10^8$	$8 \cdot 10^9$	100	$5.4 \cdot 10^{-8}$
after molasses and optical pumping	$2.8 \cdot 10^8$	$1 \cdot 10^{10}$	50	$1.9 \cdot 10^{-7}$
Quadrupole trap	$2.3 \cdot 10^8$	$4 \cdot 10^{10}$	120	$1.9 \cdot 10^{-7}$
QUIC trap	$3.0 \cdot 10^7$	$4 \cdot 10^{11}$	115	$2.1 \cdot 10^{-6}$

3.5 Evaporative Cooling as the final cooling stage

In all successful BEC experiments so far the final cooling step is performed by evaporative cooling. I will therefore sketch the theoretical basis of this technique. Then I will describe the experimental implementation in our experiment and give an overview of our results.

3.5.1 Theoretical considerations

The principal idea of evaporative cooling consists in selectively removing the most energetic particles of an ensemble. This reduces the average energy and therefore, after a rethermalization process, the temperature of the ensemble. In magnetic traps this is implemented by removing all atoms above some threshold energy, therefore truncating the Boltzmann energy distribution of a thermal gas. The atoms rethermalize by elastic collisions towards a Boltzmann energy distribution with a lower temperature. Usually *forced evaporation* is used, i. e. the truncation level is continuously lowered in order to enforce an ongoing cooling effect. Evaporative cooling has been reviewed extensively in [103] and I will only sketch the necessary results here.

The energy threshold E_{thr}, above which all particles are removed, can be parametrized with a dimensionless number η, defined by

$$\eta = E_{\mathrm{thr}}/k_B T. \tag{3.38}$$

Here T is the temperature of the ensemble. For large values of η (which means approximately $\eta > 4$) and in the case of a thermal gas obeying Boltzmann statistics, analytic expressions can be deduced for the most important quantities.

If η is kept fixed during the evaporation process, all quantities scale exponentially with time [103]. This can be explained by noting, that always the same fraction of the atoms has an energy above $\eta k_B T$ and is therefore evaporated. Assuming a Boltzmann distribution, the evaporated atoms will always have the same relative amount of energy compared with the average energy of the particles in the ensemble. Thus the relative loss of energy will remain constant. This leads to the above mentioned exponential scaling laws of temperature and atom number versus time. The connection between the number of trapped atoms N and the temperature T can be cast in the form

$$N(t)/N(0) = \left(T(t)/T(0)\right)^{\alpha}. \tag{3.39}$$

The exponent α can be deduced from η. The relation is given by

$$\alpha = \frac{\eta + 1}{3} - 1. \tag{3.40}$$

A more detailed calculation reveals a physical interpretation of α. It denotes the amount of additional energy, which is removed with an evaporated atom from the trap as compared with the average energy $3k_BT$ of the atoms in the sample. Equation (3.40) also illustrates that increasing η also increases α. Thus in principle, evaporative cooling can be made arbitrary efficient in terms of atom loss by increasing η (cf. equation (3.39).

However, for very high values of η, the evaporation rate and thus also the cooling rate becomes very small. If the evaporation rate becomes smaller than the inverse storage time of the particles in the trap, the process becomes inefficient with respect to the increase of the phase space density.

For alkali atoms, the main loss process limiting the storage time is collisions with hot background atoms. This explains the great importance of the vacuum in the trapping chamber. A longer storage time makes it possible to evaporate much more efficient and reach quantum degeneracy with worse starting conditions.

Obviously, a too small value of η will also lead to failure. In this case the density of the atoms will drop faster than can be compensated for (regarding the phase space density) by the temperature. So the right choice for η has to be in an intermediate regime and depends on the storage time in the trap and also on the rethermalization time τ_{rt}.

The rethermalization time τ_{rt} defines the overall length of the evaporation process at a given η. If the Boltzmann distribution is truncated at ηkT, it takes τ_{rt} until the energy distribution of the atoms is again Boltzmann like. Before the atoms reach this distribution, it is not efficient to lower the energy threshold further.

If the atoms thermalize faster at a given value for η, the energy threshold E_{thr} can be lowered faster, and the cooling proceeds faster. Since the total time that can be used for the evaporation, is on the order of the storage time, this means that for faster thermalization higher values for η can be used, leading to more efficient cooling.

As mentioned above, thermalization in the trapped gas is induced by elastic collisions. The rate of elastic collisions $1/\tau_{\mathrm{el}}$, which is directly proportional to the rethermalization rate [104], depends on the density and temperature of the trapped cloud as

$$1/\tau_{\mathrm{el}} = n v_{\mathrm{av}} \sigma. \tag{3.41}$$

Here v_{av} is the average velocity between atoms and is proportional to $T^{1/2}$.

The cross section is determined by the s-wave scattering length of the atomic species, which explains not only the importance of this parameter for the properties of the BEC itself as discussed in section 2.1.2, but also for the cooling process. The density is the parameter that can be influenced most directly in an experiment. Equation (3.41) shows, why a high density is so crucial for evaporative cooling.

In practice, the collision rate is the decisive parameter for choosing values for η during an evaporation. While it is theoretically possible to reach BEC with a dropping collision rate during the evaporation, success is usually only guaranteed, if the collision rate rises during the cooling process [103]. In this regime the cooling process is called *run-away evaporation.*

3.5.2 Experimental results

In order to realize the outlined evaporation scheme, the trapping potential has to be cut at some specified height. This is implemented in the experiment using a radio frequency technique.

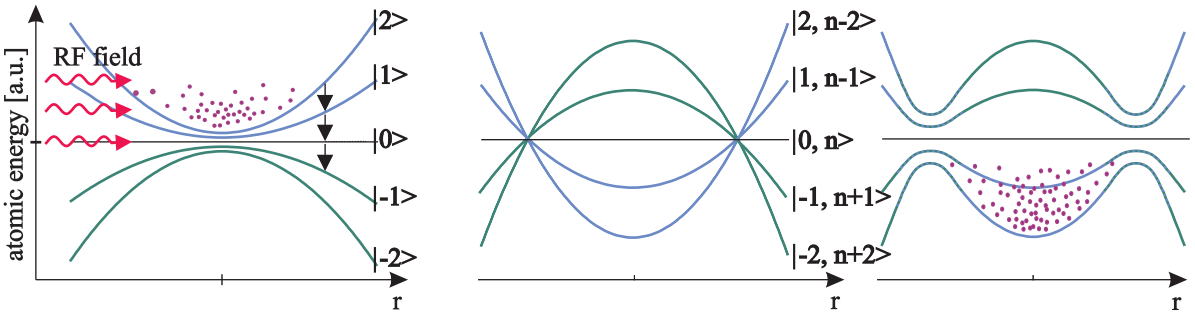

Figure 3.28: Truncating the magnetic trap with radio frequencies. Left image: Resonance condition for the RF field on the magentic trap. Middle image: Dressed atom eigenvalues without impinging RF field. Right image: Dressed atom eigenvalues with the RF power switched on. The RF field deforms the bare energy eigenvalues.

Due to the magnetic field of the trap, the m_F substates of the $F = 2$ ground state of ^{87}Rb are split by 700 kHz/G. If a RF field impinges onto atoms resonant with the splitting between the m_F states, the atoms can change their m_F state. Usually, the applied RF field is so strong, that it can not be treated any more as a small perturbation, which would induce transitions between neighboring m_F states and lead to populations on all m_F states. Instead one has to apply a dressed state picture, which results from diagonalizing the complete Hamiltonian of atomic energies and radiation field. Away from the resonance condition, the eigenstates of this Hamiltonian correspond to the bare states without the radio frequency, as shown in figure 3.28. However, in the transition region around resonance the state corresponding asymptotically to $|2, 2\rangle$ in the inner region is connected continuously to the state $|2, -2\rangle$ in the outer regions.

Thus atoms, which move through a magnetic field corresponding to the resonance condition change their state adiabatically from $|2, 2\rangle$ to $|2, -2\rangle$. Because the latter is an anti-binding state, these atoms are expelled from the trapping region. Since only atoms of sufficient energy will reach the positions where the RF field is resonant, this method effectively cuts the trapping potential at this magnetic field. Atoms with lower energy stay trapped, while high energy atoms crossing this position are expelled. The truncated trap depth is proportional to the applied radio frequency, and can therefore be lowered externally by changing the frequency of the RF.

From a technical view, the used frequencies are between 0 MHz and 10 MHz. For the lower frequency range, an absolute precision of 25 kHz is necessary. Furthermore, it is necessary to change the frequency ramp of the evaporation cycle in a flexible way. The radio frequency setup shown in figure 3.29 meets these requirements. Our RF source is a frequency generator (Agilent 33250A), operated in FM mode. In this mode, the frequency of the radio frequency is proportional to an externally applied voltage, which is provided by another frequency generator (Agilent 33120A), used as a wave form generator. This solution has the advantage that all signals are produced outside of the noisy environment of a computer system. The waveform of the generator is programmed by the computer via a GPIB connection (*General Purpose Interface Bus*, sometimes also referred to as IEEE

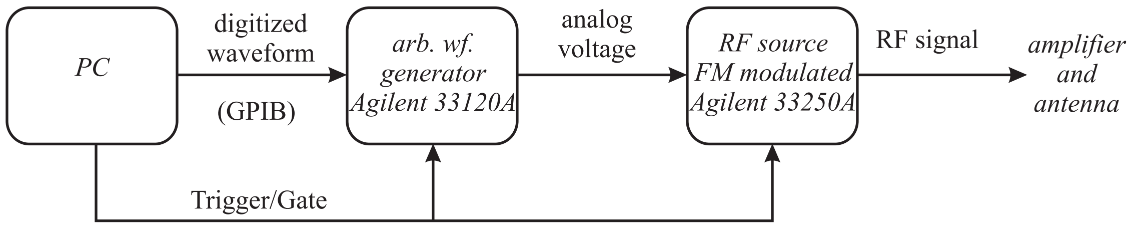

Figure 3.29: RF system for the evaporative cooling. A personal computer is used as the central control unit. The shape of the radio frequency has been stored in the arbitrary waveform generator before the experimental sequence begins and is started by a trigger signal from the PC.

488 protocol). The waveform is transmitted to the generator in a digitalized form, i. e. free of analog noise and prior to the experimental sequence. The waveform and thus the RF is triggered by the computer.

If the RF is not used, it is switched off by a PIN diode attenuator (Mini-Circuits ZSWHA-1-20, 60 dB suppression) in series with a mechanical relais. During the evaporation, the relais is switched and the attenuator gated. The radio frequency is then amplified in a homebuild amplifier based on the wideband linear amplifier chip CA2832C (Motorola) to 38 dB. Two windings of copper wire around the vacuum glass cell suffice as antenna.

We thus have a radio frequency setup, that allows us to change the energy cut-off parameter η at will. The primary task in choosing a shape of the frequency ramp, which is equivalent to choosing a function $\eta(t)$, is to reach the runaway evaporation regime.

We accomplished this objective by constructing the evaporation ramp out of individually optimized 5 s long linear ramps. The final ramp had a duration of 126.5 s. For each segment, the end point of the last segment was used as starting frequency. The next stop frequency was chosen such that the optical peak density of a subsequent absorption picture was maximized. Since the peak optical density as well as the collision rate scale as $n(\rho = 0)T^{\frac{1}{2}}$, they are proportional to each other. However, the optical peak density offers the advantage that just one absorption image is sufficient for its determination. A direct measurement of the collision rate on the other hand would require recording a complete time of flight series.

For the chosen endpoint, a complete temperature and atom number measurement was performed. The results are shown in figure 3.30. We attribute the occasional bumps in the frequency curve to variations of the initial conditions, leading to small variations of the optimal choice of the next frequency point.

The evaporation was in the runaway regime, as we could verify by the slow increase of the optical peak density from a value of 1.88 to about 3 during the measurement, and also later by calculating the actual collision rates. The value of η was initially at about 4 and shifted gradually to larger values of 6-8 at the end of the sequence. This is also consistent with the achievement of runaway evaporation.

Since the temperature could be measured with the smallest error of all observable quantities it was also used — in combination with the known trap frequencies — to calculate the

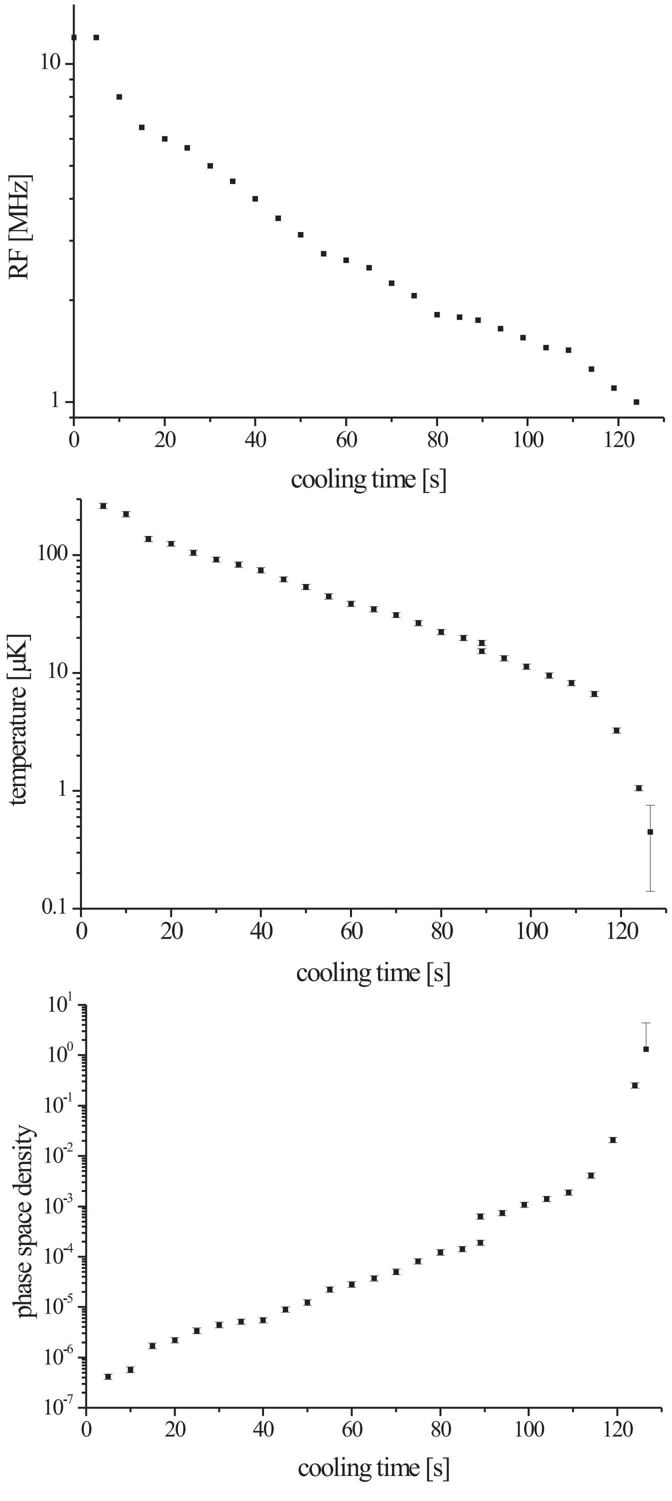

Figure 3.30: Evaporative Cooling. Upper figure: Applied radio frequency. Middle figure: Temperature during the evaporation. Lower figure: Phase space density during the evaporation. For details see the text.

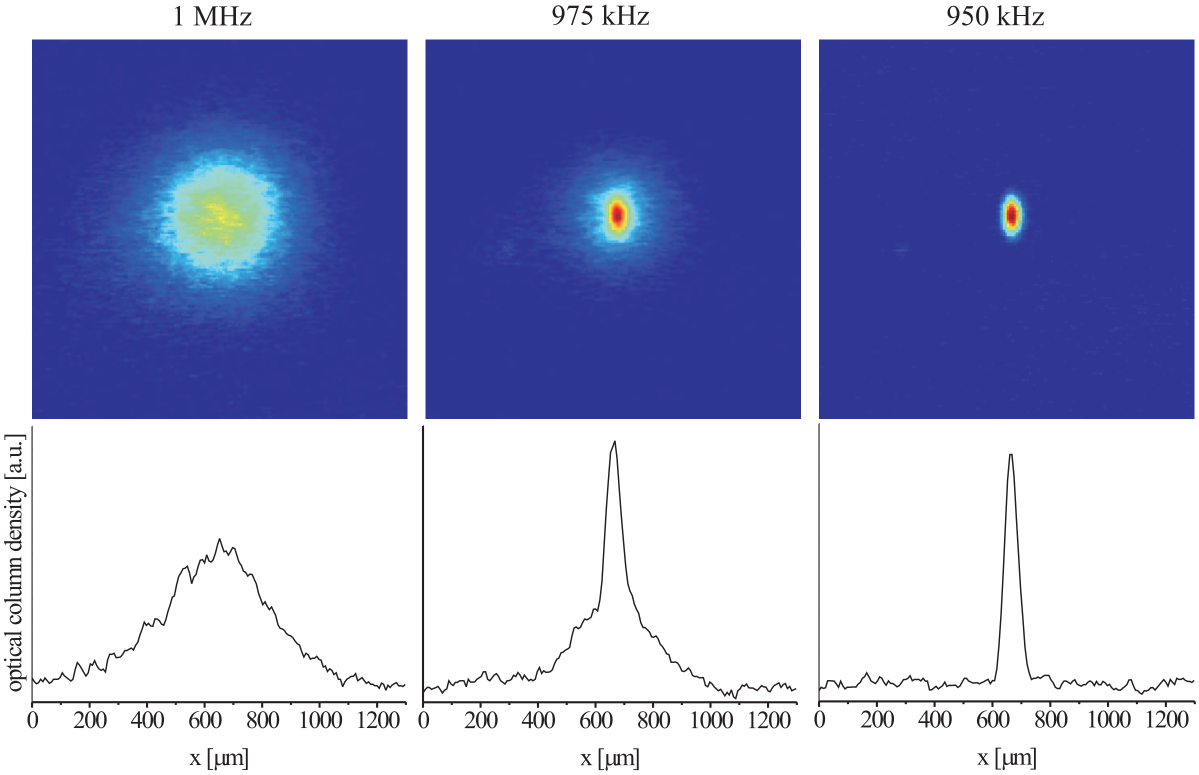

Figure 3.31: Thermal cloud, partially condensed cloud and pure BEC. Above the pictures is the final radio frequency used in the corresponding evaporation ramp. A final frequency of 1 MHz leads to an isotropic thermal cloud of approximately 500 nK, a final frequency of 975 kHz to a condensate with a visible thermal background and a final frequency of 950 kHz to a nearly pure condensate fraction. All images use the same color encoding and are taken after 24 ms time of flight, corresponding to a drop of 3 mm. In the lower row, cuts through the absorption profiles are plotted.

size of the clouds. For higher temperatures, a fit of the cloud shape was in agreement with the cloud sizes determined via the temperature and trap frequencies. For lower temperatures, the clouds become so small, that a direct determination is not possible any more due to the resolution limit of our imaging system.

Together with the atom number, which was also extracted from the absorption pictures, the density and the phase space density can be determined, as plotted in figure 3.30.

The whole measurement took about 30 hours and was performed over two days. The first measurement period went up to 89 s evaporation time. This explains the discontinuity at that time; at the second day starting conditions were slightly better, leading to the noticeable offset in the phase space density curve.

I would like to stress the usefulness of this method of stepwise optimization of the the optical peak density. Apart from providing a guide for designing the frequency ramp, it was also invaluable to know during the long measurement, that we were still in the runaway regime.

The last point of the frequency ramp was not chosen by the criterion of maximized optical density, but rather by testing for the emergence of the BEC. As can be seen in the sequence displayed in figure 3.31, differences as small as 25 kHz at the end of the ramp change the character of the atomic cloud completely. The critical temperature for the shown atomic cloud was approximately 300 nK and the condensate consisted of 10^5 atoms.

Compared to similar experiments, our starting conditions for evaporation are significantly worse than usually reported. However, the size of the realized condensate is quite comparable to other experiments using a similar setup. This already indicates, that our evaporation process is very efficient in terms of atom loss. Due to our long storage times, we can afford to apply a very long evaporation sequence. In fact, our sequence is about four times longer than standard sequences used in other experiments.

3.6 Conclusions

In this section I have described our scheme to produce Bose-Einstein condensates of ^{87}Rb. The main processes, i. e. precooling in magneto-optical traps, transferring into a magnetic trap, storing in these traps and evaporative cooling are documented in detail. Key technical components as the laser system, vacuum system and the imaging system are characterized. The imaging system is found to work close to the shot noise limit. Critical control points to monitor the performance of the BEC creation process are the atom number in the lower MOT and the quadrupole trap.

I would like to emphasize a few key points regarding the described methods. Although all mentioned steps are important, I have learned — sometimes the hard way — during the construction of the experiment, that some parts of the experiment are more crucial than the rest.

From a hardware perspective, among several parts such as the RF system, laser system, control system, current power supplies etc, the most critical ones are the vacuum system and the QUIC setup.

To the frustration of all participating experimenters, we experienced how the whole experiment can be set back by one year, if the vacuum system is simply not good enough to provide long storage times. On the other hand, the excellent vacuum we achieved in a new setup allowed us to optimize the evaporation process and overcompensate other shortcomings in the system. Given the enormous effort necessary to reinstall a new vacuum system, the quality of the vacuum should be optimized consequently and tested by storage time measurements as early as possible.

Similar considerations hold for the design of the magnetic trap. Since a change of the magnetic trap system also requires a long design and optimization period, the parameters of such a system have to be chosen and characterized with care. The too shallow trap potential experienced by the atoms during the transport is the weakest point within the experiment. With an optimized coil system it will be possible to transfer nearly one order of magnitude more atoms into that trap. This will ease the efforts to reach quantum degeneracy considerably.

In this context, also the low transfer efficiency of atoms from the first to the second MOT has to be considered as a weak point within the experiment. By further optimization, it should be possible to increase significantly the number of atoms caught in the lower MOT.

Strong points in the implementation of this BEC system are the excellent vacuum, allowing for long storage times in the magnetic trap, the efficiency of the evaporative cooling stage, and the established monitoring system for the most important external parameters such as laser powers, magnetic fields and timings.

All techniques described in this chapter are not difficult to implement for themselves. The overall complexity of the experiment stems from the requirement to combine the separate stages efficiently and reliably. The implementation of a working system to reach quantum degeneracy is thus an important milestone towards our goal to study the interaction of ultracold Cesium-Rubidium mixtures.

Chapter 4

Characterization of the BEC

After the characterization of the experimental routine to obtain a Bose-Einstein Condensation, in this chapter the condensate itself is examined. The various properties of the cloud have some interdependence, which allows consistency checks of the different measured parameters.

4.1 Experimental parameters and methods

In the first part of this chapter I summarize the relevant parameters describing our condensate. The experimental methods to investigate these properties are closely related to the methods covered in the last chapter.

4.1.1 BEC figures of interest

The properties of an atomic cloud below the critical temperature are governed by parameters that remain constant during several experiments and such that vary from experiment to experiment. Fixed parameters are the s-wave scattering length a_s and the trap frequencies ω_ρ and ω_z of the magnetic trap. The number of atoms in the condensate N_0 and in the thermal cloud N_{th}, and the temperature T of the cloud can change significantly for different experiments. The transition temperature T_c, the chemical potential μ and the mean field energy E_{mf} depend on the total number of atoms and the temperature.

The s-wave scattering length of ^{87}Rb is known from the literature [53] with sufficient accuracy. The trap frequencies can be determined using equations (3.36) and (3.37), which relate the frequencies to the characteristics of the magnetic field. The gradient ζ of the quadrupole field, the strength of the dipole moment p and its distance z_p from the position of the quadrupole trap can be inferred directly from measurements with a magnetic probe. This was performed in [50], resulting in the values

$$\begin{aligned}\zeta/I_{\text{coil}} &= (6.27 \pm 0.02)\ \text{G cm}^{-1}\ \text{A}^{-1} && (4.1)\\ p/I_{\text{coil}} &= (28.2 \pm 0.3)\ \text{G cm}^{3}\ \text{A}^{-1} && (4.2)\\ z_p &= (30.48 \pm 0.08)\ \text{mm}. && (4.3)\end{aligned}$$

The values for ζ and p have to be multiplied with the current I_{coil} through the coil system to recover the values valid in the experiments. For the current of 25.6 A we used during the BEC experiments, this yields for the axial trap frequency

$$\omega_z = 2\pi \cdot (21.47 \pm 0.06)\ \text{Hz}. \tag{4.4}$$

The determination of the radial oscillation frequency requires the knowledge of the offset field B_0, which results from the nearly complete cancellation of the quadrupole field by the field due to the Ioffe coil. Since both these fields are much larger than B_0 at the position of the QUIC trap, a determination of B_0 using the values of equations (4.1) to (4.3) leads to a large relative error of B_0. A more direct method is to measure B_0 directly by lowering the final radio frequency of the evaporative cooling sequence, until all atoms are removed from the trap. Since the spatial extensions of the BEC are very small, the atoms sample the magnetic field to a good approximation only at its lowest value. Thus the atoms are only removed for radio frequencies very close to the frequency corresponding to the offset field. We measured this frequency to be (910 ± 10) kHz. This corresponds to a magnetic offset field of $B_0 = (1.300 \pm 0.014)$ G. Using this value and the expression in equation (3.37), we obtain thus

$$\omega_\rho = 2\pi \cdot (271.7 \pm 2.2)\ \text{Hz}. \tag{4.5}$$

The combination of these fixed parameters with measured values of the cloud, as e. g. the number of atoms in the thermal component and the condensate fraction and the temperature, allows to deduce further properties of the cloud as the critical temperature T_c and the mean field energy E_{mf} of the trapped condensate. A comparison of the mean field energy with the other energy scales of the cloud allows to review the validity of the Thomas-Fermi approximation as discussed in section 2.1.2. Within the Thomas-Fermi approximation, knowledge of the atom number N_0 in the condensed fraction can be used to determine the chemical potential μ of the cloud and the density distribution in the trap $n(\vec{r})$.

The density distribution according to the Thomas-Fermi approximation is given in equation (2.15) by $n(\vec{r}) = \mu/U_0 \max(1 - \rho^2/R_\rho^2 - z^2/R_z^2, 0)$, where the Thomas-Fermi radii are $R_\rho = \sqrt{2\mu/m\omega_\rho^2}$ and $R_z = \sqrt{2\mu/m\omega_z^2}$. Analytical expressions for the chemical potential μ and the Thomas-Fermi radii R_ρ and R_z can be obtained using the normalization condition

$\int dV\, n(\vec{r}) = N_0$ as

$$\mu = \frac{15^{2/5}}{2}\left(\hbar^4 a_s^2 m \omega_\rho^4 \omega_z^2 N_0^2\right)^{1/5} \tag{4.6}$$

$$R_\rho = 15^{1/5}\left(\frac{\hbar^2 a_s \omega_z N_0}{m^4 \omega_\rho^3}\right)^{1/5} \tag{4.7}$$

$$R_z = 15^{1/5}\left(\frac{\hbar^2 a_s \omega_\rho^2 N_0}{m^4 \omega_z^4}\right)^{1/5} \tag{4.8}$$

4.1.2 Experimental methods

Just as for clouds above the transition temperature, the most important quantities that can be extracted directly from the experimental data with the help of absorption pictures are the temperature and the number of atoms.

The total number of atoms can be extracted in the same way as for thermal clouds above the critical temperature. For partially condensed clouds, it is also of interest to determine the fraction of atoms belonging to the condensed component. This is accomplished within the data acquisition process by fitting the absorption pictures to appropriate theoretical profiles.

These profiles result from the sum of a Thomas-Fermi profile as defined in equation (2.15) and a term describing the thermal component of the gas. While a gas well above the transition temperature can be described very well with the classical Boltzmann distribution, the exact Bose distribution departs strongly from that for a gas below the transition temperature (cf. figure 2.1). Because of this the density n_{th} of a thermal cloud can not be fitted anymore with a Gaussian function, but with a so called *Bose enhanced Gaussian* [34]

$$n_{\mathrm{th}}(\vec{r}) = \frac{1}{\lambda_{\mathrm{dB}}^3} g_{3/2}\left(\exp\left(\frac{\mu - V(\vec{r})}{k_B T}\right)\right), \tag{4.9}$$

where $\lambda_{\mathrm{dB}} = \sqrt{2\pi\hbar^2/mk_BT}$ is the deBroglie wave length, $V(\vec{r})$ the harmonic trapping potential, μ the chemical potential and $g_{3/2} = \sum_{n=1}^{\infty} x^n/n^{3/2}$ a function of the class already introduced in context with the theory of Bose gases on page 6. For high temperatures (i. e. $T > T_c$), we have $V(\vec{r}) - \mu \gg k_B T$, so the the exponential argument of the $g_{3/2}$ function becomes very small. Then only the first term in the series defining $g_{3/2}$ contributes and one recovers a Gaussian profile again, in agreement with the fitting functions used in the last chapter.

The whole ansatz of the profile being the sum of these two parts relies on the proposition that the two components coexist and do not mutually influence their density distributions. This assumption is affirmed by the good resulting description of the experimental data. The functions used for the fit routine are the projections of the theoretical distributions, because absorption images only show the column density of a density distribution along the imaging beam direction. The necessary integration can be performed for both the

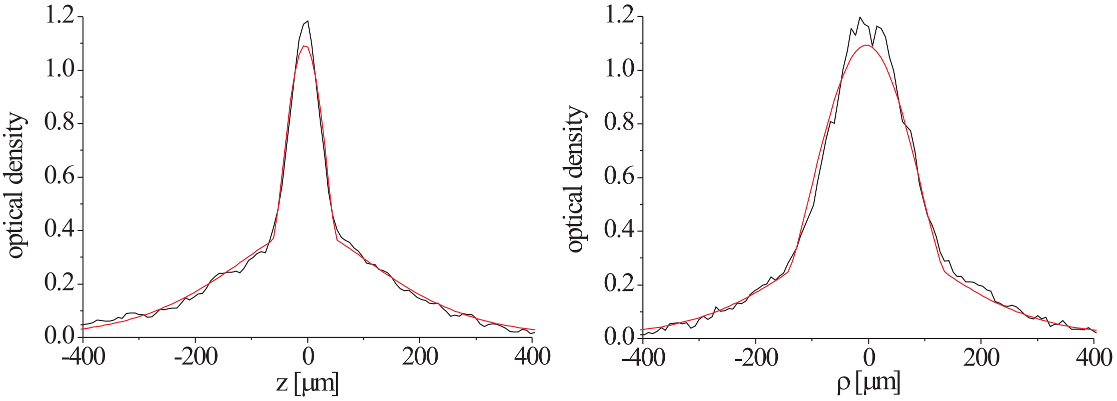

Figure 4.1: Fitted profiles for a partially condensed atomic cloud. The profiles were obtained by the absorption imaging technique and the profiles are fitted according to equation (4.10). The imaged cloud expanded freely for 18 ms before the absorption image was taken.

thermal and the condensed component analytically. The used fitting function n_c for the measured column density is thus

$$\begin{aligned} n_\mathrm{c}(\rho, z) = n_{\mathrm{TF},0} &\left(\max\left(1 - \frac{(\rho-\rho_0)^2}{w_{\mathrm{TF},\rho}^2} - \frac{(z-z_0)^2}{w_{\mathrm{TF},z}^2},\, 0\right)\right)^{3/2} \\ + n_{\mathrm{th},0}\, g_2 &\left(\exp\left(-\frac{2\,(\rho-\rho_0)^2}{w_{\mathrm{th},\rho}^2} - \frac{2\,(z-z_0)^2}{w_{\mathrm{th},z}^2}\right)\right) + b. \end{aligned} \tag{4.10}$$

Here, $n_{\mathrm{TF},0}$ ($n_{\mathrm{th},0}$) is the measured peak optical density due to the condensed (thermal) component, $w_{\mathrm{TF},\rho}$ and $w_{\mathrm{TF},z}$ ($w_{\mathrm{th},\rho}$ and $w_{\mathrm{th},z}$) are the Thomas-Fermi radii of the condensed part (the $1/e^2$ radii of the thermal component), ρ_0 and z_0 denote the center of the cloud and b is a uniform background (which should be close to 0 for a reliable image). An example of an absorption image fitted with this function is shown in figure 4.1.

The number of atoms in each component can be given analytically in terms of the fit parameters. For an absorption image the number of atoms of the condensed part is given by

$$N_0 = \frac{2\pi n_{\mathrm{TF},0}}{5} \frac{w_{\mathrm{TF},\rho} w_{\mathrm{TF},z}}{\sigma} \tag{4.11}$$

and the atom number of the thermal component by

$$N_\mathrm{th} = \frac{\pi g_3\,(1)\, n_{\mathrm{th},0}}{2} \frac{w_{\mathrm{th},\rho} w_{\mathrm{th},z}}{\sigma} \approx 1.89\; n_{\mathrm{th},0} \frac{w_{\mathrm{th},\rho} w_{\mathrm{th},z}}{\sigma}. \tag{4.12}$$

Here σ is the absorption cross section.

The temperature of the atomic cloud can be inferred from the expansion of the thermal cloud in time of flight measurements. Since the the size of the trapped cloud is very small and expansion times are longer than those applicable for higher temperature clouds, the influence of the trapping potential is negligible and also the absolute values of the two fitted widths must coincide within their errors.

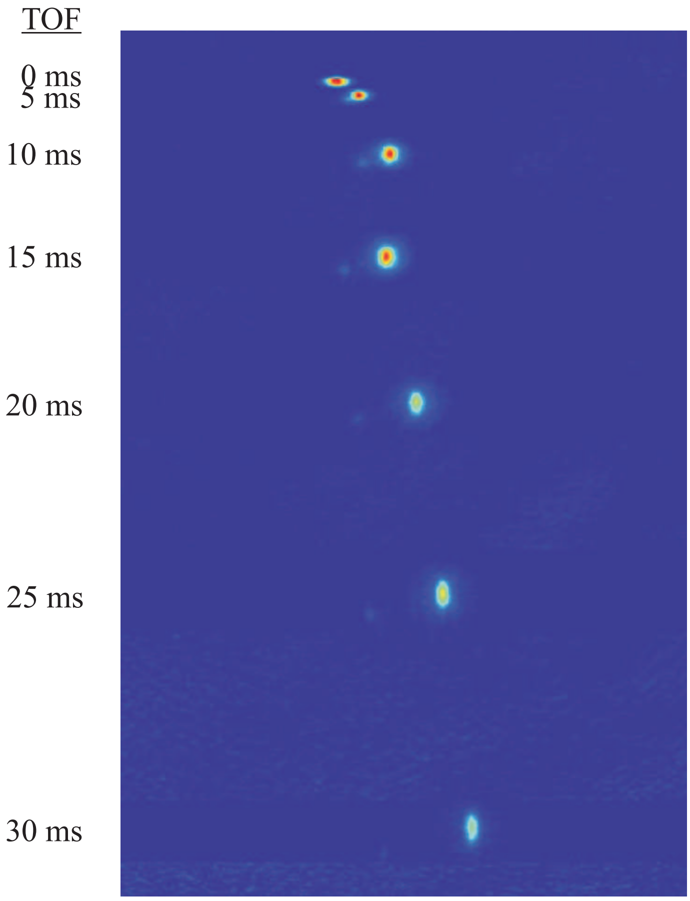

Figure 4.2: Free expansion of a BEC. Each cloud was imaged separately with the absorption imaging technique. Images were taken every 5 ms. In 30 ms, the cloud fell about 4.4 mm. The horizontal velocity component of the clouds, as well as the faint signal to the left of some of the clouds, stem from a Stern-Gerlach type force acting on the atoms while the magnetic fields are switched off. Details for this effect are discussed in the next section.

4.2 Measured BEC properties

While the increase of the thermal cloud width can be used to measure the temperature of the cloud, the change of the Thomas-Fermi radii allows to determine the mean field energy of the condensate. This is examined in section 4.2.1. Comparing the fraction of condensed to non-condensed atoms in section 4.2.2 yields another possibility to check the consistency of the used methods. In the last part of this chapter, a Stern-Gerlach like spatial splitting of multiple condensates of different magnetic spin is discussed.

4.2.1 Reversal of the aspect ratio and mean field energy

The expansion of the condensed component of the cloud is independent of the cloud's temperature, since the atoms are always in their motional ground state. The expansion is governed by repulsive forces between the atoms due to the mean field energy of the condensate.

A quantitative description can be obtained by solving the time dependant Gross-Pitaevskij equation (cf. equations (2.13) and (2.14)). A time of flight measurement can be described with these equations by using a time dependant trapping potential, which is switched off at $t = 0$. In [105], the resulting differential equation was solved by an expansion in terms of even powers of the trapping frequency ratio ω_z/ω_ρ. Since in our case $\omega_z/\omega_\rho = 0.079$, it suffices to consider only the first two terms of the series and drop further terms of order $(\omega_z/\omega_\rho)^4$ or higher.

This formalism predicts that the condensate keeps — within the Thomas-Fermi approximation — its paraboloid shape with rescaled radii during the free expansion. The time dependant Thomas-Fermi radii $R(t)$ are given by [105, 34]:

$$\begin{aligned} R_\rho(t) &= R_\rho(0)\sqrt{1+(\omega_\rho t)^2} && (4.13)\\ R_z(t) &= R_z(0)\left(1+\left(\frac{\omega_z}{\omega_\rho}\right)^2\left(\omega_\rho t\arctan(\omega_\rho t)-\frac{1}{2}\ln\left(1+(\omega_\rho t)^2\right)\right)\right). && (4.14)\end{aligned}$$

Figure 4.2 shows a series of freely expanding clouds. The different scaling of the cloud radii is clearly visible. The resulting change of the aspect ratio is a clear signature of Bose-Einstein condensation. The physical explanation for the inversion of the aspect ratio is due to the repulsion of the atoms. Because of the anisotropy of the trapping potential, the trapping forces are stronger along the radial direction. These forces are counterbalanced by the repulsive atom–atom interaction, giving rise to the mean field energy of the cloud. When the trapping potential is switched off instantaneously, these repulsive forces expand the cloud. The expansion is faster in the radial direction because of the larger gradient of the mean field energy along this direction.

For a quantitative analysis, the Thomas-Fermi radii $R_\rho(t)$ and $R_z(t)$ are plotted versus the expansion time in figure 4.3. The plotted radii are corrected for the imaging system resolution of 22 μm ±3 μm.

The average number of atoms in the measurement was $6.4 \cdot 10^4 \pm 1.1 \cdot 10^4$ atoms as determined from the absorption images. According to equations (4.6) to (4.8), this yields a chemical potential of $\mu = k_B \cdot (134 \pm 26)$ nK, where the major part of the error stems from the uncertainty in the number of atoms. The Thomas-Fermi radii are $R_\rho = (3.0 \pm 0.3)$ μm and $R_z = (38 \pm 4)$ μm. The plotted curve in figure 4.3 is the theoretical prediction along equations (4.13) and (4.14), using these values for the Thomas-Fermi radii. The curve describes the data very well, considering that there are no free fit parameters in the model.

Alternatively, using the initial radii as fitting parameters, one obtains $R_\rho = (2.80 \pm 0.08$ μm

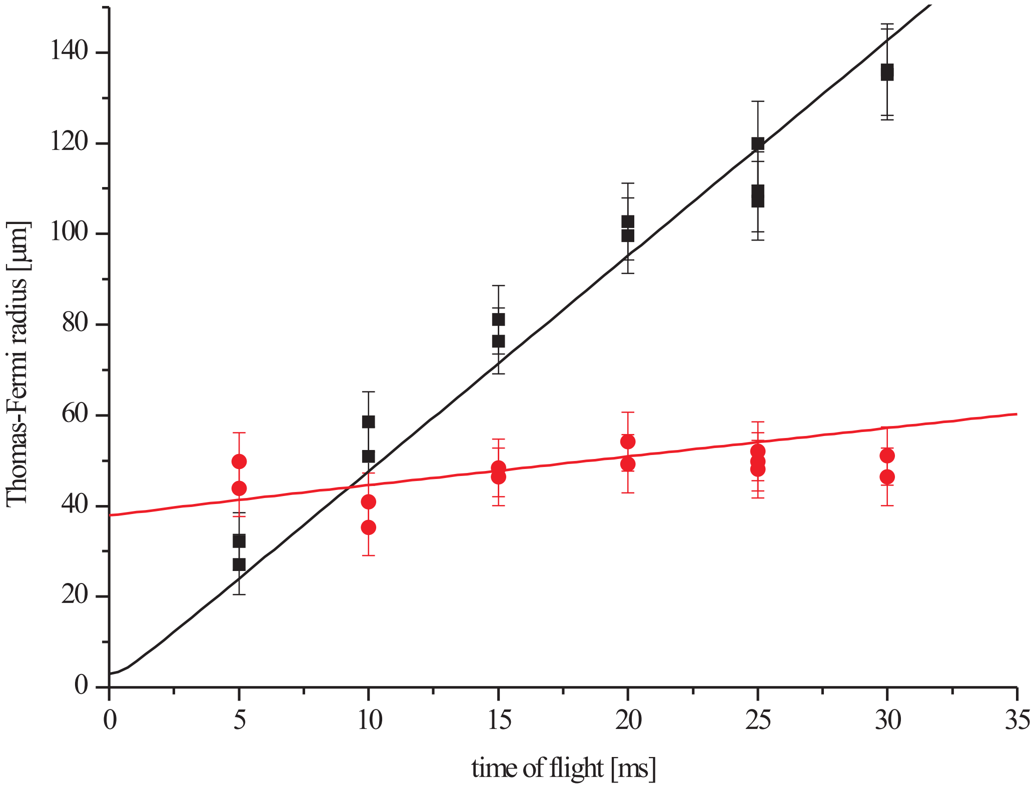

Figure 4.3: Thomas-Fermi radii of a freely expanding BEC. The black data is the radius in radial direction R_ρ and the red data the radius in axial direction R_z. The curves are according to equations (4.13) and (4.14), without any free fitting parameters. For details see the text.

and $R_\rho = 36 \pm 2$ μm. This is in agreement with the radii calculated from the Thomas-Fermi approximation for the atom number detected in the condensates. Also the resulting ratio R_z/R_ρ of the fitted initial radii of 12.9 ± 0.8 agrees very well with the theoretical value of 12.6 ± 0.4, which can be determined directly from the trap frequencies.

This good compliance with predictions based on the Thomas-Fermi approximation shows the validity of this approach.

Note, that the above measurement can also be used to estimate directly the mean field energy in the trapped condensate. From figure 4.3 it is evident, that nearly all kinetic energy remaining in the expanding BEC is contained in the radial direction.

Neglecting the initial kinetic energy of the condensate, the kinetic energy of the expanding condensate stems only from the mean field energy E_{mf} of the BEC. This leads to the expression

$$E_{\mathrm{mf}} \approx \frac{1}{2} m \left(R_\rho(0)\omega_\rho\right)^2 . \tag{4.15}$$

Here m is the atomic mass of Rubidium. This expression yields a value of about 110 nK. This has to be compared with the kinetic energy of the trapped sample neglected above, which will be on the order of the ground state energy of the interaction free ground state,

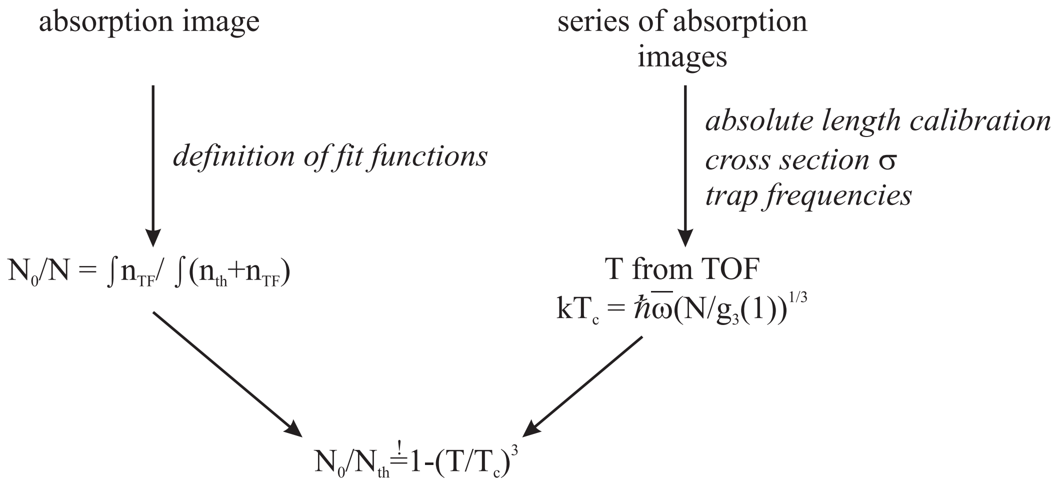

Figure 4.4: Consistency check based on a measurement of $N_0/(N_0+N_{\text{th}})$ and T/T_c. The diagram shows the basic figures used for the consistency check and the parameters and assumptions required to determine them experimentally (italic). For details see the text.

i. e. 6 nK. This confirms again the validity of the Thomas-Fermi approach.

4.2.2 Atom number and critical temperature

The relation $N_0/N = 1-(T/T_c)^3$ (equation (2.8)) can be used to perform a consistency check on the most important parameters and assumptions entering the data analysis of the experiment. As illustrated in figure 4.4, the two sides of the equation can both be determined from absorption images. The ratio $N_0/N = N_0/(N_0+N_{\text{th}})$ can be calculated using equations (4.11) and (4.12). For the other side of the equation, the temperature T can be determined with a TOF measurement, while the critical temperature is given by equation (2.5).

Figure 4.4 lists also the relevant parameters entering the calculations. Overall, the left side of the equation relies on the determination of a ratio, cancelling out all calibrations, while the right side depends on the the absolute determination of the two basic quantities T and N.

The corresponding measurement is shown in figure 4.5. The ratio N_0/N and the expression $(1-T/T_c)^3$ are obtained from the measured data as indicated in figure 4.4. The theoretically expected dependance according to equation (2.8) is also shown.

Within the error bars, the data follows the theoretical description, but is systematically below the prediction. An additional fit in red color is obtained using the model function

$$\frac{N_0}{N_0+N_{\text{th}}} = 1-\left(\alpha\frac{T}{T_c}\right)^3, \tag{4.16}$$

using α as a free fitting parameter. The fit yielded $\alpha = 1.02 \pm 0.01$. This indicates, that within a few percent our data processing yields consistent results. Note, that for the

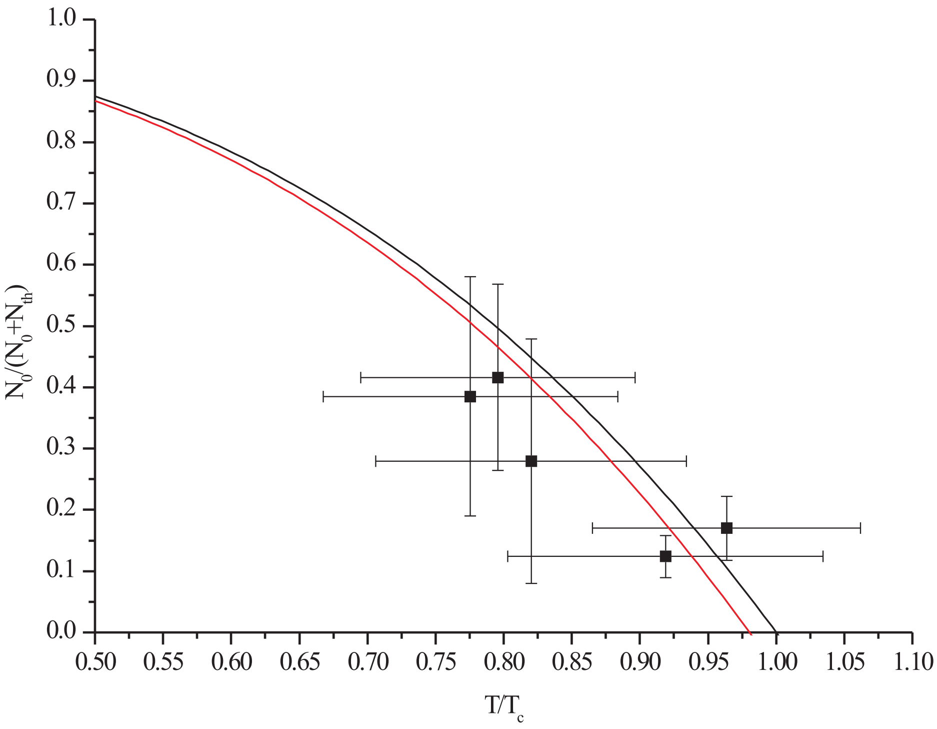

Figure 4.5: Fraction of condensed atoms versus T/T_c. The black line is the theoretical expectation according to equation (2.8) (no free fitting parameters). The red curve assumes a lower critical temperature than predicted by the simple theoretical model (see text).

analysis of the experimental raw data basically all models, imaging processing routines and quantitative values of our experiment have been used. Including the uncertainties of these figures leads to the large error bars of the data in figure 4.5.

A similar measurement was performed in [40]. By performing more measurements than here the statistical errors in that work were substantially lower than in figure 4.5. Just as in our measurement, the data points were shifted to the left, suggesting a smaller critical temperature T_c than predicted theoretically by the model of noninteracting Bosons. Due to the better statistics in [40], this was attributed to finite particle number effects and the interaction between the particles. Our results agree with this conclusion, but our statistical errors are to large to regard this measurement as an independent confirmation.

4.2.3 Multi component BECs

In image 4.2 a faint structure is visible next to the absorption signal of the condensate. These weak signals are due to further BECs in different m_F states. We attribute the emergence of these additional BECs to a transfer of the atoms into other m_F state when the magnetic field is rapidly switched off. The switching induces eddy currents in the coil holders, which show up in the pushing of the condensate away from the Ioffe coil, as can

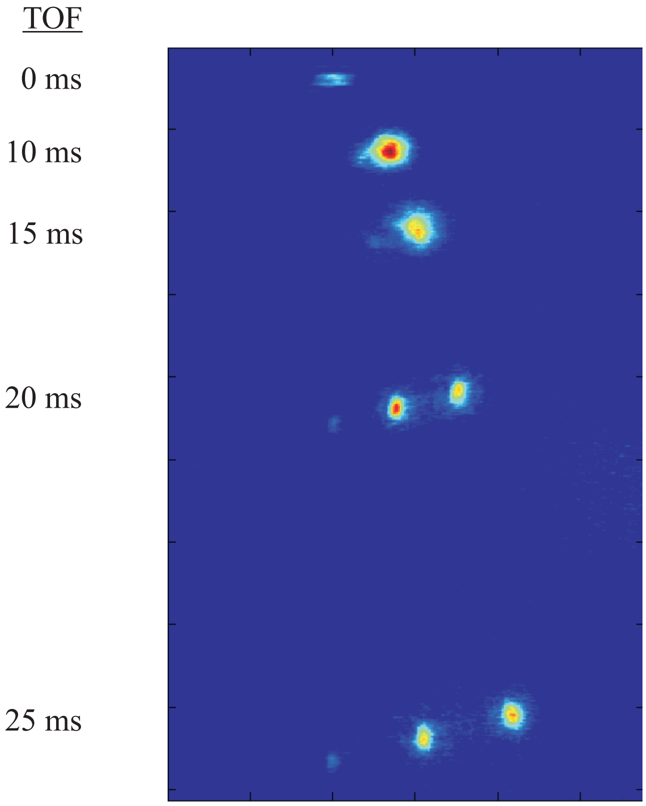

Figure 4.6: Stern-Gerlach detection of multi-component BECs. For details see the text.

also be seen nicely in image 4.2. If the eddy currents are scaled such that the magnetic field sweeps through 0 at the position of the QUIC trap, Majorana spin flips arise which possibly transfer a part of the atoms into different m_F states.

Supporting evidence for this explanation can be gained by changing the behavior of the switching of the fields. As expected, the population of the m_F states depends critically on the timing of the switching process. Turning the quadrupole and the Ioffe coil off with a small delay of a few 100 μs in between changes the distribution significantly. This behavior has been also observed in other BEC experiments [106]. In figure 4.6 the switching process was arranged to yield three condensates in the $m_F = 0, 1, 2$ states. Because of their different horizontal velocity, the components can be distinguished like in a Stern-Gerlach experiment. The existence of a condensate in the $m_F = 0$ is also a clear indication, that these additional m_F substates are only populated at the very end of the experimental sequence, since the $m_F = 0$ state is not stored in our magnetic trap.

The motional dynamics can be studied in figure 4.7. The clearest signature for the different magnetic dependance of the condensates stems from the motion in horizontal direction. All three trajectories exhibit uniform linear motions in this direction. This indicates that the condensates are accelerated only at the time of the switching process. The velocities v_{m_F} for the three sub states can be determined as $v_0 = (0.2\pm0.5)\ \mathrm{cm\,s^{-1}}$, $v_1 = (1.6\pm0.3)\ \mathrm{cm\,s^{-1}}$

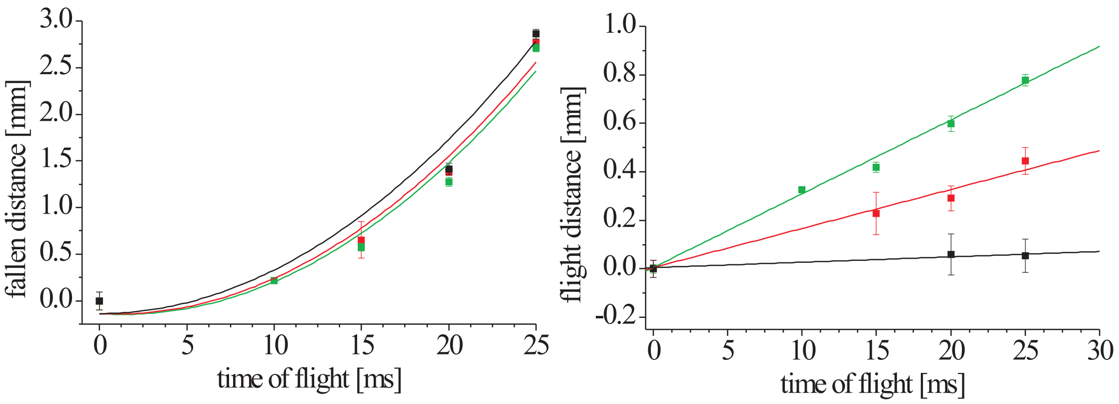

Figure 4.7: Vertical and horizontal movement of BECs in different m_F states. The position of the condensates in figure 4.6 is plotted versus the time of flight. Left image: Vertical position of the condensates. Right image: Horizontal position of the condensate. Data for the condensate in the $m_F = 2$, $m_F = 1$ and $m_F = 0$ condensate are in green, red and black color respectively.

and $v_2 = (3.0 \pm 0.2)$ cm s^{-1}. Since the magnetic moment of the condensate is proportional to their m_F quantum number, these velocities are consistent with the Stern-Gerlach effect.

The vertical motion is described with parabolical fits. Within the error bars, all data sets can be described with the same acceleration, but with different initial velocities in the upward direction. These velocities are all below 1 mm s^{-1} and can again be ascribed to a magnetic Stern-Gerlach force. The fit for $m_F = 0$ is used to calibrate the length scale, since no magnetic force is expected to act on atoms in this state.

4.3 Conclusions

In this chapter I have presented measurements with BECs created in our setup. Typical features of a Bose condensed gas as the bimodal density distribution and the inversion of the aspect ratio of the cloud could clearly be observed.

Furthermore several consistency checks could be performed, on the basis of a detailed analysis of the experimental data. The good agreement of the measurements show on the one hand, that the corresponding experiments are well understood. On the other hand, it also proves the very good reproducability of the results. This can also be observed directly during the measurements. Given the same initial parameters — as the number of atoms in the lower MOT, correct laser detunings and powers etc. — at the beginning of an experimental run, more than 90% of the experiments aimed to produce a BEC succeeded and delivered also condensates with similar parameters (T_c, N etc.).

Mastering the techniques to produce a single species BEC is an obvious prerequisite for creating two species condensates. The next step is therefore to trap the two species simultaneously in traps. This is reported on in the next chapter.

Chapter 5

Combined trapping of two atomic species

I will present initial steps undertaken in our experiment to observe an interaction between ultracold Rubidium and Cesium atoms. First experiments have been performed both in a MOT and a magnetic trap.

5.1 Double species atomic traps

The most important properties of Cesium are summarized. The interaction between ultracold Rubidium and Cesium above the critical temperature, as well as related work of other groups is discussed. At the end of this section the technical implementation of the double species trap is described.

5.1.1 Important properties of ^{133}Cs

The realization of a Cesium BEC has been the objective of several groups for some time. Cesium can be cooled to very low temperatures by purely optical means due to its low photon recoil momentum (it is the heaviest of all stable alkali isotopes) and its internal structure [107]. The splitting of the $6S_{1/2}$ Cesium ground state is also the basis for the SI definition of the time unit, which adds further to the interest in its properties. Its optical properties are very similar to those of the other alkali atoms. A MOT can be operated close to the D_2 line, as already described for Rubidium. A level scheme with the cooling and repumping transitions is shown in figure 5.1.

However, at low temperatures the collisional properties of Cesium deviate strongly from the other alkali atoms' behavior. The scattering cross section for ground state collisions depends strongly on an external magnetic field. The underlying mechanism is a *Feshbach resonance* [27], which is illustrated in figure 5.2. A Feshbach resonance (named after H. Feshbach, who developed a scattering theory approach for nuclear reactions in the late

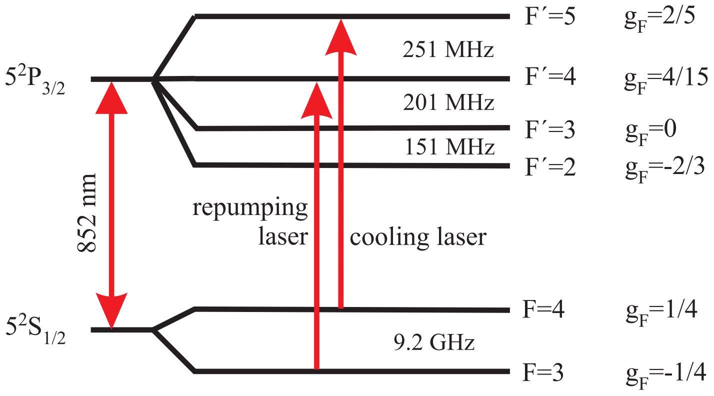

Figure 5.1: Level scheme of ^{133}Cs. The cooling transition and the repumper transition as used in the MOT are marked in red color. Note, that the energy scale indicated by the hyperfine splittings and the optical frequency are not to scale.

1950s) appears if the total energy of the colliding particles matches the energy of a molecular bound state in a closed collision channel (see figure 5.2). For an exact coincidence of the collision energy and the energy of the bound state (resonance) and in the case of a possible coupling between these states (e. g. by hyperfine interactions), the colliding particles scatter into that state with a high probability. This increases the scattering cross section. The energy of the bound state might be influenced by the Zeeman effect due to an external magnetic field. Therefore a magnetic field influences the collision properties strongly close to a Feshbach resonance, if the bound and the entrance state have different magnetic moments. In the case of the $F = 4$, $m_F = 4$ ground state of Cesium, such a resonance occurs at a zero magnetic field.

In the state $|4,4\rangle$, the scattering length is approximately 2400 Bohr radii. This results in a cross section three orders of magnitude larger than for Rubidium [54]. The elastic scattering rate exceeds the trap frequencies of common conservative atom traps. However, the thermalization rate is limited by the trap frequencies, so it saturates. Inelastic collisions, which lead to trap losses, do not saturate, such that the ratio of inelastic to elastic collisions is increased. This deteriorates the efficiency of the evaporation cooling stage.

To date, this collisional behavior has prevented the creation of a Cesium BEC in a magnetic trap [108]. A Cesium BEC was created in the group of R. Grimm in an optical dipole trap [109]. In this experiment, using an optical trap it was possible to change the elastic cross section with an external magnetic field without affecting the trapping mechanism.

5.1.2 Rubidium-Cesium interaction and related work

Rubidium-Cesium mixtures

The interaction of Rubidium and Cesium within a double condensate was already discussed in detail in chapter 2. All studies carried out so far in our experiments take place above the transition to BEC. The interaction between the different atomic species thus manifests

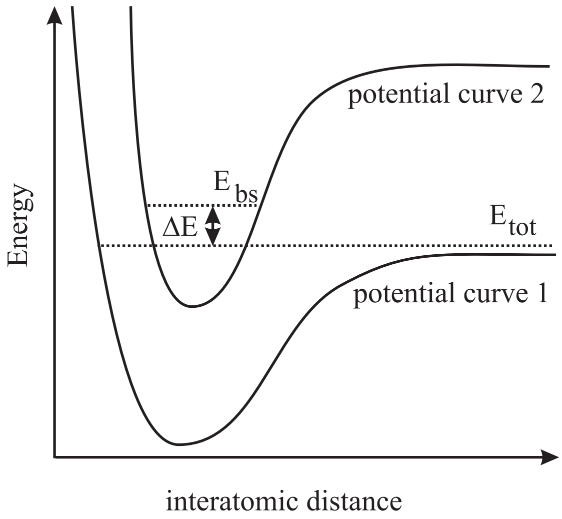

Figure 5.2: Feshbach resonance. The total energy of the two colliding particles is E_{tot}. The collision is governed by potential curve 1. Potential curve 2 is not accessible, since it is energetically forbidden initially (*closed entrance channel*). If the energy difference ΔE between a bound state of curve 2 and the collision energy vanishes, the particles scatter into this bound state and the scattering cross section is enhanced.

itself differently.

Just as for the single species case, the collisional behavior depends on whether near resonant light is present. The standard experiment to observe collisions influenced by light is storing the atoms in a MOT and studying the loading dynamics of the trapped gases. There have been three published experiments of this kind for a Rubidium-Cesium mixture [110, 111][1], which I will comment on in connection with our own measurements in section 5.2.

The properties of ground state collisions, that take place without the presence of resonant light, are decisive for the realization of sympathetic cooling. The molecular interaction potential during the scattering process is the molecular potential curve of the RbCs $X^1\Sigma_u$ state. This molecular potential has been studied by several groups. Nevertheless, it is not known well enough as to derive relevant quantities — as e. g. the interspecies s-wave scattering length — for ultracold collisions from it. The known information is summarized in appendix B.

The scattering process can be described best within a partial wave decomposition. At temperatures of about 100 μK, as typically encountered in a MOT, also higher partial waves than the s-wave contribution are important. S-wave scattering is supposed to become the dominant mechanism at temperatures below 50 μK, according to estimates based on the available knowledge of the interaction potential [112].

One method to observe ground state collisions in a conservative trap is to perform a thermalization measurement. The species are prepared at different temperatures and the thermalization towards an equilibrium temperature is observed. Since the thermalization is mediated by collisions, the collisional cross section can be determined by these measurements. Such a measurement for a RbCs mixture was performed in the group of E. Arimondo [112]. The experiments were carried out in a temperature regime where only s-wave scattering contributes. However, the obtained data in that experiment was only used to choose the best fit out of four theoretical curves. A more precise determination of the interspecies s-wave scattering length has not been performed till now.

---

[1] In [110], similar experiments by two different groups are described and compared with each other.

An alternative approach for determining the scattering cross section is to measure the molecular interaction potential with sufficient precision. This can be done via *photoassociation spectroscopy*. The colliding atoms are excited by a laser beam into a molecular bound state. The creation rate depends on the laser frequency and the molecular structure. From the obtained spectra, the molecular potential can be inferred with very high precision. Such a photoassociation was performed for a Rubidium-Cesium mixture in the group of D. deMille [113, 114]. However, the measurements of this group did explore only excited molecular potential curves so far. Thus the lowest molecular potential curve, which is the relevant one for ground state collisions, has not been measured with sufficient accuracy yet.

Other alkali mixtures

Because of the added technical efforts necessary for trapping a second atomic species, the number of active groups studying alkali mixtures is still comparably small. Interspecies Feshbach resonances have been studied by the groups of W. Ketterle (Sodium and Lithium) [29], D. Jin (Rubidium and Potassium) [28] and M. Inguscio (Rubidium and Potassium) [115].

The s-wave scattering length has been determined experimentally for a Lithium-Cesium mixture in the group of M. Weidemüller [116] and for a Rubidium-Potassium mixture in the group of M. Inguscio [117]. Both measurements were performed using a rethermalization technique. The latter group even succeeded in creating a two-species BEC by sympathetically cooling the Potassium atoms with the Rubidium atoms [47].

The fact, that nearly all of the cited work has been performed within the last three years indicates the growing interest in this field.

5.1.3 Technical implementation of a double species atomic trap

Like for Rubidium, the first step for trapping Cesium is to capture the atoms in a MOT. For the envisioned sympathetic cooling of Cesium with Rubidium the number of Rubidium has to be much larger than the number of Cesium atoms. Thus the number of Cesium atoms is not such a critical issue as the number of Rubidium atoms. Therefore it is not necessary to rebuild the entire double MOT system for Cesium. The Cesium atoms are trapped directly in a MOT located in the lower UHV part of the apparatus (cf. figure 3.1).

The necessary laser beams for the implementation of the MOT are superimposed onto the Rubidium laser beams with a dichroic mirror. The polarization optics, such as wave plates and polarizers, are designed to work at both wavelengths as well. The wave plates are custom made by the company Lens-Optics.

Three diode lasers are necessary for the operation of the Cesium MOT. As for Rubidium, these are diode lasers in Littrow configuration. All used lasers are homebuild. One laser is used as a reference laser and the other two provide the cooling laser light and the repumping laser light. The cooling laser is stabilized with a DAVLL scheme — just as the Rubidium lasers — whereas the reference and repumping lasers are stabilized with a polarization spectroscopy [118, 119]. In contrast to the Rubidium cooling laser, for the Cesium MOT a standard laser diode (SDL-5421-G1, JDS Uniphase) without additional amplification is used. All lasers are monitored using additional saturation spectroscopies; in addition to that, the frequency of the cooling laser is monitored by observing the beat signal between the reference laser and the cooling laser. The cooling laser was stabilized close to the $6S_{1/2}F = 4 \rightarrow 6P_{3/2}F' = 5$ transition and the repumping laser resonantly with the $6S_{1/2}F = 3 \rightarrow 6P_{3/2}F' = 4$ transition.

About 1.5 mW of the reference laser is used for probing the atoms in absorption measurements. Because of the mandatory short exposure time of this method, the laser beam is switched by passing it through an AOM. The imaging beam for the Cesium atoms is superimposed onto the Rubidium imaging beam. 300 μW of resonant light is available before the glass cell to probe the atoms.

The remaining part of the Cesium system is very similar to the Rubidium laser system described in section 3.1.2. The laser beams are sent through mechanical shutters and coupled into optical fibers. The whole setup is contained in a box to avoid stray light.

The source for the Cesium atoms is a reservoir connected with a valve to the lower UHV part of the apparatus (cf. figure 3.1). The flux of Cesium atoms can be controlled with this valve. For trapping a large number of Cesium atoms, the valve was opened such that the vacuum gauge changed its reading from the 10^{-11} mbar level into the 10^{-9} mbar range. After closing the valve again, the gauge display returns within four hours to its former value.

A pressure of 10^{-9} mbar is suitable for the experiments described in this thesis. For the envisioned realization of a Rubidium BEC with Cesium impurities or a double species condensate, this pressure is too high since the resulting storage time in the magnetic trap would be too short. For experiments requiring less or even single particles, one obvious solution is the reduction of the Cesium flux. As shown experimentally in [120] and subsequent work in our group, storing of few or single particles requires pressures between 10^{-10} mbar and 10^{-11} mbar.

Capturing a larger number of Cesium would not be directly compatible with the vacuum requirements of a BEC experiment. However, since the initial number of Cesium atoms can be chosen smaller than for Rubidium, this problem is not as severe as for Rubidium. It seems feasible to operate the vacuum system then with a nearly closed Cesium valve at a background gas pressure of 10^{-11} mbar and to temporarily enhance the number of trapped Cesium atoms by shining in UV light. Multiple experiments (e. g. [121, 122])

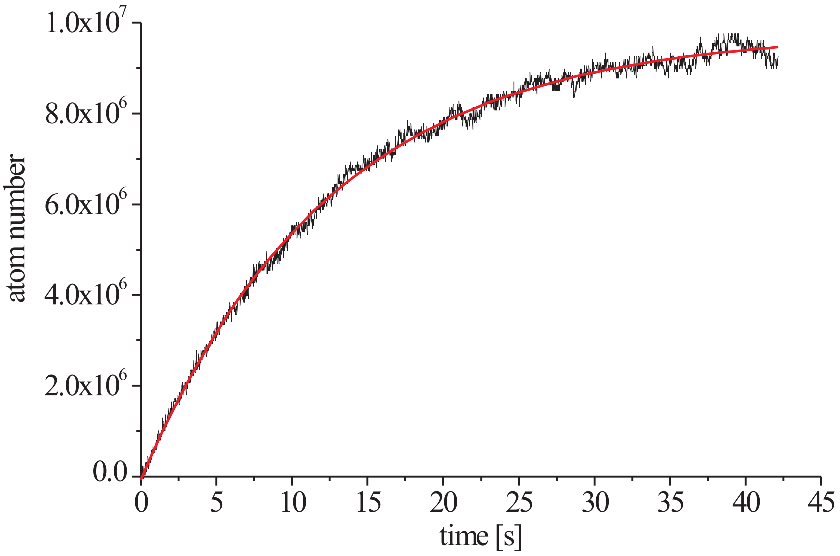

Figure 5.3: Loading curve of the Cesium MOT. The atom number is recorded by measuring the atomic fluorescence with a calibrated photo diode. The red curve is a fitted exponential function.

report on a rapid increase of the partial alkali vapor pressure with UV light illuminating the vacuum system. Under the influence of UV light, alkali atoms desorb from the surface of the vacuum system. After switching the light off again, the atoms stick to a wall and the pressure decreases within seconds.

5.2 Results for combined trapping in Magneto-Optical Traps

5.2.1 The Cesium MOT

A similar characterization as described above for the Rubidium MOT was conducted for the Cesium MOT. On average each Cesium MOT beam had about 2 mW of cooling laser light. The total repumping laser power was approximately 1 mW. In contrast to the alignment of the Rubidium MOT, the repumping laser beam is superimposed on all MOT beams. A detuning of 10 MHz (i.e. 1.9 linewidths) below the cooling transition was applied. This detuning is smaller than the one used for the Rubidium MOT and partially compensates the smaller power available as compared with the Rubidium MOT. The diameter of the Cesium MOT beams was about 1.5 cm, which is the same as the one used for the Rubidium MOT beams.

At a displayed background pressure of $2 \cdot 10^{-9}$ mbar, the Cesium MOT stores $1 \cdot 10^7$ atoms. A typical loading curve is plotted in figure 5.3. A remarkable feature of the curve is the long loading time of (12.5 ± 0.5) s. For a background pressure as measured by the vacuum gauge, the loading time should be comparable to the loading time of the

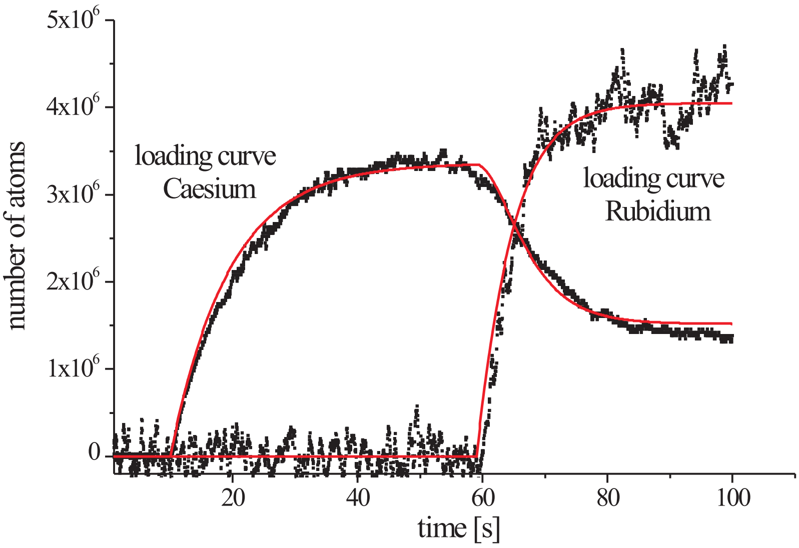

Figure 5.4: Simultaneous trapping of Rubidium and Cesium in a MOT. First only Cesium is loaded into the MOT. After 60 s Rubidium is loaded as well. The number of Cesium atoms decreases with an increasing number of Rubidium atoms.

upper Rubidium MOT, which is shorter than 1 s. This discrepancy is possibly due to the geometric arrangement of the gauge, the turbo pump and the MOT as shown in figure 3.1. The gauge is very close to the Cesium reservoir, while the MOT is close to the bottom of the glass cell at the bottom of the trap. The glass cell provides a low conductance for the Cesium vapor, such that it takes a much longer time to reach an equilibrium pressure at the position of the MOT. However, the valve to the Cesium reservoir is only open during the actual experiments, such that the time to reach this equilibrium is possibly never reached.

We also observed storage times as long as 15 s in the magnetic trap with the Cesium reservoir open at the same time. This presents further evidence, that the local pressure at the position of the atom traps is smaller than the pressure measured close to the reservoir.

The temperature measured in the Cesium MOT is generally lower than in the Rubidium MOT. This reflects on the one hand that Cesium can be cooled more easily to lower temperatures than other alkali atoms, as already mentioned above. In addition, the Cesium MOT has a lower density. This further facilitates efficient laser cooling.

5.2.2 The Cesium-Rubidium MOT

Our experimental setup allows to operate two MOTs for the two species simultaneously. Careful adjustment of the power balance and alignment of each MOT beam is necessary in order to obtain a good spatial overlap of the two atomic clouds. Since all optics is shared for the beams, it is not possible to change the power distribution among the six beam paths separately for each cooling laser[2]. As a consequence, the alignment of the beams has to optimize both MOTs simultaneously. The atom numbers we could store in each MOT was significantly lower than for optimized single species operation.

The spatial overlap can be controlled with the help of CCD cameras observing the clouds from two directions. For a good overlap, loading curves as displayed in figure 5.4 can be recorded. The fluorescence of Cesium and Rubidium can be distinguished with interference filters and detected separately.

In figure 5.4, first the Cesium MOT is loaded by blocking the Rubidium repumping laser. At $t = 60$ s, the Rubidium is also loaded into the trap. At the same time, the number of trapped Cesium atoms decreases strongly. This strong effect on the Cesium atoms can be explained by collisions between the atoms, which lead to the reduction of the Cesium atoms. We did not observe a significant effect on the Rubidium atoms, when the Rubidium atoms were loaded first into the trap and afterwards the Cesium atoms. We attribute these losses to light induced collisions [43].

The loading curve can be described with a generalization of the rate equation for the loading of a one species MOT (cf. equation (3.26))

$$\begin{aligned} \dot{n}_{\mathrm{Rb}}(t) &= R_{\mathrm{Rb}} - \alpha_{\mathrm{Rb}} n_{\mathrm{Rb}}(t) - \beta_{\mathrm{Rb,Rb}} n_{\mathrm{Rb}}(t)^2 - \beta_{\mathrm{Rb,Cs}} n_{\mathrm{Rb}}(t) n_{\mathrm{Cs}}(t) \quad (5.1) \\ \dot{n}_{\mathrm{Cs}}(t) &= R_{\mathrm{Cs}} - \alpha_{\mathrm{Cs}} n_{\mathrm{Cs}}(t) - \beta_{\mathrm{Cs,Cs}} n_{\mathrm{Cs}}(t)^2 - \beta_{\mathrm{Cs,Rb}} n_{\mathrm{Cs}}(t) n_{\mathrm{Rb}}(t). \quad (5.2) \end{aligned}$$

Here R is the loading rate for a species and α the loss rate due to collisions with background gas. The β coefficients model the losses arising from binary collisions.

These equations can not be solved analytically. A numerical solution with $R_{\mathrm{Rb}} = 0$ for $t < 60$ s and with adjusted parameters describes the measured curves well and is plotted in figure 5.4 in red color. Note, that the differential equations describe the density of the clouds whereas the measured data describes the atom number of the atomic species. For a constant cloud size of the trapped atoms, these two quantities are strictly proportional to each other. Small changes of the cloud sizes possibly lead to the small systematic deviation visible in the plot. The numerical analysis reveals that the interspecies loss coefficient $\beta_{\mathrm{Cs,Rb}}$ is at least a factor of three larger than the other collisional loss coefficients $\beta_{\mathrm{Rb,Rb}}$ and $\beta_{\mathrm{Cs,Cs}}$, while $\beta_{\mathrm{Rb,Cs}}$ is vanishingly small.

Note, that the interspecies loss coefficients $\beta_{\mathrm{Cs,Rb}}$ and $\beta_{\mathrm{Rb,Cs}}$ do not have to be identical. The loss coefficient depends on the rate of inelastic collisions, the amount of transferred energy and in particular also on the trap depths of the Cesium and Rubidium MOT respectively. All these quantities depend in a nontrivial way on the parameters of the MOT [43]. Exactly this dependance renders a quantitative analysis of loss curves as in figure 5.4 very difficult. Complicated and usually over-simplifying models are necessary in order to estimate the trap depth (i. e. the minimum escape velocity) of the trap.

In the preceding experiments by the groups of E. Arimondo and V. Bagnato [110] and the group of N. Bigelow [111], the observed losses were also asymmetrical with respect to the atomic species. However, in all these experiments, the Cesium atoms had a stronger effect on the number of trapped Rubidium atoms than vice versa, as observed by us. Further, most effects observed by these groups were significantly smaller (i. e. less atoms pushed out by the other species) than the effect we observe. These differences can most probably be attributed to different working conditions of the atom traps.

---

[2] This issue has been addressed meanwhile by ordering custom made polarization optics, that changes only the polarization of light with one wavelength, while leaving the other laser beam unchanged. However, this optics will be delivered only after this thesis is already completed.

This underlines once more the principal weakness of this type of experiments. Already comparing different experiments aimed to study cold collisions of the same species in a single species MOT has proven to be difficult. This difficulty is greatly increased, if two species are trapped simultaneously in a MOT. For this reason, I omit a detailed numerical comparison between our loss coefficients and the ones from the literature.

5.3 Results for combined trapping in Magnetic Traps

The analysis of the interaction between the two species is facilitated in the magnetic trap because the effect of the conservative trapping potential can be modelled well. In contrast to a gas trapped in a MOT, trap losses do not play a significant role here. There are no binary collisions between the trapped particles, that release enough energy for escaping out of the trap[3]. As mentioned above, thermalization measurements offer a way to study the collisional dynamics within the mixture.

The same considerations as for loading the Rubidium atoms in the magnetic trap applies here. Also the same stages — compression of the cloud, molasses cooling and optical pumping — are applied.

We found that the same values for the magnetic field worked well for both elements. The detuning and timing of the light fields can be adjusted separately for each element because of the frequency selectivity of the atoms. For the optical molasses we found that a red detuning of 90 MHz yielded good results. Temperatures as low as 10 μK could be obtained after the molasses cooling. The lower temperature as compared to the temperature of the Rubidium atoms (50 μK, cf. table 3.1) is possibly due to the lower density of the Cesium cloud and the overall more advantageous properties of Cesium concerning laser cooling.

Optical pumping of the Cesium atoms is realized by superimposing two additional laser beams onto the beams for the optical pumping of Rubidium. In analogy to the optical pumping scheme used for Rubidium, the optical pumping lasers for Cesium are resonant to the $6S_{1/2}F = 4 \to 6S_{1/2}F' = 4$ and $6S_{1/2}F = 3 \to 6S_{1/2}F' = 4$ transitions and circularly polarized. We achieve a transfer efficiency of up to 70% into the magnetic trap, which is comparable to the transfer of Rubidium atoms into the magnetic trap.

The selective preparation of the atoms by the laser beams during the molasses cooling stage can be used to prepare a basic thermalization measurement by setting the different species on purpose to different temperatures. A first experiment along these lines is shown in figure 5.5. Plotted is the temperature of the Cesium temperature with and without

---

[3] This argument neglects collisions that change the m_F state. For spin polarized Alkali gases, these processes are suppressed and the corresponding loss rates are for the densities of concern here negligible.

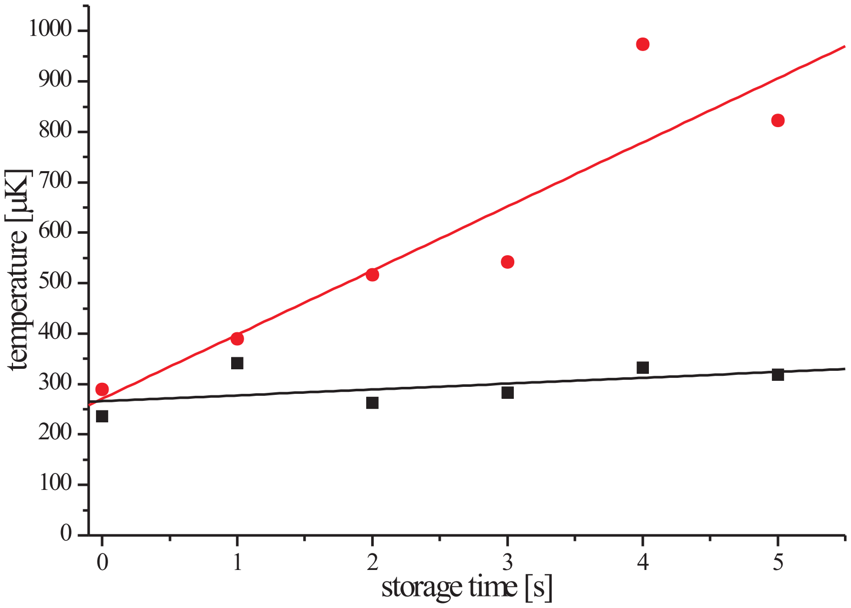

Figure 5.5: Thermalization measurement in the magnetic quadrupole trap. The black data points show the temperature of Cesium stored in the magnetic trap without Rubidium present, the red data points with Rubidium present. For details see the text.

additional Rubidium in the trap. Here, $4 \cdot 10^7$ Rubidium and $1 \cdot 10^7$ Cesium atoms were transferred simultaneously into the magnetic quadrupole trap.

The heating of Rubidium in the presence of Cesium in the magnetic trap is clearly visible, while the Cesium — if stored without additional Rubidium — does not change its temperature significantly with increasing storage. Linear fits of the data yield heating rates R of

$$R_{\mathrm{withRb}} = (127 \pm 28)\ \mu\mathrm{K\ ms}^{-1} \qquad (5.3)$$

$$R_{\mathrm{withoutRb}} = (11 \pm 9)\ \mu\mathrm{K\ ms}^{-1}. \qquad (5.4)$$

We attribute this heating process to a thermalization in the magnetic trap. For a quantitative analysis more systematic measurements of this type — including the determination of the Rubidium temperature — are necessary. However, this initial observation shows the feasibility of the approach.

5.4 Conclusions

In this chapter, I have described the first experiments conducted in our group to study a cold Rubidium-Cesium mixture. So far, a strong interaction between the ultracold clouds trapped in a MOT is observable. The data gained from experiments in conservative magnetic potential can not be used yet to extract quantitative collisional characteristics.

However, the performed experiments show the necessary atom number and temperature of each species, which are required in order to obtain results from such measurements.

The limiting factors are of technical nature so far. All performed experiments rely on the preparation of the atoms before they are transferred into the magnetic trap. The performed experiments clearly demonstrate the potential of the setup to study the interaction between two different atomic species in the ultracold regime.

A more powerful variant of the demonstrated method consists in selectively cooling one species while *already stored* in the magnetic trap. The expected thermalization in this case should lead to sympathetic cooling of the other species. This requires selective manipulation of one species without using near resonant light. In principle, this can be done with the RF setup installed at the experiment, since the Zeeman splitting between adjacent m_F states is 700 kHz G^{-1} for ^{87}Rb atoms and 470 kHz G^{-1} for ^{133}Cs atoms. Therefore for a mixture in thermal equilibrium, the Rubidium atoms would be excited resonantly by the radio frequency before the Cesium atoms in the case of an evaporative cooling RF ramp. For an appropriate timing of the frequency ramp, more high energetic Rubidium atoms would be expelled than high energetic Cesium atoms. Thus an evaporative cooling ramp would cool Rubidium atoms faster than Cesium atoms.

However, this approach is not completely selective, but expels atoms of both species from the trap. A more elegant solution is to employ the microwave transition between the two hyperfine F states for evaporative cooling. The corresponding frequency is 6.8 GHz for Rubidium and 9.2 GHz for Cesium, while the shifts in the transition frequency due to the Zeeman effect is less than 100 MHz. A microwave source can thus address selectively one species, without influencing directly the other one. This enables the preparation of nearly arbitrary temperature differences.

Such a microwave source is set up currently at our experiment. I expect the resulting data to be much easier to analyze.

Chapter 6

Conclusion and outlook

The BEC experiment in Bonn aims to explore ultracold mixtures of Rubidium and Cesium atoms. In this thesis I have presented results of the first steps towards this objective. We have created Rubidium BECs with 10^5 atoms reproducibly and with high reliability. The relevant stages of the experiment are well understood and documented in this thesis.

Further, we have realized cold trapped mixtures of Rubidium and Cesium in a MOT as well as in a magnetic potential. First evidence for the interaction of these two species was obtained. The described measurements pave the way for a systematic investigation of the interaction strength, which can be parameterized by the s-wave scattering length. Possible experimental realizations of these measurements were detailed in chapter 5.

Within the theoretical considerations in chapter 2, special attention was paid to the behavior of double species condensates with large and small atom numbers. The applied models allow predictions concerning the expected properties of these systems and point out the experimental prerequisites which will be necessary for recording signatures of these phenomena.

Efforts at the experiment will concentrate on two areas. First, sympathetic cooling of Cesium has to be implemented. For this purpose, the interaction between the two species has to be understood well enough to be able to exploit it for cooling Cesium in a controlled way. Second, few or even single Cesium atoms must be trapped in a MOT and transferred deterministically into the conservative magnetic potential of the quadrupole and QUIC traps.

6.1 Sympathetic cooling of Cesium

The Rb-K experiment in M. Inguscio's group can serve as a guide for the implementation of sympathetic cooling [47, 117]. In this experiment, selective evaporative cooling was implemented using a microwave technique. The underlying idea is to induce transitions between the hyperfine F states of only one element to transfer it from a trapped state into an untrapped state (cf. section5.4). A microwave system which meets the requirements imposed by this method is already installed in the experiment. First experiments succeeded in cooling trapped cold Rubidium vapor evaporatively.

This technique is expected to have the same success in the Rb-Cs system as in the Rb-K system. However, an open question remains, whether it will be possible to realize a double condensate with this technique as it was possible for the Rb-K system. Pursuing this objective in a magnetic trap poses additional challenges due to the peculiar collisional properties of Cesium [54].

There are two possible approaches to overcome this issue. First it might be possible to use interspecies Feshbach resonances to tailor the Rb-Cs interaction towards an appropriate strength. So far, there has been no search for Feshbach resonances in the Rb-Cs system. However, the likelihood of finding such a resonance is high, as recent results on similar heteronuclear Alkali systems show [28, 29, 115]. Since the magnetic field in these experiments is used as a free parameter, it is advantageous to store the atoms in a non-magnetic potential. We plan to use an optical dipole trap for this purpose. A new coil system, which is currently being built, guarantees the necessary optical access for this trap. Assuming that Feshbach resonances can be found in the system, the success of this approach will depend mainly on the position and structure of the resonance. For controlling the interaction in a conveniant way, a broad resonance at low magnetic fields is preferable.

Another way to reach ultracold temperatures via sympathetic cooling despite the large Cesium–Cesium interaction is to use only low densities of the stored Cesium. This is the approach taken in current experiments aiming to realize a BEC of Cesium in magnetic traps [108]. Calculations performed by A. Montina et al. indicate, that — depending on the interspecies scattering length — this imposes to work with a very small number of Cesium atoms for the trap parameters as available in our setup [123].

6.2 Single Cesium atoms

Storing and manipulating few and even single atoms has been one focus of the research in our group for some time. Cesium atoms have been stored in magneto-optical traps [120] and also in optical dipole traps [124, 125]. Internal degrees of freedom and the position of the atoms can be controlled with high accuracy [126]. The acquired experience of handling single atoms and observing them in a MOT with a high signal to noise ratio can be applied directly to the BEC experiment. Further, most methods applicable for the case of conservative optical traps — including a method to measure the temperature of single trapped particles [127] — can be adapted to particles trapped in magnetic potentials.

Simultaneous trapping of a large number of Rubidium atoms and single Cesium atoms requires a few modifications from the standard procedure used so far in our group. Usually high magnetic field gradients are used to trap single Cesium atoms in a MOT. This opens e. g. the possibility of storing simultaneously a large number of Rubidium atoms in the magnetic quadrupole trap and single Cesium atoms in a MOT at the same location. However, for storing single Cesium atoms together with many Rubidium atoms in a MOT, lower magnetic field gradients are necessary. We have shown in our group, that single particles can be also observed in this case [128].

The observation of many of the described phenomena would benefit greatly from a possibility to image single Cesium atoms within the Rubidium condensate with a spatial resolution of a few μm. This is possible in the experiments conducted in our group with the help of an intensified CCD camera [75]. However, the exposure times used in these experiments are on the order of at least tens of milliseconds, which is much longer than the life time of condensates subjected to resonant light. On the other hand, this thesis indicates that our absorption measurement technique is in principle capable to observe atom numbers as low as 100 at very low temperatures with exposure times as small as 200 μs. For less than 100 atoms, novel detection techniques have to be developed. Alternatively, other signatures of the involved processes (e. g. velocity distributions in the case of the condensation of a few sympathetically cooled Cesium atoms) have to be recorded.

Combining both a detailed knowledge of the Rubidium-Cesium interaction and also the technologies of trapping few Cesium atoms, it should also be possible to create small samples of RbCs molecules. The realization of a quantum degenerate gas grants complete control on all external and internal degrees of freedom of the gas. This control can be directly transferred to molecules generated out of an ultracold mixture. In the extreme case it should be thus possible, to create deterministically one single RbCs molecule. This would open up the possibility to create systems on demand with the tightest control on its properties — such as number of particles, internal and motional state — as permitted by quantum mechanics.

Appendix A

Technical Details

A.1 Optical setup of the UHV MOT

Figure A.1 provides a schematic overview of the optical layout of the lower Rubidium UHV MOT. The dimensions are about to scale. For orientation purposes an optical table with its 2.5 cm spaced bores is shown below the schematics

Although the optical elements shown are roughly at the same position as they can be found on the optical table, the scheme is not an exact image of the experiment. This is due to some simplifications in order to keep the scheme readable. In the actual experiment, each beam can be aligned by two independent mirrors before it enters the MOT region. In figure A.1, some of these mirrors have been omitted. Among other details, all telescopes, an AOM facilitating tuning the optical pumping beam and several monitoring photo diode are omitted. In the top view, beams drawn in red run 5 cm above the table surface, while beams are about 25 cm above the table surface.

Only the laser beams at 780 nm for the Rubidium MOT are shown. The Cesium cooling laser and repumping laser are superimposed onto the Rubidium beams at the dichroic mirror. Similarly, the beams for optical pumping and for imaging Cesium are superimposed onto the respective Rubidium beams.

A.2 Complete timing sequence of the experiment

In figure A.2 a timing sequence for a complete BEC time of flight measurement is sketched. The experiment is divided into separate processes as denoted. Each row in the scheme denotes the physical influence of one or more devices onto the atoms by filling the appropriate square. The following devices are listed in the scheme:

Laser reservoir MOT Cooling and repumping laser in the upper reservoir MOT.

Cooling laser UHV MOT Presence of the cooling laser in the UHV MOT.

Repumping laser UHV MOT Presence of the cooling laser in the UHV MOT.

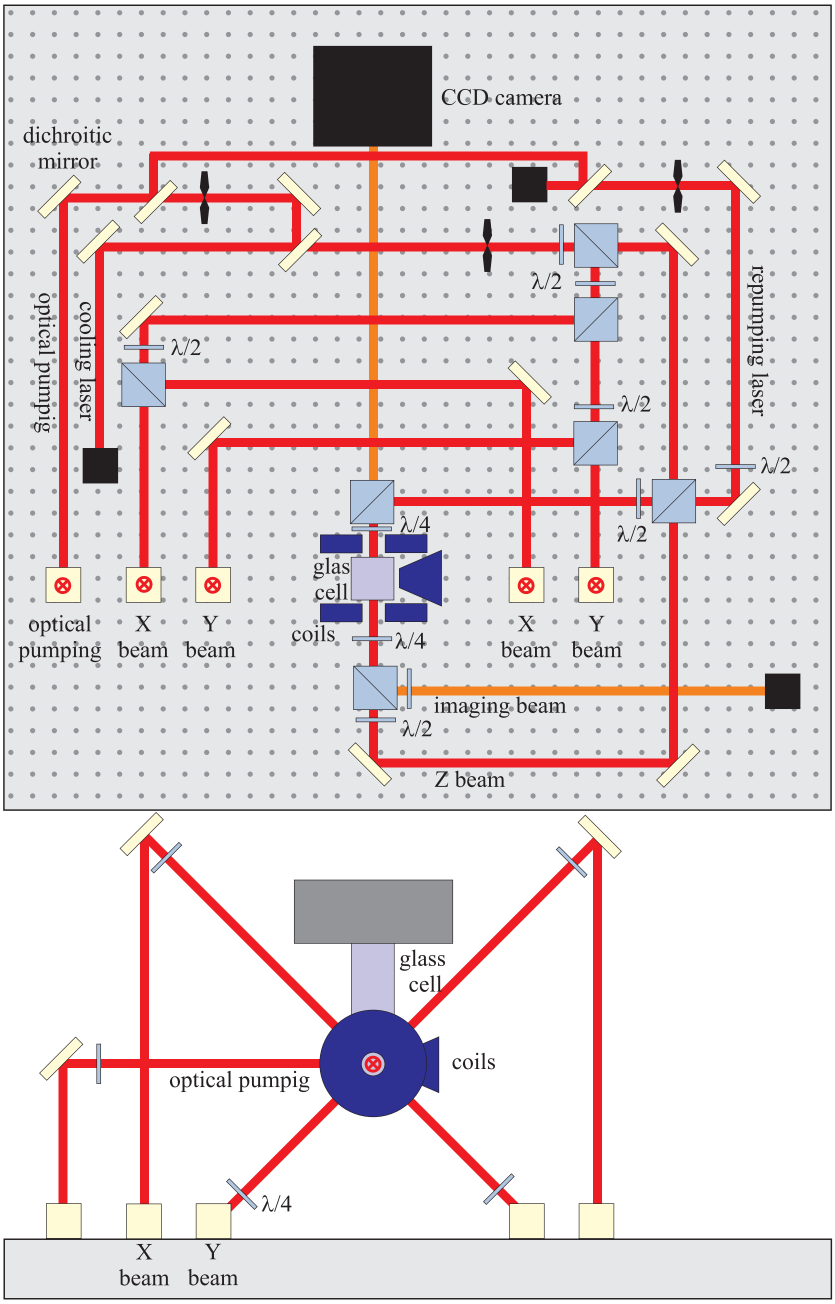
CCD camera
dichroitic mirror
optical pumpig
cooling laser
repumping laser
λ/2
λ/2
λ/2
λ/2
λ/2
λ/4
glas cell
coils
λ/4
optical pumping
X beam
Y beam
X beam
Y beam
imaging beam
λ/2
Z beam
glass cell
coils
optical pumpig
λ/4
X beam
Y beam

Figure A.1: Optical setup of the Rubidium UHV MOT. The above figure shows the schematic optical layout of the UHV Rubidium MOT, the lower figure a view from the side. For details see the text.

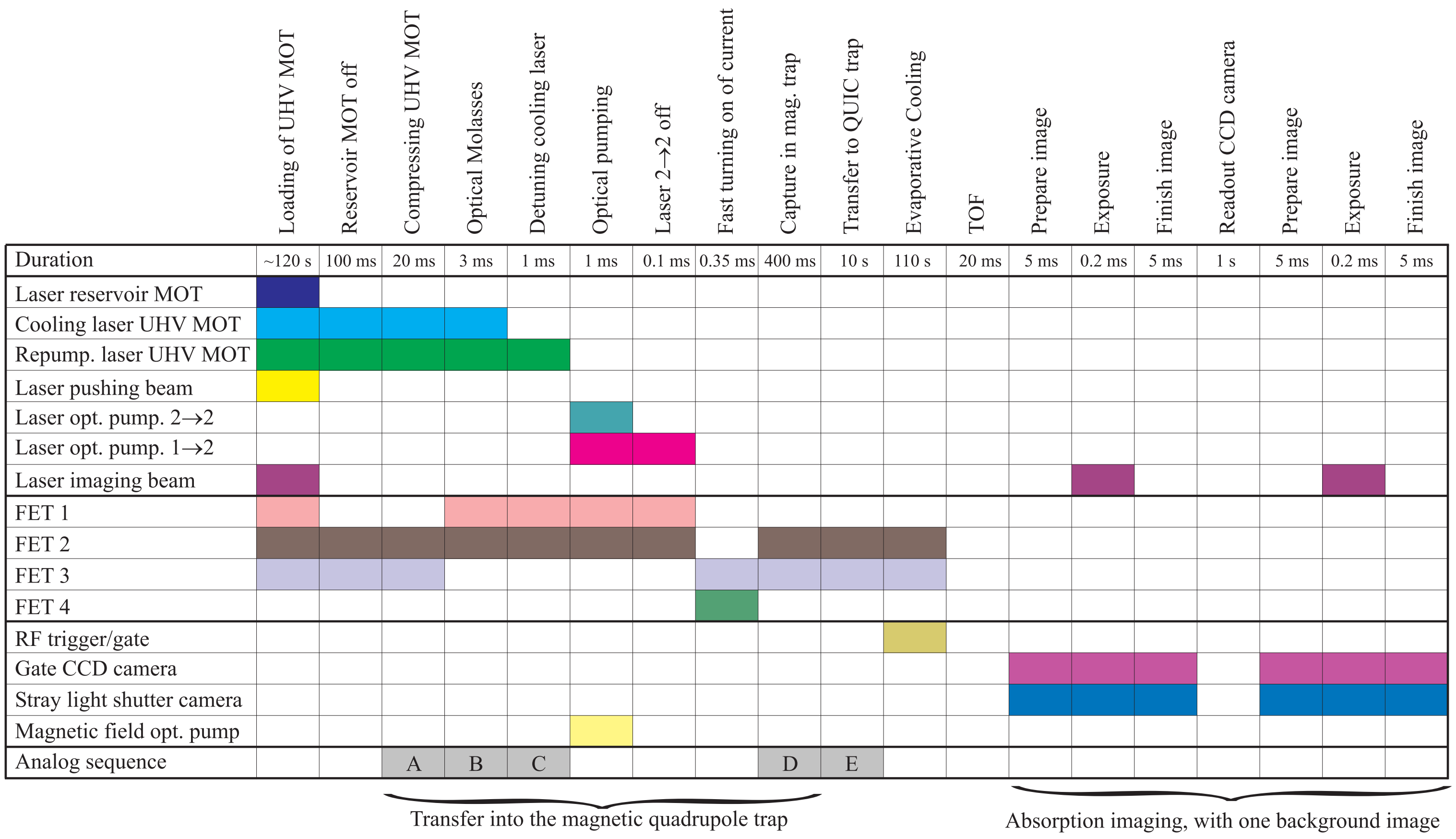

	Loading of UHV MOT	Reservoir MOT off	Compressing UHV MOT	Optical Molasses	Detuning cooling laser	Optical pumping	Laser 2→2 off	Fast turning on of current	Capture in mag. trap	Transfer to QUIC trap	Evaporative Cooling	TOF	Prepare image	Exposure	Finish image	Readout CCD camera	Prepare image	Exposure	Finish image
Duration	~120 s	100 ms	20 ms	3 ms	1 ms	1 ms	0.1 ms	0.35 ms	400 ms	10 s	110 s	20 ms	5 ms	0.2 ms	5 ms	1 s	5 ms	0.2 ms	5 ms
Laser reservoir MOT	■																		
Cooling laser UHV MOT	■	■	■	■															
Repump. laser UHV MOT	■	■	■	■	■														
Laser pushing beam	■																		
Laser opt. pump. 2→2						■													
Laser opt. pump. 1→2						■	■												
Laser imaging beam	■													■				■	
FET 1	■			■	■	■	■												
FET 2	■	■	■	■	■	■	■		■	■	■								
FET 3	■	■	■					■	■	■	■								
FET 4								■											
RF trigger/gate											■								
Gate CCD camera													■	■	■		■	■	■
Stray light shutter camera													■	■	■		■	■	■
Magnetic field opt. pump						■													
Analog sequence			A	B	C				D	E									

Transfer into the magnetic quadrupole trap

Absorption imaging, with one background image

Figure A.2: Timing sequence of a BEC time of flight experiment. The process is divided into time slots of different length as indicated in the most upper row. For details see text.

Laser pushing beam Laser beam for the transfer of the atoms from the reservoir to the UHV MOT.

Laser optical pumping $2 \to 2$ **and** $1 \to 2$ The laser beams for optical pumping.

Laser imaging beam Imaging beam for absorption measurements. Switching the imaging beam is implemented in the experiment with a combination of an AOM and a mechanical shutter.

FET1, FET2, FET2 and FET4 Switches to control the magnetic fields as outlined below.

RF trigger/gate Control of the radio frequency used for the evaporative cooling.

Gate CCD camera Gate signal during which the CCD sensor of our camera integrates.

Stray light shutter camera Opens the shutter in front of the camera in order to record an image.

Magnetic field opt. pumping Gates a coil for the optical pumping magnetic field.

Analog sequence In parallel to the digital channels above, the following analog control signals are used during the sequence:

Sequence A Compressing the UHV MOT. Increasing linearly the gradient of the quadrupole trap from 6 G/cm to 18 G/cm. Simultaneously the detuning of the cooling laser is changed from -15 MHz to -25MHz.

Sequence B Optical molasses. The detuning of the cooling laser is changed from -25 MHz to -90MHz. At the same time, the current of the power supply is increased to prepare for the rapid switching of the magnetic fields.

Sequence C Optical pumping. The cooling laser is set onto the transition $5S_{1/2}F = 2 \to 6P_{3/2}F = 2$.

Sequence D Capturing in the magnetic trap. The power supply for the coil system is regulated with an appropriate waveform in order to pre-compensate transients after the rapid switching of the coils system.

Sequence E Transfer to the QUIC trap. The current through the Ioffe coil is increased for the transport of the atoms into the QUIC trap. For this the two coupled FETs in figure A.3 are used. At the same time, the total current is increased to compress the atoms adiabatically in the magnetic trap.

In the experiment, the timing of the channels is controlled with a `LabWindows` (National Instruments) program described in the PhD thesis [129]. The program accesses a digital I/O card with 32 channels (PCI-DIO-32HS, National Intruments) and an analogue I/O card with 8 channels (PCI-6713, National Instruments). About 30 digital and 4 analog channels are necessary to control the experiment. In addition one GPIB interface card

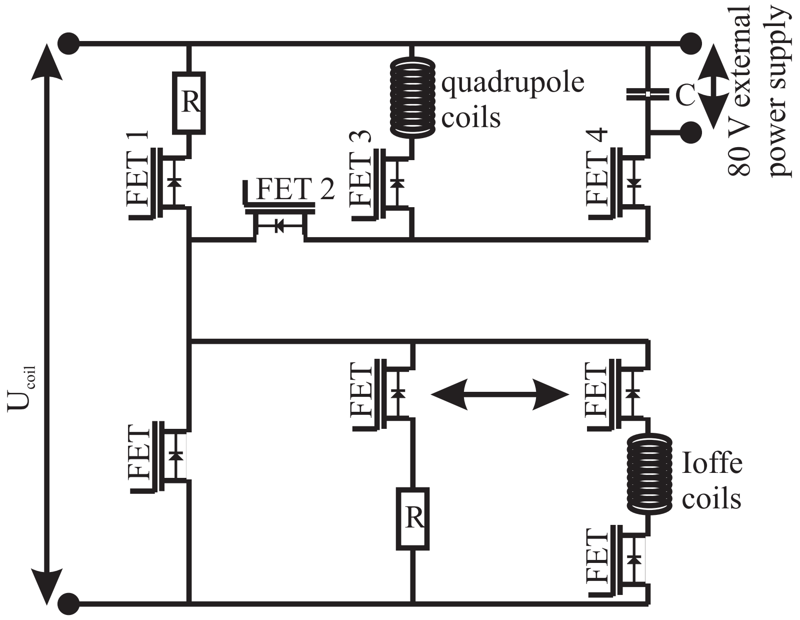

Figure A.3: Circuitry of the coil system. The control of the two FETs connected with the arrow is coupled; all other FETs can be controlled independently. For details see text.

(PCI-GPIB, National Instruments) is used to preprogram the waveform of the radio frequency (cf. section 3.5).

The coil system is controlled by a separate circuitry as shown in figure A.3. FET1 to FET4 are used for the rapid switching of the magnetic fields. Since the current from the power supply can be changed only within fractions of a second, the load of the power supply is changed as little as possible during the switching process. This is achieved by letting the current run through resistances of comparable ohmic restistance as the coils, when the magnetic fields are switched off. For the fast switching of the quadrupole coils, an additional power supply is used to charge a capacitor of about 5mH. The stored charge allows to switch on the fields faster by depleting the capacitor over the quadrupole coils with FET3 and FET4.

Appendix B

Relevant molecular data for the RbCs molecule

Information on the RbCs molecular potential has been gained by molecular spectroscopy, e. g. laser-induced fluorescence, and by theoretical considerations, including ab initio calculations. To the best of my knowledge, table B.1 contains all relevant publications on the ground state potential.

The long range part $U_{\mathrm{lr}}(r)$ of the potential is usually parameterized using a power series

Table B.1: Published molecular data on the RbCs molecule $X^1\Sigma_u$ state. If mentioned in the publication, the dissociation energy D_e and the dispersion coefficients C_6, C_8 and C_{10} are given, as well as the year of the publication

year	D_e [cm^{-1}]	C_6 [10^6 Å^6 cm^{-1}]	C_8 [10^8 Å^8 cm^{-1}]	C_{10} [10^{10} Å^{10} cm^{-1}]	reference
1967		25.9			[130]
1982		28.6	11.4		[131]
1983	3833				[132]
1985		23.4			[133]
1987		35.44	12.0		[134]
1988	3845	54			[135]
1989	4183				[136]
1989	3835				[137, 138]
1992	3838.46	29.361	11.430	4.380	[139]
1996		26.42	9.597	3.639	[140]
1999		25.47	9.8588	4.0932	[141]
1999	3836.14	26.409	11.56	4.3	[142]
2000	3875				[143]

of the form

$$U_{\mathrm{lr}}(r) = C_6/r^6 + C_8/r^8 + C_{10}/r^{10} + \ldots, \tag{B.1}$$

where the coefficients C_i are called *dispersion coefficients*.

For the short range potential, pseudo potentials can be extracted from spectroscopic measurements. Given a sufficient spectroscopic resolution, the analysis of the spectra yields the energies of the vibrational molecular states. In a self-consistent, semiclassical approach, spatial turning points are assigned to these vibrational energies. This yields a list of molecular potential values sampled at these turning points. The pseudo potential for the ground state, which is the interaction potential for ultracold collision between Rubidium and Cesium atoms, is extracted from this list by interpolation.

Table B.1 documents the improved accuracy of the data over the years, as visible by the increasing agreement of the values reported by different groups. However, the known data on the molecule is not sufficient to extract the s-wave scattering length $a_{\mathrm{Rb,Cs}}$ with satisfactory accuracy. M. J. Jamieson et al. calculated explicitly $a_{\mathrm{Rb,Cs}}$ in 2003 [144]. Using four different combinations of values from references [141, 142, 143], they obtained four different values for $a_{\mathrm{Rb,Cs}}$: 595 a_0, 177 a_0, -317 a_0, and -45 a_0.

Appendix C

Numerical methods

Two types of partial differential equations have to be solved to obtain the results presented in chapter 2. This appendix outlines the used techniques.

C.1 Gross-Pitaevski equation

The first equation is the two-species Gross-Pitaevski equation (2.14).

$$\mu_1\psi_1(\vec{r}) = \left(-\frac{\hbar^2\nabla^2}{2m_1} + V_{\text{ext}}(\vec{r}) + \frac{4\pi\hbar^2 a_{11}}{m_1}\left|\psi_1(\vec{r})\right|^2 + \frac{2\pi\hbar^2 a_{12}}{m_{12}}\left|\psi_2(\vec{r})\right|^2\right)\psi_1(\vec{r})$$
$$\mu_2\psi_2(\vec{r}) = \left(-\frac{\hbar^2\nabla^2}{2m_2} + V_{\text{ext}}(\vec{r}) + \frac{4\pi\hbar^2 a_{22}}{m_2}\left|\psi_2(\vec{r})\right|^2 + \frac{2\pi\hbar^2 a_{12}}{m_{12}}\left|\psi_1(\vec{r})\right|^2\right)\psi_2(\vec{r}).$$

Because of the cylindrical symmetry of the trapping potential, each equation appears in cylindrical coordinates as a two-dimensional partial differential equation. The equations are solved by discretizing them on a grid of typically 2500×2500 points. The Thomas-Fermi solution of the problem is used as initial trial function to a Gauss-Seidel type iteration scheme. Although this algorithm is known to converge slowly for large grids [145], the algorithm works well here because of the good quality of the initial trial function. The nonlinearity of the equation was taken into account by keeping the cubed term in the equation fixed during one complete set of Gauss-Seidel iterations. After convergence of the iteration scheme the cubic term was updated with a correction based on the last result. This cycle was repeated until the solution did not change significantly any more. The algorithm was implemented in the C programming language, using a modified variant of the `sor.c` routine found in [145].

C.2 Schrödinger equation

For the determination of the transition temperature of a small atomic sample immersed in a large cloud of the other species (cf. section 2.2.2), the lowest energy eigenvalues of a Schrödinger equation have to be calculated. The potential term of this Schrödinger equation is the the sum of the harmonic trapping potential and the mean field term V_{TF} as defined in equation (2.23) by

$$V_{\text{TF}}(\vec{r}) = \begin{cases} \mu_1 \frac{a_{11}}{a_{12}} \frac{m_1}{2m_{12}} \left(1 - \sum_{i=1}^{3} \frac{r_i^2}{R_i^2}\right) & \text{for } \sum_{i=1}^{3} \frac{r_i^2}{R_i^2} \leq 1 \\ 0 & \text{for } \sum_{i=1}^{3} \frac{r_i^2}{R_i^2} \geq 1. \end{cases}$$

The resulting effective potentials for different values of the interspecies scattering length a_{12} is plotted in figure 2.7. The resulting partial differential equation is not separable because of the boundary of V_{TF}. The symmetry of the trapping potential leads again to a two-dimensional equation.

The used method for the coupled Gross-Pitaevski equations is not possible here because no good trial function is known for the algorithm initially. Instead the eigenvalues of the equation are calculated by rewriting the equation as a time dependant Schrödinger equation with a time dependant scattering length a_{12}. The interaction is slowly increased over time, such the the solution at any time t is changed only adiabatically according to the changed potential. Starting with the known solution for a harmonic trap with $a(0) = 0$, the solution evolves towards the desired solutions for finite values of a (*relaxation method*).

This type of algorithm has the known problem, that only very small time steps Δt can be used to advance the solution in order to avoid divergence from the sought solution. Indeed, the time steps Δt have to be chosen smaller for a finer spatial discretization [145]. In order to stabilize the algorithm, intermediate solutions are processed here by Gauss-Seidel type iterations as described above. The resulting algorithm reproduces the known solutions of test problems without significant deviations.

The relaxation steps are implemented within the `overture` framework for solving partial differential equations. `Overture` is a library for the `C++` programming language freely available from `www.llnl.gov/casc/overture`, together with very comprehensive documentation. The Gauss-Seidel steps are implemented as described above.

It turns out, that the 30 lowest eigenvalues suffice for the results presented in section 2.2.2. Higher eigenvalues become increasingly more difficult to determine, because the highly oscillating initial wave functions require an increasingly finer spatial grid, leading to longer run times of the algorithm. For each eigenvalue determined here, the algorithm ran about 14 hours on a Linux PC with 2 GHz clock speed.

List of Figures

2.1 Bose and Boltzmann distributions in a harmonic trap 7
2.2 Interpretation of BEC as overlapping matter waves 7
2.3 Effective potential in Thomas-Fermi approximation 11
2.4 Thomas-Fermi profiles in comparison with ideal gas profiles 11
2.5 Density distributions of ^{133}Cs and ^{87}Rb double condensates with large atom numbers 15
2.6 Population of the ground states of interaction free, small bosonic samples . 17
2.7 Effective potentials for a few Cs atoms in a harmonic trap with Rb atoms . 19
2.8 Population of the ground state of a system of 10 Cesium atoms interacting with a condensate of 10^4 Rubidium atoms 20

3.1 Setup of the experimental vacuum system 26
3.2 Schematic laser setup 27
3.3 Schematic overview of the imaging system 30
3.4 Experimental test of the imaging resolution 31
3.5 Images used for the standard processing 32
3.6 Temperature measurement by Time Of Flight (TOF) 33
3.7 Measurement of the atom number via optical pumping 36
3.8 Comparison of optical pumping and fluorescence method for the atom number determination 38
3.9 Smallest detectable number of atoms by absorption measurement versus temperature 40
3.10 One dimensional optical molasses 42
3.11 Level scheme of ^{87}Rb 43
3.12 Working principle of a MOT 44
3.13 Sisyphus cooling 45
3.14 Installation of the upper vapor pressure MOT 48
3.15 Loading curve of the reservoir MOT 49

3.16 Reservoir MOT with and without pushing beam 50
3.17 Alignment of the pushing beam 51
3.18 Characterization of the atomic transfer beam 51
3.19 Loading and decay curves of the UHV MOT 52
3.20 Minimum magnetic gradient to support against gravity 55
3.21 Transfer from the MOT into the quadrupole trap 58
3.22 Storage time in the quadrupole trap 60
3.23 Heating of atoms in the quadrupole trap 61
3.24 QUIC setup 62
3.25 Magnetic fields for the transfer into the QUIC trap 64
3.26 Transfer of atoms into the QUIC trap 65
3.27 Storage in the QUIC trap 66
3.28 Truncating the magnetic trap with radio frequencies 70
3.29 RF system for the evaporative cooling 71
3.30 Evaporative Cooling 72
3.31 Thermal cloud, partially condensed cloud and pure BEC 73

4.1 Fitted profiles for a partially condensed atomic cloud 80
4.2 Free expansion of a BEC 81
4.3 Thomas-Fermi radii of a freely expanding BEC 83
4.4 Consistency check based on a measurement of $N_0/(N_0 + N_{\mathrm{th}})$ and T/T_c . . 84
4.5 Fraction of condensed atoms versus T/T_c 85
4.6 Stern-Gerlach detection of multi-component BECs 86
4.7 Vertical and horizontal movement of BECs in different m_F states. 87

5.1 Level scheme of ^{133}Cs 90
5.2 Feshbach resonance 91
5.3 Loading curve of the Cesium MOT 94
5.4 Simultaneous trapping of Rubidium and Cesium in a MOT 95
5.5 Thermalization measurement in the magnetic quadrupole trap 98

A.1 Optical setup of the Rubidium UHV MOT 106
A.2 Timing sequence of a BEC time of flight experiment 107
A.3 Circuitry of the coil system 109

List of Tables

2.1 Transition temperatures for different atom numbers 18

3.1 Typical values for the trapped atomic clouds 67

B.1 Published molecular data on the RbCs molecule $X^1\Sigma_u$ state 111

Bibliography

[1] S. N. Bose, *Plancks Gesetz und Lichtquantenhypothese*, Zeitschrift für Physik **26**, 178 (August 1924)

[2] A. Einstein, *Quantentheorie des einatomigen idealen Gases*, Sitzungsberichte der Preussischen Akademie der Wissenschaften **22**, 261 (September 1924)

[3] A. Einstein, *Quantentheorie des einatomigen idealen Gases: Zweite Abhandlung*, Sitzungsberichte der Preussischen Akademie der Wissenschaften **23**, 3 (January 1925)

[4] A. Pais, *"Subtle is the Lord..." :The Life and Science of Albert Einstein*, Oxford University Press (1983)

[5] W. C. Stwalley and L. H. Nosanow, *Possible "New" Quantum Systems*, Physical Review Letters **36**(15), 910 (April 1976)

[6] T. J. Greytak and D. Kleppner, *Lectures on Spin-Polarized Hydrogen*, volume 38 of *Les Houches Summer Schools*, Chapter 11, 1125, North-Holland, Amsterdam (1984)

[7] I. F. Silvera and J. Walraven, *Spin-Polarized Atomic Hydrogen*, Progress in Low Temperature Physics **10**, 139 (1986)

[8] D. G. Fried, T. C. Killian, L. Willmann, D. Landhuis, S. C. Moss, D. Kleppner and T. J. Greytak, *Bose-Einstein Condensation of Atomic Hydrogen*, Physical Review Letters **81**(18), 3811 (November 1998)

[9] S. Chu, *Nobel Lecture: The manipulation of neutral particles*, Review of Modern Physics **70**(3), 685 (1998)

[10] C. Cohen-Tannoudji, *Nobel Lecture: Manipulating atoms with photons*, Review of Modern Physics **70**(3), 707 (1998)

[11] W. D. Phillips, *Nobel Lecture: Laser cooling and trapping of neutral atoms*, Review of Modern Physics **70**(3), 721 (1998)

[12] M. Anderson, J. Ensher, M. Matthews, C. E. Wieman and E. A. Cornell, *Observation of Bose-Einstein Condensation in a Dilute Atomic Vapor*, Science **269**, 198 (July 1995)

[13] C. C. Bradley, C. A. Sackett, J. J. Tollett and R. G. Hulet, *Evidence of Bose-Einstein Condensation in an Atomic Gas with Attractive Interactions*, Physical Review Letters **75**(9), 1687 (August 1995)

[14] K. B. Davis, M. O. Mewes, M. R. Andrews, N. J. van Druten, D. S. Durfee, D. M. Kurn and W. Ketterle, *Bose-Einstein Condensation in a Gas of Sodium Atoms*, Physical Review Letters **75**(22), 3969 (November 1995)

[15] E. A. Cornell and C. E. Wiemann, *Nobel Lecture: Bose-Einstein condensation in a dilute gas, the first 70 years and some recent experiments*, Review of Modern Physics **74**(3), 875 (2002)

[16] W. Ketterle, *Nobel lecture: When atoms behave as waves: Bose-Einstein condensation and the atom laser*, Review of Modern Physics **74**(4), 1131 (2002)

[17] M. R. Andrews, C. G. Townsend, H.-J. Miesner, D. S. Durfee, D. M. Kurn and W. Ketterle, *Observation of Interference Between Two Bose Condensates*, Science **275**, 637 (January 1997)

[18] I. Bloch, T. W. Hänsch and T. Esslinger, *Atom Laser with a cw Output Coupler*, Physical Review Letters **82**(15), 3008 (April 1999)

[19] S. Burger, K. Bongs, S. Dettmer, W. Ertmer, K. Sengstock, A. Sanpera, G. V. Shlyapnikov and M. Lewenstein, *Dark Solitons in Bose-Einstein Condensates*, Physical Review Letters **83**(25), 5198 (December 1999)

[20] M. Greiner, O. Mandel, T. Essliner, T. W. Hänsch and I. Bloch, *Quantum phase transition from a superfluid to Mott insulator in a gas of ultracold atoms*, Nature **415**, 39 (January 2002)

[21] F. S. Cataliotti, S. Burger, C. Fort, P. Maddaloni, F. Minardi, A. Trombettoni, A. Smerzi and M. Inguscio, *Josephson Junction Arrays with Bose-Einstein Condensates*, Science **293**, 843 (August 2001)

[22] O. M. Maragò, S. A. Hopkins, J. Arlt, E. Hodby, G. Hechenblaikner and C. J. Foot, *Observation of the Scissors Mode and Evidence for Superfluidity of a Trapped Bose-Einstein Condensed Gas*, Physical Review Letters **84**(10), 2056 (March 2000)

[23] Y. Torii, Y. Suzuki, M. Kozuma, T. Sugiura, T. Kuga, L. Deng and E. W. Hagley, *Mach-Zehnder Bragg interferometer for a Bose-Einstein condensate*, Physical Review A **61**, 041602 (February 2000)

[24] D. E. Pritchard, A. D. Cronin, S. Gupta and D. A. Kokorowski, *Atom Optics: Old ideas, current technology, and new results*, Annalen der Physik **10**(1-2), 35 (2001)

[25] E. A. Donley, N. R. Claussen, S. T. Thompson and C. E. Wieman, *Atom - molecule coherence in a Bose Einstein condensate*, Nature **417**, 529 (May 2002)

[26] T. V. Stephan Dürr, A. Marte and G. Rempe, *Observation of Molecules Produced from a Bose-Einstein Condensate*, Physical Review Letters **92**(2), 020406 (January 2004)

[27] C. Pethick and H. Smith, *Bose Einstein Condensation in dilute gases*, Cambridge University Press, Cambridge (2002)

[28] S. Inouye, J. Goldwin, M. L. Olsen, C. Ticknor, J. L. Bohn and D. S. Jin, *Observation of Heteronuclear Feshbach Resonances in a Mixture of Bosons and Fermions*, Physical Review Letters **93**(18), 183201 (October 2004)

[29] C. A. Stan, M. Zwierlein, C. H. Schunck, S. F. Raupach and W. Ketterle, *Observation of Feshbach Resonances between Two Different Atomic Species*, Physical Review Letters **93**(14), 143001 (October 2004)

[30] D. DeMille, *Quantum Computation with Trapped Polar Molecules*, Physical Review Letters **88**(6), 067901 (February 2002)

[31] A. Klein and M. Fleischhauer, *Interaction of Impurity Atoms in Bose-Einstein-Condensates*, preprint arXiv:cond-mat/0407809 (2004)

[32] A. J. Daley, P. O. Fedichev and P. Zoller, *Single-atom cooling by superfluid immersion: A nondestructive method for qubits*, Physical Review A **69**, 022306 (February 2004)

[33] F. Dalfovo, S. Giorgino, L. P. Pitaevski and S. Stringari, *Theory of Bose-Einstein condensation in trapped gases*, Reviews of Modern Physics **71**(3), 463 (April 1999)

[34] W. Ketterle, D. S. Durfee and D. M. Stamper-Kurn, *Bose-Einstein condensation in atomic gases*, Chapter Making, probing and understanding Bose-Einstein condensates, 67, Proceedings of the International School of Physics "Enrico Fermi", Course CXL, edited by M. Inguscio, S. Stringari and C. E. Wieman, IOS Press, Amsterdam (1999)

[35] V. Bagnato, D. E. Pritchard and D. Kleppner, *Bose-Einstein condensation in an external potential*, Physical Review A **35**(10), 4354 (May 1987)

[36] S. Grossmann and M. Holthaus, *On Bose-Einstein condensation in harmonic traps*, Physics Letters A **208**(3), 188–192 (November 1995)

[37] W. Ketterle and N. J. van Druten, *Bose-Einstein condensation of a finite number of particles in one or three dimensions*, Physical Review A **54**(1), 656 (July 1996)

[38] S. Giorgini, L. Pitaevski and S. Stringari, *Condensate fraction and critical temperature of a trapped interacting Bose gas*, Physical Review A **54**(6), R4633 (December 1996)

[39] S. Giorgini, L. Pitaevski and S. Stringari, *Thermodynamics of a Trapped Bose-Condensed Gas*, Journal of Low Temperature Physics **109**(3), 309 (1997)

[40] J. R. Ensher, D. S. Jin, M. R. Matthews, C. E. Wieman and E. A. Cornell, *Bose-Einstein condensation in a dilute gas: Measurement of energy and ground-state occupation*, Physical Review Letters **77**(25), 4984 (December 1996)

[41] F. Gerbier, J. H. Thywissen, S. Richard, M. Hugbart, P. Bouyer and A. Aspect, *Critical Temperature of a Trapped, Weakly Interacting Bose Gas*, Physical Review Letters **92**(3), 030405 (January 2004)

[42] A. L. Fetter and J. D. Walecka, *Quantum Theory of Many-Particle Systems*, Dover Publications, Mineola (2003)

[43] J. Weiner, V. S. Bagnato, S. Zilio and P. S. Julienne, *Experiments and theory in cold and ultracold collisions*, Reviews of Modern Physics **71**(1), 1 (January 1999)

[44] N. N. Bogoliubov, *On the theory of superfluidity*, Journal of Physics **11**, 23 (1947)

[45] P. A. Ruprecht, M. J. Holland, K. Burnett and M. Edwards, *Time-dependent solution of the nonlinear Schrödinger equation for Bose-condensed trapped neutral atoms*, Physical Review A **51**(6), 4704 (June 1995)

[46] J. L. Roberts, N. R. Claussen, S. L. Cornish, E. A. Donley, E. A. Cornell and C. E. Wieman, *Controlled Collapse of a Bose-Einstein Condensate*, Physical Review Letters **86**(19), 4211 (May 2001)

[47] G. Modugno, G. Ferrari, G. Roati, R. J. Brecha, A. Simoni and M. Inguscio, *Bose-Einstein Condensation of Potassium Atoms by Sympathetic Cooling*, Science **294**(5545), 1320 (October 2001)

[48] T.-L. Ho and V. B. Shenoy, *Binary Mixtures of Bose Condensates of Alkali Atoms*, Physical Review Letters **77**(16), 3276 (October 1996)

[49] P. Ao and S. T. Chui, *Binary Bose-Einstein condensate mixtures in weakly and strongly segregated phases*, Physical Review A **58**(6), 4836 (December 1998)

[50] M. Ringler, *Aufbau und Charakterisierung einer Magnetfalle zum Speichern und Kühlen verdünnter atomarer Gase*, Diploma thesis, Universität Bonn (2003)

[51] D. A. Steck, *Rubidium 87 D Line Data*, http://george.ph.utexas.edu/ dsteck/alkalidata/rubidium87numbers.pdf, LANL Release number LA-UR-03-8638 (October 2003)

[52] D. A. Steck, *Cesium D Line Data*, http://george.ph.utexas.edu/ dsteck/alkalidata/ cesiumnumbers.pdf, LANL Release number LA-UR-03-7943 (October 2003)

[53] H. M. J. M. Boesten, C. C. Tsai, J. R. Gardiner, D. J. Heinzen and B. J. Verhaar, *Observation of a shape resonance in the collision of two cold ^{87}Rb atoms*, Physical Review A **55**(1), 636 (January 1997)

[54] P. J. Leo, C. J. Williams and P. S. Julienne, *Collision Properties of Ultracold ^{133}Cs Atoms*, Physical Review Letters **85**(13), 2721 (September 2000)

[55] E. Arimondo, private communication (June 2004)

[56] H. Pu and N. P. Bigelow, *Properties of Two-Species Bose Condensates*, Physical Review Letters **80**(6), 1130 (February 1998)

[57] C. W. Gardiner and P. Zoller, *Quantum kinetic theory. V. Quantum kinetic master equation for mutual interaction of condensate and noncondensate*, Physical Review A **61**, 033601–1 (2000)

[58] M. Imamovic-Tomasovic and A. Griffin, *Quasiparticle Kinetic Equation in a Trapped Bose Gas at Low Temperatures*, Journal of Low Temperature Physics **122**(5/6), 617 (2001)

[59] H. F. Hess, *Evaporative cooling of magnetically trapped and compressed spin-polarized hydrogen*, Physical Review B **34**(5), 3476 (September 1986)

[60] M. Weidemüller and C. Zimmermann, *Interactions in Ultracold Gases*, Wiley-VCH, Weinheim (2003)

[61] K. E. Gibble, S. Chang and R. Legere, *Direct Observation of s-Wave Atomic Collisions*, Physical Review Letters **75**(14), 2666 (October 1995)

[62] C. J. Myatt, N. R. Newbury, R. W. Ghrist, S. Loutzenhiser and C. E. Wieman, *Multiply loaded magneto-optical trap*, Optics Letters **21**(4), 290 (February 1996)

[63] B. Klöter, *Erzeugung ultrakalter Rubidiumatome zur Photoassoziation von Rubidium und Csium*, Diploma thesis, Universität Bonn (2003)

[64] L. Ricci, M. Weidemüller, T. Esslinger, A. Hemmerich, C. Zimmermann, V. Vuletic, W. König and T. W. Hänsch, *A compact grating-stabilized diode laser system for atomic physics*, Optics Communications **117**(5-6), 541 (June 1995)

[65] K. L. Corwin, Z.-T. Lu, C. F. Hand, R. J. Epstein, and C. E. Wieman, *Frequency-stabilized diode laser with the Zeeman shift in an atomic vapor*, Applied Optics **37**(15), 3295 (May 1998)

[66] V. V. Yashchuk, D. Budker and J. R. Davis, *Laser frequency stabilization using linear magneto-optics*, Review of Scientific Instruments **71**(2), 341 (February 2000)

[67] S. Marenbach, *Aufbau und Untersuchung eines stabilisierten Lasersystems für die Bose-Einstein-Kondensation*, Diploma thesis, Universität Bonn (2001)

[68] T. W. Hänsch, M. D. Levenson and A. L. Schawlow, *Complete Hyperfine Structure of a Molecular Iodine Line*, Physical Review Letters **26**(16), 946 (April 1971)

[69] W. Demtröder, *Laser Spectroscopy*, Springer Verlag, 2nd edition (1995)

[70] R. Loudon, *The Quantum Theory of Light*, Oxford University Press, 3rd edition (2000)

[71] A. R. Edmonds, *Angular Momentum in Quantum Mechanics*, Princeton University Press, 3rd edition (1996)

[72] J. W. Goodman, *Introduction to Fourier Optics*, McGraw-Hill, 2nd edition (1996)

[73] H. J. Lewandowski, D. M. Harber, D. L. Whitaker and E. A. Cornell, *Simplified System for Creating a Bose-Einstein Condensate*, Journal of Low Temperature Physics **132**, 309 (2003)

[74] W. Alt, *An objective lens for efficient fluorescence detection of single atoms*, Optik **113**(3), 142 (2002)

[75] Y. Miroshnychenko, D. Schrader, S. Kuhr, W. Alt, I. Dotsenko, M. Khudaverdyan, A. Rauschenbeutel and D. Meschede, *Continued imaging of the transport of a single neutral atom*, Optics Express **11**(25), 3498 (December 2003)

[76] Y.-C. Chen, Y.-A. Liao, L. Hsu and I. A. Yu, *Simple technique for directly and accurately measuring the number of atoms in a magneto-optical trap*, Physical Review A **64**(3), 031401(R) (September 2001)

[77] K. E. Gibble, S. Kasapi and S. Chu, *Improved magneto-optic trapping in a vapor cell*, Optics Letters **17**(7), 526 (April 1992)

[78] N. Davidson, private communication (August 2004)

[79] E. L. Raab, M. Prentiss, A. Cable, S. Chu and D. E. Pritchard, *Trapping of Neutral Sodium Atoms with Radiation Pressure*, Physical Review Letters **59**(23), 2631 (December 1987)

[80] C. Wieman, G. Flowers and S. Gilbert, *Inexpensive laser cooling and trapping experiment for undergraduate laboratories*, American Journal of Physics **63**(4), 317 (April 1995)

[81] H. J. Metcalf and P. van der Straten, *Laser Cooling and Trapping*, Springer Verlag, 1st edition (1999)

[82] P. Lett, R. Watts, C. Westbrook, W. Phillips, P. Gould and H. Metcalf, *Observation of Atoms Laser Cooled below the Doppler Limit*, Physical Review Letters **61**(10), 169 (July 1988)

[83] J. Dalibard and C. Cohen-Tannoudji, *Laser cooling below the Doppler limit by polarization gradients: simple theoretical models*, Journal of the Optical Society of America B **6**(11), 2023 (1989)

[84] P. J. Ungar, D. S. Weiss, E. Riis and S. Chu, *Optical molasses and multilevel atoms: theory*, Journal of the Optical Society of America B **6**(11), 2058 (November 1989)

[85] K. Mølmer, *Friction and diffusion coefficients for cooling atoms in laser fields with multidimensional periodicity*, Physical Review A **44**(9), 5820 (November 1991)

[86] J. Javanainen, *Numerical experiments in semiclassical laser-cooling theory of multistate atoms*, Physical Review A **46**(9), 5819 (November 1992)

[87] S. Chang, T. Y. Kwon, H. S. Lee and V. G. Minogin, *Laser sub-Doppler cooling of atoms in an arbitrarily directed magnetic field*, Physical Review A **66**, 043404 (2002)

[88] T. Walker, D. Sesko and C. Wieman, *Collective Behavior of Optically Trapped Neutral Atoms*, Physical Review Letters **64**(4), 408 (January 1990)

[89] W. Wohlleben, F. Chevy, K. Madison and J. Dalibardb, *An atom faucet*, European Physical Journal D **15**(2), 237 (2001)

[90] L. Cacciapuoti, A. Castrillo, M. de Angelis and G. M. Tino, *A continuous cold atomic beam from a magneto-optical trap*, European Physical Journal D **15**(2), 245 (2001)

[91] R. Ozeri, *Spectroscopy and Time-Dynamics of Bogoliubov Excitations in a Bose-Einstein condensate*, Ph.D. thesis, Weizman Institute of Science, Rehovot, Israel (August 2003)

[92] W. G. und O. Stern, *Der experimentelle Nachweis des magnetischen Moments des Silberatoms*, Zeitschrift für Physik **8**, 110 (February 1922)

[93] J. D. Jackson, *Classical Electrodynamics*, John Wiley and Sons, New York, 2nd edition (1975)

[94] A. L. Migdall, J. V. Prodan, W. D. Phillips, T. H. Bergeman and H. J. Metcalf, *First Observation of Magnetically Trapped Neutral Atoms*, Physical Review Letters **54**(24), 2596 (June 1985)

[95] J. H. Oort, *The structure of the cloud of comets surrounding the solar system, and a hypothesis concerning its origin*, Bulletin of the Atronimical Institutes of The Netherlands **11**(408), 91 (1950)

[96] K. Dieckmann, *Bose-Einstein Condensation with High Atom Number in a Deep Magnetic Trap*, Ph.D. thesis, Universiteit van Amsterdam, (2001)

[97] E. A. Cornell, J. R. Ensher and C. E. Wieman, *Bose-Einstein Condensation in Atomic Gases*, Chapter Experiments in dilute atomic Bose-Einstein condensation, 67, Proceedings of the International School of Physics "Enrico Fermi", Course CXL, edited by M. Inguscio, S. Stringari and C. E. Wieman, IOS Press, Amsterdam (1999)

[98] M.-O. Mewes, M. R. Andrews, N. J. van Druten, D. M. Kurn, D. S. Durfee and W. Ketterle, *Bose-Einstein Condensation in a Tightly Confining dc Magnetic Trap*, Physical Review Letters **77**(3), 416 (July 1996)

[99] E. A. Burt, R. W. Ghrist, C. J. Myatt, M. J. Holland, E. A. Cornell and C. E. Wieman, *Coherence, Correlations, and Collisions: What One Learns about Bose-Einstein Condensates from Their Decay*, Physical Review Letters **79**(3), 337 (July 1997)

[100] D. M. Stamper-Kurn, M. R. Andrews, A. P. Chikkatur, S. Inouye, H.-J. Miesner, J. Stenger and W. Ketterle, *Optical Confinement of a Bose-Einstein Condensate*, Physical Review Letters **80**(10), 2027 (March 1998)

[101] E. Majorana, *Atomi orientati in campo magnetico variabile*, Nuovo Cimento **9**, 43 (1932)

[102] T. Esslinger, I. Bloch and T. W. Hänsch, *Bose-Einstein condensation in a quadrupole-Ioffe-configuration trap*, Physical Review A **58**(4), R2664 (October 1998)

[103] W. Ketterle and N. van Druten, *Evaporative cooling of atoms*, Advances in Atomic, Molecular, and Optical Physics **37**, 181 (1996)

[104] C. R. Monroe, E. A. Cornell, C. A. Sacket, C. J. Myatt and C. E. Wieman, *Measurement of Cs-Cs Elastic Scattering at* $T=30\mu K$, Physical Review Letters **70**(4), 414 (January 1993)

[105] Y. Castin and R. Dum, *Bose-Einstein Condensates in Time Dependent Traps*, Physical Review Letters **77**(27), 5315 (December 1996)

[106] N. Robins and J. Close, private communication (July 2004)

[107] A. J. Kerman, V. Vuletic, C. Chin and S. Chu, *Beyond Optical Molasses: 3D Raman Sideband Cooling of Atomic Cesium to High Phase-Space Density*, Physical Review Letters **84**(3), 439 (January 2000)

[108] Z.-Y. Ma, A. M. Thomas, C. J. Foot and S. L. Cornish, *The evaporative cooling of a gas of caesium atoms in the hydrodynamic regime*, Journal of Physics B **36**(16), 3533 (August 2003)

[109] T. Weber, J. Herbig, M. Mark, H.-C. Nägerl and R. Grimm, *Bose-Einstein Condensation of Cesium*, Science **299**, 232 (January 2003)

[110] G. D. Telles, W. Garcia, L. G. Marcassa, V. S. Bagnato, D. Ciampini, M. Fazzi, J. H. Müller, D. Wilkowski and E. Arimondo, *Trap loss in a two-species Rb-Cs magneto-optical trap*, Physical Review A **63**, 033406 (February 2001)

[111] M. E. Holmes, M. Tscherneck, P. A. Quinto-Su and N. P. Bigelow, *Isotopic difference in the heteronuclear loss rate in a two-species surface trap*, Physical Review A **69**, 063408 (June 2004)

[112] M. Anderlini, E. Courtade, M. Cristiani, D. Cossart, D. Ciampini, C. Sias, O. Morsch and E. Arimondo, *Sympathetic cooling and collisional properties of a Rb-Cs mixture*, preprint arXiv:cond-mat/0410565 (November 2004)

[113] A. J. Kerman, J. M. Sage, S. Sainis, T. Bergeman and D. DeMille, *Production of Ultracold, Polar RbCs** *Molecules via Photoassociation*, Physical Review Letters **92**(3), 033004–1 (January 2004)

[114] A. J. Kerman, J. M. Sage, S. Sainis, T. Bergeman, and D. DeMille, *Production and State-Selective Detection of Ultracold RbCs Molecules*, Physical Review Letters **92**(15), 153001–1 (April 2004)

[115] A. Simoni, F. Ferlaino, G. Roati, G. Modugno and M. Inguscio, *Magnetic Control of the Interaction in Ultracold K-Rb Mixtures*, Physical Review Letters **90**(16), 163202–1 (April 2003)

[116] M. Mudrich, S. Kraft, K. Singer, R. Grimm, A. Mosk and M. Weidemller, *Sympathetic Cooling with Two Atomic Species in an Optical Trap*, Physical Review Letters **88**(25), 253001–1 (June 2002)

[117] G. Ferrari, M. Inguscio, W. Jastrzebski, G. Modugno, G. Roati and A. Simoni, *Collisional Properties of Ultracold K-Rb Mixtures*, Physical Review Letters **89**(5), 053202–1 (July 2002)

[118] C. Wieman and T. W. Hänsch, *Doppler-Free Laser Polarization Spectroscopy*, Physical Review Letters **36**(20), 1170 (May 1976)

[119] C. P. Pearman, C. S. Adams, S. G. Cox and P. F. G. I. G. Hughes, *Polarization spectroscopy of a closed atomic transition: applications to laser frequency locking*, Journal of Physics B **35**, 5141 (2002)

[120] D. Haubrich, H. Schadwinkel, F. Strauch, B. Ueberholz, R. Wynands and D. Meschede, *Observation of individual neutral atoms in magnetic and magneto-optical traps*, Europhysics Letters **34**(9), 663 (June 1996)

[121] B. P. Anderson and M. A. Kasevich, *Loading a vapor-cell magneto-optic trap using light-induced atom desorption*, Physical Review A **63**, 023404 (January 2001)

[122] S. Du, M. B. Squires, Y. Imai, L. Czaia, R. A. Saravanan, V. Bright, J. Reichel, T. W. Hänsch and D. Z. Anderson, *Atom-chip Bose-Einstein condensation in a portable vacuum cell*, Physical Review A **70**, 053606 (November 2004)

[123] A. Montina, R. Mannella and E. Arimondo, *Excitation frequencies and stability regions for two-species Bose-Einstein condensate in a triaxial magnetic trap*, Physics Letters A **261**(5-6), 337 (October 1999)

[124] D. Frese, B. Ueberholz, S. Kuhr, W. Alt, D. Schrader, V. Gomer and D. Meschede, *Single Atoms in an Optical Dipole Trap: Towards a Deterministic Source of Cold Atoms*, Physical Review Letters **85**(18), 3777 (October 2000)

[125] S. Kuhr, W. Alt, D. Schrader, M. Müller, V. Gomer and D. Meschede, *Deterministic Delivery of a Single Atom*, Science **293**, 278 (July 2001)

[126] D. Schrader, I. Dotsenko, M. Khudaverdyan, Y. Miroshnychenko, A. Rauschenbeutel and D. Meschede, *Neutral Atom Quantum Register*, Physical Review Letters **93**(15), 150501 (October 2004)

[127] W. Alt, D. Schrader, S. Kuhr, M. Müller, V. Gomer and D. Meschede, *Single atoms in a standing-wave dipole trap*, Physical Review A **67**, 033403 (March 2003)

[128] H. Schadwinkel, V. Gomer, U. Reiter, B. Ueberholz and D. Meschede, *Quantum Fluctuations of a Single Trapped Atom: Transient Rabi Oscillations and Magnetic Bistability*, IEEE Journal of Quantum Electronics **36**(12), 1358 (December 2000)

[129] S. Kuhr, *A controlled quantum system of individual neutral atoms*, Ph.D. thesis, Rheinische Friedrich-Wilhelms-Universität Bonn (June 2003)

[130] A. Dalgarno and W. D. Davidson, *Long-range interactions of alkali metals*, Molecular Physics **13**, 479 (1967)

[131] A. J. C. Varandas and J. Brandao, *A simple semi-empirical approach to the intermolecular potential of van der Waals systems. I. Isotropic interactions: applications to the lowest triplet state of the alkali atoms*, Molecular Physics **45**(4), 857 (February 1982)

[132] H. Kato and H. Kobayashi, *Laser-induced fluorescence of the RbCs molecule*, Journal of Chemical Physics **79**(1), 123 (1983)

[133] A. Movre and R. Beuc, *Van der Waals interaction in excited alkali dimers*, Physical Review A **31**(5), 2957 (1985)

[134] B. Bussery, Y. Achker and M. Aubert-Frécon, *Long-range molecular state dissociating to the three or four lowest asymptotes for the ten heteronuclear diatomic molecules*, Chemical Physics **116**, 319 (1987)

[135] H. Gustavsson, C. Amiot and J. Vergés, *Spectroscopic investigations of the diatomic molecule RbCs by means of laser-induced fluorescence. I. Rotational analysis of the $^1\Sigma^+$ ground state up to near dissociation*, Chemical Physics Letter **143**, 101 (1988)

[136] D. Pavolini, F. Spiegelmann and T. Gustavsson, *Theoretical study of the excited states of the heavier alkali dimer. I. The RbCs molecule*, Journal of Physics B **22**(11), 1721 (1989)

[137] F. Jenč and B. A. Brandt, *Application of the reduced-potential curve method for the detection of errors or inaccuracies in the analysis of spectra and for the construction of internuclear potentials of diatomic molecules*, Physical Review A **39**(9), 4561 (1989)

[138] F. Jenč, *Limits for the dissociation energy of RbCs by the reduced potential curve (RPC) method*, Journal of Molecular Spectroscopy **143**(2), 396 (1990)

[139] C. E. Fellows, C. Amiot and J. Vergés, *The electronic ground state revisited*, Journal de Physique II **2**, 939 (1992)

[140] S. H. Patil and K. T. Tang, *Multipolar polarizabilities and two- and three-body dispersion coefficients for alkali isoelectronic sequences*, Journal of Chemical Physics **106**(6), 2298 (1997)

[141] M. Marinescu and H. R. Sadeghpour, *Long-range potentials for two species alkali metal atoms*, Physical Review A **59**(1), 390 (1999)

[142] C. E. Fellows, R. F. Gutteres, A. P. C. Campos, J. Vergés and C. Amiot, *RbCs* $X^1\Sigma^+$ *Ground Electronic State: New Spectroscopic Study*, Molecular Physics **197**, 19 (1999)

[143] A. R. Allouche, M. Korek, K. Fakherddin, A. Chaalan, M. Dagher and F. Taher, *Theoretical electronic structure of RbCs revisited*, Journal of Physics B **33**, 2307 (2000)

[144] M. J. Jamieson, H. Sarbazi-Azad, H. Ouerdane, G.-H. Jeung, Y. S. Lee and W. C. Lee, *Elastic scattering of cold caesium and rubidium atoms*, Journal of Physics B **36**(6), 1085 (March 2003)

[145] W. H. Press, B. P. Flannery, S. A. Teukolsky and W. T. Vetterling, *Numerical Recipes in C*, Cambridge University Press, Cambridge, 2nd edition (1993)

Danksagung

Ich möchte mich an dieser Stelle für all die Unterstützung bedanken, die ich im Laufe meiner Promotionszeit erfahren habe. Ich habe mich am Institut sehr wohl gefühlt. Zu meinen schönsten Erinnerungen während der Zeit am IAP gehören die breite Teilnahme an meiner Hochzeit und die Anteilnahme bei der Geburt meiner Tochter.

An erster Stelle soll Herr Meschede genannt sein. Auch während der Zeit, als es im Experiment ziemlich unrund lief, hatte ich immer das Gefühl, sein Vertrauen zu haben.

Herrn Hillert muß ich nicht nur für die freundliche Übernahme des Koreferats danken, sondern vor allem auch für die tatkräftige Hilfe beim Aufbau unseres Vakuumsystems, zusammen mit Herrn Neff.

Bei der täglichen Arbeit habe ich natürlich am meisten von der BEC-Crew profitiert. Mit Michael Haas hatte ich den längsten zeitlichen Überlapp. Was soll ich sagen, jederzeit wieder ! For two years, I could work together with Vanessa Leung, who brought a very valuable view from outside to the experiment. Christian Grachtrup, Diplomand am Experiment während des letzten Jahres, hat mit unglaublicher Ausdauer mitgearbeitet. Mit Bernhard Kloeter und Moritz Ringler hat die Arbeit trotz z.T. widriger Umstände einfach Spass gemacht. Margit Dornseifer war anfangs am Experiment mit dabei. Wir benutzen noch immer einige von ihr eingeführte Aufbauten.

Als Postdoc betreute uns anfangs Victor Gomer, der uns auf seine unnachahmliche Art die Kernpunkte physikalischer Sachverhalte nahebringen konnte. Später hat Arno Rauschenbeutel als Postdoc dann maßgeblichen Anteil am Experiment gehabt. Ohne sein kompromissloses Herangehen an das Experiment hätten wir vielleicht nur die Hälfte hingekriegt. Als ,,Joker" hat uns auch Dietmar Haubrich bei vielen Problemen weitergeholfen.

Den Single Atoms, mit denen wir das Labor teilen, einen herzlichen Dank für die gute Zusammenarbeit auf engem Raum. Besonderen Dank an Wolfgang Alt, von dessem enormen technischen Wissen und physikalischen Verständnis ich enorm profitieren durfte !

Nichts wäre gelaufen ohne die Verwaltung und technischen Werkstätten. Einen herzlichen Dank an Ilona Jaschke, Fien Latumahina und Anneliese Miglo swie Herrn Ernst für die Hilfe bei allen verwaltungstechnischen Dingen. Wesentliche Teile von Experiment wurden uns von der E-Werkstatt und der Feinmechanik zusammengebaut, wofür ich mich stellvertretend bei Herrn Krause, Herrn Rudloff und Herrn Langen bedanken möchte.

Ohne Rückhalt im privaten Bereich hätte ich dieses Projekt nicht durchgestanden. Meine Eltern haben mich während meines gesamten Studiums in jeder erdenklichen Weise unterstützt. Undenkbar, wie das sonst hätte funktionieren können ! Auch meine Schwiegereltern haben mich — besonders seit der Geburt unserer Tochter — tatkräftig unterstützt.

Den größten Anteil hat meine Frau Christine, die immer für mich da war.

Und schließlich noch Dank an meine Tochter Hannah. Sie hat mich zwar im ,,Endspurt" mit ihrer Geburt zunächst ziemlich ausgebremst, aber dann doch so gut mitgespielt, daß ich meine Dissertation zügig zu Ende führen konnte.